Development of a flexible haptic interface using localized friction modulation

Développement d'une interface haptique flexible à modulation de frottement localisé

Thèse de doctorat de l'Université de Lille
préparée au CEA-Leti et au L2EP.

École doctorale n°632 Sciences de l'Ingénierie et des
Systèmes (ENGSYS)
Spécialité de doctorat: Génie Electrique

Thèse présentée et soutenue à Grenoble, le 10 juin 2024, par

Romain LE MAGUERESSE

Composition du jury :

Betty SEMAIL
Professeure, Université de Lille (L2EP)   Présidente

Skandar BASROUR
Professeur, Université Grenoble Alpes (TIMA)   Rapporteur

Emmanuel DEFAY
Ingénieur Chercheur, Luxembourg Institute of Science and
Technology (LIST)   Rapporteur

Matthieu RUPIN
CTO, Vibra Nova   Examinateur

Frédéric GIRAUD
Professeur, Université de Lille (L2EP)   Directeur de thèse

Fabrice CASSET
Ingénieur Chercheur, CEA-Leti   Encadrant

Abstract

Haptic technologies enhance our interactions with human-machine interfaces by integrating the sense of touch. They enable a variety of experiments, particularly on rigid touch screens, ranging from simple vibrations to the reproduction of textures by modulation of the friction between the finger and the vibrating screen in an ultrasonic mode. At the same time, the emergence of flexible electronics, used notably in the manufacture of foldable phones and wearable devices, has led the way to the development of flexible haptic technologies. However, none of these new flexible solutions is effective in reproducing texture effects.

This thesis therefore takes up the challenge of creating a flexible interface capable of reproducing localized or continuous haptic feedback through friction modulation. To achieve this, a hybrid interface concept is developed, integrating rigid haptic resonators of around 1 cm^2 with a polymer film of up to 100 μm thickness. The dimensions of the ultrasonic resonators and the interface, consisting of 3 x 3 resonators, are optimized using analytical models and numerical simulations. Manufacturing is carried out in a cleanroom process, assessed by a life-cycle analysis. Electromechanical measurements validate the technology's performance, with surface displacements of over 1 μm at a low actuating voltage of 20 Vpp. Tribological tests verify the reduction in friction during active user touch. Finally, psychophysical studies confirm the localization and continuity of haptic sensations, thus affirming the multitouch and multi-user nature of this interface. As a result, the potential applications of this new technology are vast, promising improvements in human-machine interactions by reproducing textured sensations on flexible and conformable surfaces.

Résumé

Les technologies haptiques améliorent nos interactions avec les interfaces homme-machine en intégrant le sens du toucher. Elles permettent diverses expériences, notamment sur les écrans tactiles rigides, allant des simples vibrations à la reproduction de textures par modulation du frottement entre le doigt et l'écran vibrant dans un mode ultrasonore. Parallèlement, l'émergence de l'électronique flexible, utilisée notamment dans la fabrication des téléphones pliables et des dispositifs portables, a ouvert la voie au développement de technologies haptiques flexibles. Cependant aucune de ces nouvelles solutions flexibles n'est efficace pour reproduire des effets de texture.

Cette thèse relève donc le défi de créer une interface flexible capable de reproduire un retour haptique localisé ou continu grâce à la modulation du frottement. Pour ce faire, un concept d'interface hybride est développé, intégrant des résonateurs haptiques rigides d'environ 1 cm^2 à un film polymère d'une épaisseur maximale de 100 µm. Les dimensions des résonateurs ultrasonores et de l'interface, constituée de 3 x 3 résonateurs, sont optimisées à l'aide de modèles analytiques et de simulations numériques. La fabrication est réalisée selon un processus en salle blanche évalué par une analyse du cycle de vie. Des mesures électromécaniques valident ensuite le fonctionnement de la technologie avec notamment des déplacements en surface supérieurs à 1 µm pour une faible tension d'actionnement de 20 Vpp. Des essais tribologiques vérifient la réduction du frottement lors d'un toucher actif des utilisateurs. Enfin, des études psychophysiques confirment la localisation et la continuité des ressentis haptiques, affirmant ainsi le caractère multitouch et multi-utilisateurs de cette interface. En conséquence, les applications potentielles de cette nouvelle technologie sont vastes, promettant des améliorations dans les interactions homme-machine en reproduisant des sensations texturées sur des surfaces flexibles et conformables.

Remerciements

Cette thèse est le fruit d'un travail collaboratif de trois années au CEA-Leti à Grenoble et au L2EP à Lille. Je souhaite remercier, en quelques lignes, les personnes qui ont œuvré de près ou de loin à ce travail.

Tout d'abord, je tiens à exprimer ma gratitude aux membres du jury qui ont accepté d'évaluer mes travaux. Merci aux rapporteurs, Skandar Basrour et Emmanuel Defay, pour vos retours sur le manuscrit et vos interactions lors de la soutenance. Merci également à Matthieu Rupin et Betty Semail pour vos échanges durant la soutenance.

Je remercie ensuite mon encadrant Fabrice Casset au CEA-Leti. Merci pour cette opportunité et pour ton accompagnement tout au long de la thèse. Ce fut un grand plaisir de travailler avec toi ! Je garderai de super souvenirs de ces moments de travail ou d'excursions en mission en France et à l'étranger.

Je remercie aussi Frédéric Giraud, mon directeur de thèse, pour ses conseils et son partage d'expertise lors de nos échanges en visio ou lors de mes visites à Lille. Cela a toujours été un plaisir de venir à Lille, à l'IRCICA, pour travailler et échanger autour de la thèse. J'en profite aussi pour remercier toutes les personnes avec qui j'ai pu interagir à l'IRCICA, notamment Anis, Mondher, Detjon, Angelica, Gérémie, Pierre... Merci pour votre accueil et un grand merci à Anis pour son aide sur les manips !

Je voudrais ensuite remercier toutes les personnes qui m'ont aidé au CEA pour mener à bien cette thèse. Je remercie Mikael Colin pour son accueil dans le laboratoire CEA-Leti/DCOS/LICA ainsi que tous les autres membres du labo. Je remercie particulièrement les ingénieures filières, Brigitte Desloges puis Munique Kazar Mendes, pour leurs travaux sur les lots de fabrication, ainsi que toutes les personnes qui ont œuvré à la fabrication de cette nouvelle technologie : Thierry Flahaut, Nadine David, Rémi Franiatte, Daniel Mermin, Jérôme Dechamp... mais aussi Adélaïde Berdague et Séverine Danthon au

Glossary

β Variable coefficient depending on the mode of the free-free square plate

$\Delta\mu$ Friction reduction

$\Delta\Omega$ Frequency range for synchronization

δ_{hom} Deflection amplitude at the center in a case of an homogeneous beam

δ_S Deflection amplitude at the center of the beam

λ Wavelength on the vibrating plate

λ_L Lamé's first parameter

λ_p Wavelength on the polymer film

μ Friction coefficient

μ_0 Friction coefficient without vibration

μ_L Lamé's second parameter

ν Poisson's ratio of the material of the vibrating plate

ν_p Poisson's ratio of the polymer film

ω Pulsation of the vibrating plate

ω_a Pulsation at antiresonance

ω_r Pulsation at resonance

Φ_s Phase of oscillations

ψ Mean phase of the oscillators

ρ Density of the material of the vibrating plate

ρ_p Density of the polymer film

σ_{xz} Transverse mechanical stress

σ_{zz} Normal mechanical stress

A_0 Antisymmetrical plate mode of Lamb : zero-order

C Equivalent capacitance

c_L Longitudinal wave celerity on the vibrating plate

c_T Transverse wave celerity on the vibrating plate

C_0 Electrical capacitance

D_p Flexural rigidity of the polymer film

E Young's modulus of the material of the vibrating plate

E_{hom} Young modulus in a case of an homogeneous beam

E_p Young's modulus of the polymer film

f Frequency of the vibrating plate

f_f Damping of the finger

f_m Frequency of modulation

F_n Normal force

f_s Damping of the surface

F_t Tangential force

h Thickness of the vibrating plate

h_{hom} Thickness in a case of an homogeneous beam

h_p Thickness of the polymer film

Ig_{hom} Quadratic moment of area in a case of an homogeneous beam

K Coupling factor

k Wave number of the vibrating plate

k_f Stiffness of the finger

k_s Stiffness of the surface

k_w Wave number on the polymer film

L Equivalent inductance

L Length of the vibrating plate

l_0 Length of the haptic surface

l_f Chord

L_p Distance between two resonators

m_f Mass of the finger

m_s Mass of the surface

N Number of coupled oscillators

n Number of vibration nodes on the vibrating plate

Q Quality factor

R Equivalent resistance

r Phase coherence

R_c Radius of curvature

R_{mode} Radius of the antinode of vibration

S_0 Symmetrical plate mode of Lamb : zero-order

$u(u_x, u_y, u_z)$ Displacement of the particle at M

V_Φ Phase velocity

Z Impedance

Z_f Impedance of the finger

Z_s Impedance of the surface

d_{31} Piezoelectric coefficient : represents the induced in-plane strain per unit electric field applied perpendicularly to the plane (pm/V)

e_{31} Piezoelectric coefficient : characterizes the coupling between stress and load (C/m^2)

AlN   Aluminium nitride

BVD   Butterworth Van Dyke model

FEM   Finite element method

FPGA   Field-Programmable Gate Array

KAPTON   Polyimide film

KNN   Potassium sodium niobate

LCA   Life Cycle Assessment

PC   Poly Carbonate : thermoplastic polymer containing carbonate groups

PEEK   Polyether ether ketone : organic thermoplastic polymer in the polyaryletherketone (PAEK) family

PET   Polyethylene terephthalate : thermoplastic polymer of the polyester family

PVD   Physical Vapor Deposition

PVDF   Polyvinylidene fluoride

PWM   Pulse-Width Modulation

PZT   Lead zirconate titanate, $Pb[Zr_xTi_{1-x}]O_3$ with $(0 \leq x \leq 1)$

SEM   Scanning Electron Microscope

ZIF   Zero Insertion Force

ZnO   Zinc oxide

Table of contents

List of Figures

xviii

List of Tables

General Introduction

The sense of touch is essential in our daily lives for interacting with the environment and performing essential tasks such as manipulating, holding, or evaluating objects [1]. Individuals who experience partial or complete sensory perception loss face significant challenges in their daily activities. Aristotle recognized the importance of touch in ancient Greece, stating that the sense of touch is the sense whose deprivation leads to the death of living beings.

Despite its crucial role, touch is underutilized in technologies that provide us information and a societal link, which increasingly prevalent and invade our daily lives. Unlike the high-quality visual and audio experiences offered by recent human-machine interfaces, tactile feedback often lacks precision. Various tactile and haptic technologies have emerged in recent years to enhance the overall tactile feedback experience. Haptic surface technologies [2] provide a variety of tactile sensations, ranging from simple vibration alerts, already present in current mobile phones, to more complex sensations such as local pulse and texture stimulation. This is achieved by using inverse filtering [3], time reversal [4], stimulus confinement [5], or even friction modulation techniques [6]. To be efficient, these solutions require specific properties from the surface to be actuated, generally with piezoelectric elements, and their principles have been demonstrated with flat and rigid material, with a simple geometry.

At the same time new flexible and conformable technologies are currently emerging on the market. These include foldable phones, rollable screens and wearable technologies. This is largely due to the development of flexible electronics with polymer film solutions [7]. As a result, over the last few years, researchers have proposed various flexible and conformable haptic devices [8, 9]. However, these solutions essentially provide vibrotactile effects, and none of these interfaces are effective in reproducing

complex haptic effects such as textures.

This work addresses the challenge of creating a flexible haptic interface capable of reproducing localized or continuous feedback through friction modulation. To this end, we draw on the experience of L2EP in Lille, which has been developing rigid haptic interfaces using friction modulation for many years [6], and on that of DCOS/SITEC/LICA at CEA-Leti in Grenoble, which develops and manufactures rigid haptic interfaces [10] and flexible technologies in cleanrooms.

Drawing from a comprehensive review of the current state of the art, the thesis introduces a hybrid interface concept, comprising rigid resonators with ultrasonic lubrication integrated into a flexible polymer matrix, as discussed in Chapter 1. Chapter 2 presents the development of the haptic resonator, the fundamental component of this surface. Subsequently, Chapter 3 outlines the design of a surface featuring nine haptic resonators. Chapter 4 details the realization of this innovative interface using a specific manufacturing process. Finally, Chapter 5 evaluates the haptic capabilities of this pioneering solution which open the way to a new generation of tactile interfaces.

Chapter 1

Haptics and related technologies

Contents

1.1 Introduction

In daily life, the sense of touch allows us to interact with the environment and to perform the necessary tasks by manipulating, holding, or evaluating objects. Individuals who have lost partial or complete sensory perception face significant challenges in their everyday activities. Although essential to our survival, this sense is paradoxically underused in the new technologies that are now omnipresent in our lives today and which will become even more so in the future. Indeed, in contrast to the high-quality visual and audio rendering on recent human-machine interfaces, the tactile feedback lacks accuracy and precision. To address this issue, several tactile and haptic technologies, which derive from the Greek term *haptomai*, meaning "I touch," have emerged in recent years to enhance tactile feedback.

Before implementing haptic technology, it is essential to understand the mechanical and physiological

aspects of the human tactile apparatus, which is based on the presence of mechanoreceptors beneath the skin. This chapter primarily concentrates on these factors in 1.2.1 and 1.2.2. Following this, we present haptic technologies in 1.2.3 that are classified into two main categories : kinesthetic and tactile. Subsequently, we discuss haptic and tactile surfaces, outlining their features in 1.3. We then introduce new emerging technologies based on flexible and conformable haptic technologies in 1.4. The chapter concludes with an overview of the selected concept for a flexible haptic interface and the objectives of the thesis in 1.5.

1.2   Haptics

1.2.1   The sense of touch

The human sense of touch is a highly developed sensory system that allows us to interact with the environment using various methods. According to Klatzy and Lederman [1], exploration movements are classified as a means of interacting with objects and extracting properties about them. This enables us to sense different types of information through touch, such as thermal information which relates to the sensation of heat or cold. For example, a metal plate and a piece of wood at the same temperature can be felt differently. This sensory information affects how we perceive objects. Tactile information, a type of sensory output information, contributes to the perception of an object's texture, geometry, or rigidity by stimulating receptors, such as muscles and tendons. Kinesthetic information is linked to the sensation of movement and can be either active, initiated by the individual, or passive, due to an external force. The term kinesthetic is often used interchangeably with proprioception, which combines information from proprioceptors and mechanoreceptors located in muscles, tendons, joints, and skin. Speaking generally in technical sciences, haptics can be divided into tactile perception, which encompasses all tactile and thermal information, and kinesthetic perception, which includes movement and force information.

Various mechanoreceptors transform mechanical signals on the skin surface into electrical signals to the brain in order to process the informations. The subsequent discussion will focus on the hand and fingers.

1.2.2 The human tactile apparatus

In skin perception, the information from the mechanical deformation of the stimulated part of the skin is encoded by mechanoreceptors [11]. Four types of these receptors are found at different depths in the skin, including the epidermis, dermis, and subcutaneous layer. Thus, the various mechanoreceptors of the human tactile apparatus listed here can be found on Fig. 1.1:

- Pacini corpuscles, FAII (Fast Adapting 2) mechanoreceptors.

- Meissier corpuscles, FAI (Fast Adapting 1) mechanoreceptors.

- Ruffini corpuscles, SAII (Slowly Adapting 2) mechanoreceptors.

- Merkel receptors, SAI (Slowly Adapting 1) mechanoreceptors.
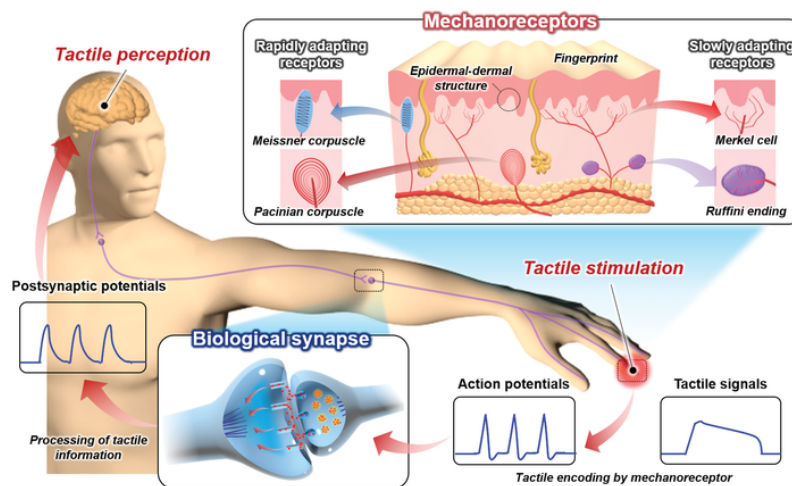
Figure 1.1: Operation of the human tactile apparatus [12].

Mechanoreceptors convert mechanical stimuli at the skin level, including pressure and speed, into nerve impulses that reach the brain. Individually, each receptor has unique features, but in combination they contribute to the perception of touch, and thus to haptic sensations. Table 1.1 summarizes the main properties of mechanoreceptors from [13, 14, 15, 16].

Meissner's corpuscles are located in the area between the dermis and the epidermis. They have a high density of about 140 units per cm^2 and a small receptive field, which allows good spatial localization of the stimulus. Thus, they perform significant roles in detecting indentations and weak vibrations, with

Table 1.1: Main characteristics of the mechanoreceptors.

Characteristics	Meissner Corpuscles	Pacini Corpuscles	Merkel Disks	Ruffini Corpuscles
Adaptation	Fast	Fast	Slow	Slow
Localization	Dermis and epidermis	Dermis and subcutaneous layer	Epidermis	Dermis
Receptive field	3-5 mm	Large area	2-3 mm	Large area
Density	140 units/cm^2	30 units/cm^2	70 units/cm^2	10 units/cm^2
% of sensory units	43 %	13 %	25 %	19 %
Frequency area and threshold	10 -200 Hz / 40 Hz	70 - 1000 Hz / 200 -250 Hz	0.4 - 100 Hz / 50 Hz	0.4 - 100 Hz / 50 Hz
Main functions	Grip, indentation, surface motion, slow vibration	Rapid vibration, mobile stimuli	Discrimination of shape and coarse textures	Skin stretching

a frequency sensitivity ranging from 10 to 200 Hz, and also in determining the grip force when holding an object. Pacini corpuscles are located at a deeper level in the dermis and subcutaneous layer, at a density of 30 units per cm^2. These corpuscles possess a large receptive field, a wide frequency range, and are responsible for the detection of unlocalized vibrations. The detection threshold is approximately 200-250 Hz. Merkel disks are located in the epidermis at a density of 70 units per cm^2, they have a small receptive field of 2-3 mm. They are responsible for detecting coarse texture and shape, static stimulation, and have a response at frequencies below 100 Hz. Rufini's corpuscles are located at a low density of 10 units per cm^2 in the dermis. The corpuscles have a large receptive field, allowing them to detect shearing and sliding of the skin. The distribution of these receptors on the hand is not uniform, and their relative percentages are as follows: 43 % Meismer's corpuscles, 25 % Merkel's disks, 13 % Pacini's corpuscles, and 19 % Ruffini's corpuscles.

The frequency range lies between 0.4 Hz and 1000 Hz, with an optimal frequency of 200-300 Hz for continuous vibration perception at the fingertip level. The minimum sensitivity threshold is 1 µm. The spatial resolution is finer in the fingertips (1-3 mm) than in the palm (10 mm) due to an increased number of Meissner's and Merkel's receptors.

Based on the main characteristics of the human tactile apparatus, researchers have developed haptic technologies to stimulate the sense of touch on different types of interfaces for different applications. The subsequent sections outline these technologies.

1.2.3 Haptic technologies

Haptic interfaces use the sense of touch to enable interaction between a user and a connected system. There is a wide variety of haptic technologies. These can be classified into two main categories which are kinesthetic and tactile force feedback technologies as presented in Fig. 1.2 and adapted from [17].
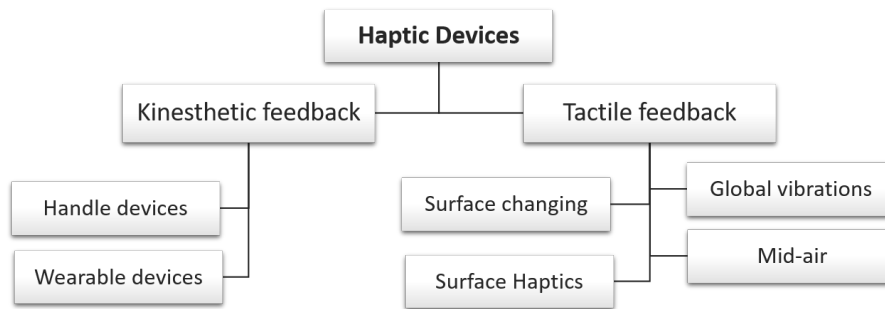
Figure 1.2: Classification of haptic devices.

Kinesthestic technologies

Kinesthetic technologies use force feedback to interact with the user's muscles or tendons, enabling interaction with virtual or real environments. These devices consist of numerous sensors and actuators that provide various degrees of freedom. Haptic technologies can be divided into two main categories as described below.

Handle/grounded devices   The first devices are desktop or fixed devices. They consist of a robotic arm with at least two degrees of freedom, enabling force feedback to simulate collisions with objects in a virtual environment as presented in Fig. 1.3. Thus, the user has the feeling of using a real tool in the virtual environment, thanks to the force feedback. These devices are used, for example, to assist and/or simulate various activities such as surgical [18], maintenance [19] or training tasks [20]. Various products are available on the market such as [21, 22].

Wearable devices   In recent years, kinesthetic technologies have developed with the advent of wearable technologies for video games, virtual reality (VR), augmented reality (AR) and mixed reality (MR) [8, 24]. These devices provide more freedom of movement and facilitate greater interaction com-
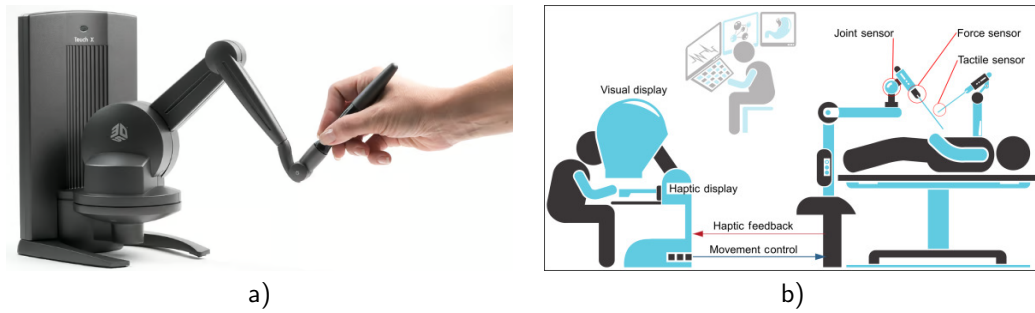
Figure 1.3: a) Phantom device "Touch X" [21]; b) Operation of a robot for surgery with haptic feedback [23].

pared to fixed or handheld devices. Various configurations of wearable devices can be worn directly on the body to support different usage scenarios. Suits [25, 26, 27], gloves [28, 29] and haptic helmets [30] have been developed to enhance virtual immersion (Fig. 1.4). These technologies incorporate a vast array of sensors and actuators to provide diverse haptic feedback to desired body parts and not just the hand or the finger, thus improving the overall experience.

Figure 1.4: a) Haptic glove [29]; b) Haptic suit [25].

Tactile technologies

Haptic technologies with tactile feedback can be divided into several categories. There are haptic surfaces, which we will look at next, but there are also other technologies such as global vibrotactile, surface changing, and mid-air haptics.

<u>**Global vibrotactile**</u> The most widespread haptic technology today is that using large and global vibrations, also known as vibrotaction. In fact, this technology is widely used in smartphones for their vibrating mode, or in gaming joysticks. To obtain haptic feedback, actuators are placed in the desired

equipment to generate large, low-frequency vibrations. The actuators used include eccentric rotating-mass actuators (ERM), linear resonant actuators (LRA), solenoids, voice coils, audio speakers, rotary electromagnetic actuators, and piezoelectric actuators. This solution offers cost-effective and highly efficient haptic feedback. However, the sensing range is limited.

Mid-air haptics   In the latter, the user's hand is not in direct contact with a surface, but is located about ten centimeters away from an array of several ultrasonic transducers. The ultrasonic acoustic field generated by this array of transducers comes from the focalization of the individual acoustic field of each transducer, as shown in Fig. 1.5.a), and allows to obtain localized sensations on the hand and fingers [31, 32, 33]. For example, Ultraleap proposes a commercial device based on this technology [34].

a)   b)
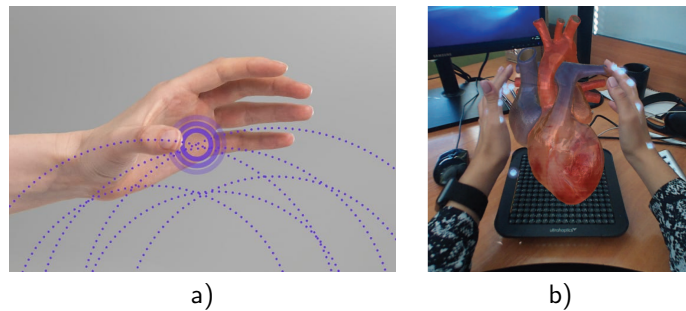
Figure 1.5: a) Focus point for mid-air haptics [34]; b) Example of a use case [35].

Surface changing   Other solutions based on surface deformation exist to propose haptic interaction. The objective is to deform the haptic surface and create a topology with significant displacement. This approach is influenced by Braille, where the characters are raised. Thus various technologies have been developed such as pin array [36], electrode array [37], pneumatic array [38], non-newtonian fludic chamber [39], fluidic chamber [40] and magneto-rheological chamber [41].

However, the spatial resolution is restricted by the number of actuation zones, and it is not easy to integrate into screens or tactile surfaces. For this reason, haptic and tactile surfaces are the preferred haptic technologies and will be discussed in more detail below.
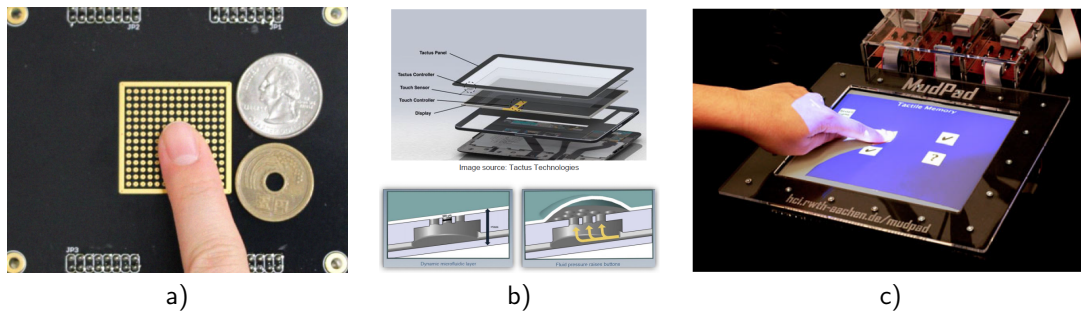
Figure 1.6: a) Electrode array [37]; b) Fluidic chamber [40]; c) Magneto-rheological chamber [41].

1.3   Surface haptic technologies

The focus here is on surface haptic interfaces. In fact, most human-machine interactions take place through a screen or a surface. The development of surface haptics aims to enhance these interactions. Basdogan et al. [2] in a state-of-the-art review propose to classify surface haptics according to the direction of the applied force (Fig. 1.7). This classification is used and adapted in the following.
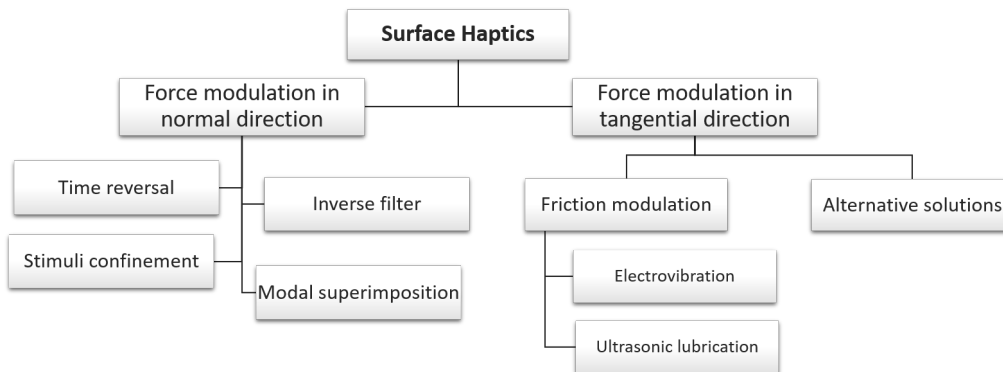
Figure 1.7: Classification of surface haptic technologies.

1.3.1   Normal direction

The first technologies are solutions where the user's finger is placed on the haptic surface and receives a normal force that lifts the finger from the surface. In this case, the finger is static and passive.

Time reversal

In 2009, Kim et al. [42] experimented with a technique based on the constructive propagation and superposition of two mechanical waves in a plate to localize a haptic sensation under the finger. Later, Hudin took up the same idea and developed the time reversal technique [4, 43]. Here too, the aim is to produce localized stimuli with passive touch, using surface waves that interact constructively at spatially and temporally selected points as presented Fig. 1.8.a). To achieve this, it is necessary to use frequency analysis of the signals obtained following excitation of the piezoelectric elements, placed at the periphery of the vibrating surface. By applying a filter using the reversibility of ultrasonic waves, we can reconstruct the ultrasonic field by reversing time. Wockel et al. [44] also propose this technique to create a haptic surface. Their modeling and experimentation with this technique provides an opportunity to create a haptic interface from different piezoelectric actuators.

Inverse filter

Another method to create a haptic effect from normal vibrations is to directly apply a grid of multiple piezoelectric actuators and excite them according to their longitudinal fundamental mode as shown in Fig. 1.8.b). To avoid that the wave propagates over the whole surface and the stimuli overlap, a spatio-temporal inverse filter is used. This "Inverse filter" method [45] thus allows the generation of a single stimulus per piezoelectric actuator placed under the surface. The filter allows each piezoelectric actuator to be stimulated at the desired frequency and prevents signals from being superimposed.
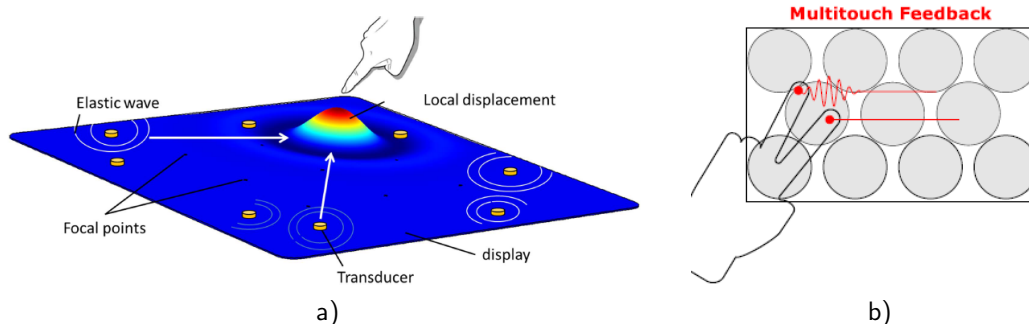
Figure 1.8: a)Time reversal illustration [46] ; b) Inverse filter illustration [3].

Stimuli confinement

Later, Ben Dhiab and Hudin [5] investigated an alternative method for creating a haptic surface with stimulus confinement. The piezoelectric elements generate vibrations that are confined to a specific region of the surface. Unlike previous approaches, electronic filters are not used. Instead, the surface geometry is optimized by subdividing it into haptic bands. Piezoelectric elements are placed on each of these bands, as can be seen in Fig. 1.9. The vibrations generated by these elements are at a frequency lower than the cutoff frequency and therefore do not propagate through the medium. In this way, the bands act as waveguides, confining the waves. Multitouch solutions result from this confinement of haptic feedback. This promising technique for generating localized haptic effects requires that the interface be rigid enough to allow the waves to propagate along the band.

Figure 1.9: Experimental set up for stimuli confinement [47].

Modal superimposition

Another method to generate normal forces under the finger is modal superimposition [48]. Here, piezoelectric elements are glued directly under a beam suspended on two supports. When the piezoelectric elements are excited, the beam vibrates. By combining and synchronizing the modes of vibrations, a vibration pattern, showing a peak of displacement at a specific positions, can be obtained. The modal composition is done by projecting the vibration pattern onto the modal base. As a result, the user can feel a normal force under the finger at the position of the vibration peak as presented in Fig. 1.10.a). When a normal and a lateral mode are superimposed an elliptical movement of the beam can be produced. This has the effect to produce a click [49]. The validity of this method has been demonstrated on an aluminum beam as shown in Fig. 1.10.b).

a)   b)

Figure 1.10: a) Experimental cartography for modal superimposition [50] ; b) Superimposition of two modes to obtain a click [51].

1.3.2   Tangential direction

The focus is now on surface haptic technologies where the main effort is tangential. The most important of these are those based on friction modulation. These techniques enable very interesting texture rendering when the finger is moving across the surface.

Electrostatic force

Electrostatic forces, or electrovibration, was the first solution to dynamically change the friction between a finger and a conductive plate. In this case, the aim is to create a Coulombian force of attraction between the surface and the finger by applying a potential difference between the two parts [52]. There are various ways of achieving this, but the haptic effect is always the same : an increase in friction when the finger slides over the surface. The solution is shown in Fig 1.11.a). Teslatouch [53] has for example developed a screen based on this technology. The haptic surface consists of several layers. A conductive layer is added to the screen, and an insulating layer forms the top surface. So a voltage applied to the conductive layer while the finger is in contact with the insulating surface induces a Coulombic attraction force. The user then feels an increase in friction with this technology. High voltages are required, complicating the control electronics in particular, and the outdoor environment can be problematic; operation becomes complicated in high humidity conditions [54].

Ultrasonic lubrication

The second approach involves ultrasonic lubrication, which uses ultrasonic waves generated by piezo-electric actuators within a rigid substrate. In 1995, Watanabe [56] was the first to use an ultrasonic
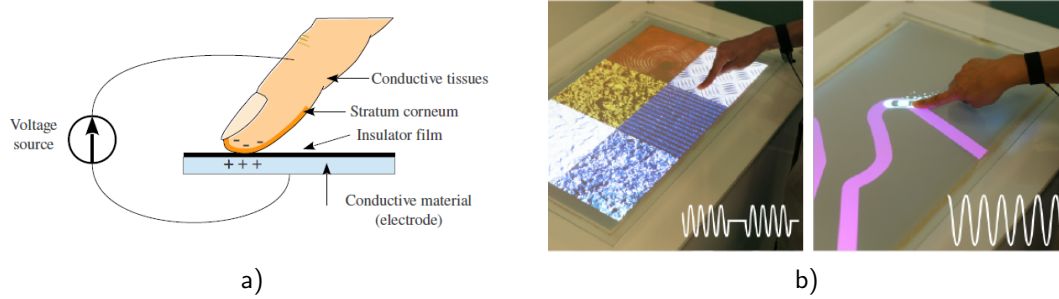
Figure 1.11: a) Operation of electrovibration [55]; b) Tesltatouch [53].

technique to modify the texture of a rough surface. He noted that the use of ultrasound could modify the perception of surface roughness. When the user presses down on the surface with his finger, he/she feels a lubrication of the surface, i.e. a reduction in friction. He notes that this requires a frequency higher than 20 kHz. It enables also to avoid the audible frequency spectrum. In this situation, the surface vibrates according to a flexural mode as an antisymmetric Lamb mode generated by the piezoelectric actuators. This wave is assimilated to a standing wave in the desired bending modes.

There are two mechanisms involved in ultrasonic lubrication. The first mechanism observed and studied is the "squeeze film effect". Watanabe theorized this effect of a layer of air between the finger and the surface as early as 1995. Subsequently, Biet [57, 58] confirmed this theory. A thin layer of air is present between the finger and the vibrating surface due to the ultrasonic vibrations of the surface. Fig. 1.12 shows the profile of the finger and its epidermal ridges [6]. This makes it possible to estimate the effect of the air layer on friction reduction. In fact, the pressure of the air trapped in the thickness noted $h(x)$ can be calculated in order to have the variation of the friction coefficient. Thus, the greater the initial roughness, the greater the amplitude of vibration required to achieve a squeeze film effect.
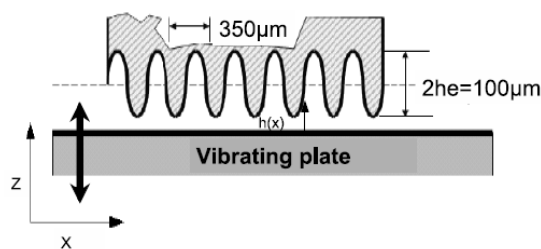
Figure 1.12: Finger on the vibrating surface [6].

Subsequently, Sednaoui [59] notes that the velocity of exploration on the surface is also an essential

parameter. In addition, the resonance frequency of the vibrating plate also plays a role. As the resonance frequency increases, the friction decreases. He also notes that the change in friction tends towards an asymptotic value, i.e. saturation occurs.

A second mechanism is present in ultrasonic lubrication : the fact that the contact between the finger and the vibrating surface is intermittent as the user explores. This intermittent contact naturally reduces friction. This mechanism, combined with the squeeze film effect, has recently been highlighted and demonstrated by Vezzoli and Sednaoui [60, 61] and Wiertlewski [62].

Fig. 1.13 shows two examples of tactile surface using friction reduction produced by the L2EP of the University of Lille and using PZT piezoelectric ceramics to actuate the ultrasonic vibration mode.

a)   b)
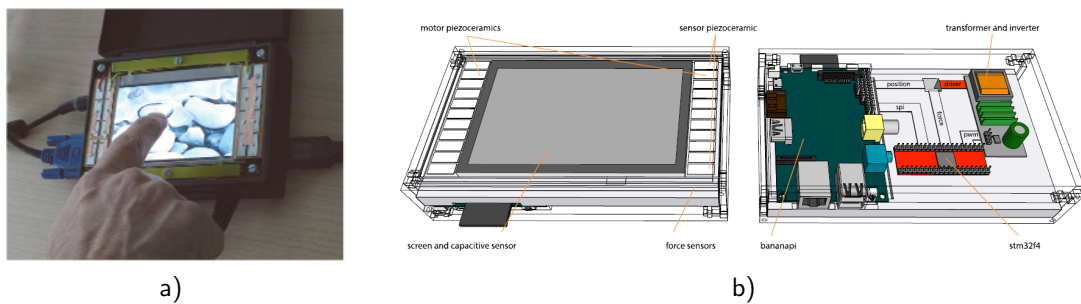
Figure 1.13: a) Tactile stimulator using friction reduction [63]; b) E- Vita solution [64].

Since then, other piezoelectric materials have been used to develop haptic surfaces using friction reduction. Indeed thin-film PZT [65, 66, 67] or AlN [68] have been proposed to obtain this kind of solution. Furthermore, thin-film processes employ microelectronics tools and facilities, offering promising industrial and large volume fabrication perspectives. Using this friction reduction technique HAP2U has presented a number of demonstrators, notably at recent CES events with a mobile phone and automotive solutions [69].

In this friction reduction technique, the waves are not localized; the entire surface is subjected to a vibrational mode. However, Hudin manages to prove that it is possible to localize the effect on a very small surface [70]. By combining two piezoelectric elements excited in a non-propagative way, as explained in the section on stimulus confinement, confined zones of friction reduction can be created.

More recently, Daunizeau et al. [71] propose the use of metamaterials to localize the friction reduction effect, as shown in Fig. 1.14. They do this by localizing the vibrational modes that allow ultrasonic lubrication between waveguides. Torres Guzman et al. [72] suggest using a longitudinal vibration mode

instead of the bending modes commonly used in ultrasonic plates.
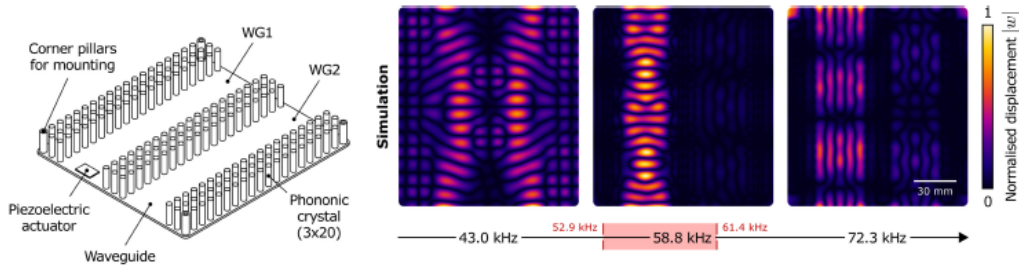
Figure 1.14: Metamaterials for friction reduction [71].

Both of the solutions using friction modulation, electrovibration and ultrasonic lubrication, enable very interesting texture rendering, far superior to simple vibration feedback. As Meyer shows in his study [73], the electrostatic solution has a much better response time than the ultrasonic method. However, texture rendering is more significant with the ultrasonic technique. The L2EP team [55] proposes to couple these two solutions.

Alternative solutions

It is also possible to generate a tangential force directly on the surface, providing indirect haptic feedback to the finger. One solution proposed in [74] is the creation of a laterally vibrating surface, known as the LateralPaD in Fig. 1.15.a). PZT ceramic stacks attached to the lateral edges of the surface generate a lateral force that the finger on the surface experiences as tangential feedback. This system requires a high actuation force, and thus a high power, due to the stiffness of the surface, which results in a significant stack of piezoceramics occupying a considerable amount of space and requiring a high power. Therefore, it is not well suited for localized haptics.
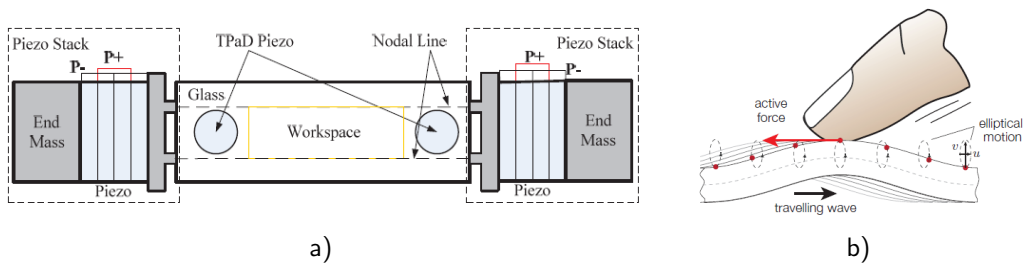
Figure 1.15: a) Lateralpad [74]; b) Operation of Ultraloop solution [75].

A second method [76, 75] involves producing a traveling wave on the beam surface using two

piezoelectric transducers as presented in Fig. 1.15.b). The propagating wave modifies surface friction in a similar way to the ultrasonic friction reduction technique. Notably, the propagation wave offers greater friction contrasts than the Lamb wave. Friction reduction is observed in the same way as with the stationary wave, but the driving force in opposition to the direction of the propagation wave is also experienced. These two forces are superimposed for better haptic rendering.

Other systems are available for producing tactile feedback through asymmetrical friction modification that is similar to the LateralPad. Two examples are ShiverPad [77] and ActivePad [78]. ShiverPad provides low or high friction based on surface vibration. The ultrasonic lubrication effect created by the piezoelectric elements is thus coupled with lateral vibration. The ActivePad solution also makes it possible to control the direction of the lateral vibration.

1.3.3 Surface haptics overview

The table 1.2 summarizes some of the main surface haptic technologies and their characteristics.

Table 1.2: Main surface haptics technology and characteristics.

	Technologies	Main feeling	Amplitude displacement	Frequency	Localization
Vibrotactile - Normal force	Inverse filter	Pulse	>10 μm	< 1 kHz	Yes
	Modal superimposition	Pulse	>1 μm	> 20 kHz	Yes
	Time reversal	Pulse	>10 μm	< 1 kHz	Yes
	Stimuli confinement	Pulse	>10 μm	< 1 kHz	Yes
Friction modulation - Tangential force	Electrostatic	Texture	-	-	No
	Ultrasonic lubrication	Texture	>1 μm	> 20 kHz	No
	Metamaterials	Texture	>1 μm	> 20 kHz	Yes

As observed in this section and summarized in this table, haptic surface solutions using a normal force under the finger enable localized vibrotactile sensations through pulses or stimuli achieved via electronic or geometric filtering techniques. However, they do not allow for more complex renderings such as texture reproduction, apart from the solution proposed by Hudin. On the other hand, localization of feedback is very difficult for solutions based on friction modulation. A geometric method using metamaterials introduced by Daunizeau seems to be an interesting approach, but the localized area remains too large for now.

In the following, the focus is on flexible and conformable haptic solutions.

1.4 Flexible and conformable haptic technologies

1.4.1 Introduction

The aim today is to develop smart surfaces that combine numerous functions with a wide range of materials and shapes. In the automotive industry, for example, the trend is to replace dashboard screens and buttons with smart surfaces that are button-free, conformable to any geometry and totally reconfigurable [79]. In the field of consumer electronics, flexible and conformable technologies have already appeared, such as foldable phones and rollable displays [80]. These technologies are based on the emergence of flexible electronics using printed polymer technologies [7].

Consequently, researchers are motivated to develop conformable haptic technologies [81, 9]. As seen in the previous part, flexible and conformable haptics already represent an important market through wearable solutions used for VR/AR/MR technologies [8, 82]. However, these technologies are very often kinesthetic, with haptic suits, jackets and gloves.

In this section, the focus is on soft technologies designed for tactile interactions where the finger directly touches and interacts with the surface.

1.4.2 One main limitation

One of the first flexible interface solutions we can mention is the Reflex solution proposed in 2016 [83]. The smartphone proposed here is very slightly flexible, with non-localized vibrotactile feedback of the ERM type found in conventional smartphones. This solution uses the smartphone and its semi-rigidity to propagate the wave emitted by the actuator, which means that it is not a truly flexible solution. This solution highlights the main problem with flexible and conformable technologies. These new devices cannot use the same operating principles as rigid technologies. Indeed, as we saw in the previous section, most haptic surfaces use mechanical wave propagation in a medium to emit vibrations and feedback to the user. However, the flexibility of these new conformable technologies causes the waves to be attenuated, resulting in unwanted tactile feedback. As a result, other haptic technologies with a wide range of actuators have been developed. We present them according to the actuators used.

1.4.3 Main solutions

Polymer actuators

The first technologies discussed involve the use of PVDF-type piezopolymer actuators. By integrating these actuators into a flexible matrix, a solution with haptic feedback can be achieved. Ju et al. developed an interface using this type of device [84], resulting in vibrotactile feedback. A beam structure is realized with the ferroelectric polymer film and two electrodes under a capacitive touch sensor (Fig. 1.16.a). When the screen is touched by the user, the beam is activated, resulting in flexural vibration. Thus the touch screen produces more than 1 μm of vibration amplitude for an applied voltage of 100 V at 220 Hz, its resonance frequency. The vibrations are localized on the top of the actuators.
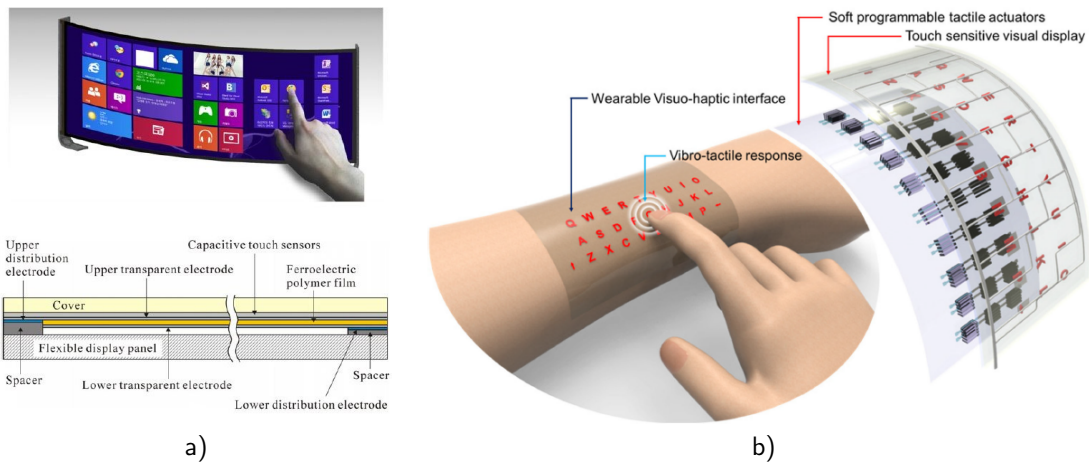
Figure 1.16: a) Haptic interface with PVDF actuators [84]; b) Haptic interface with dielectric microactuators [85].

Yun et al. [85] present a solution that employs polymeric dielectric microactuator (DEMA) technology (Fig. 1.16.b) to guide waves through a transparent polymer. This technology incorporates AgNWs electrodes designed to selectively activate the desired surface areas. When an electric field is applied across the electrodes, the tactile actuator is compressed in the thickness direction and simultaneously deformed in the vertical direction by planar expansion. The user experiences vibrotactile feedback when pressing the screen. The interface measures less than 200 μm in thickness and provides a response time of less than 1 ms. The localized feedback produces a force of 100 mN at a frequency of approximately 240 Hz, but it is for a very high electric field of 15 MV/m. This technology enables localized vibrotactile

feedback.

Park et al. [86] suggest a similar solution involving an electroactive actuator composed of a PVC and silicon dioxide nanoparticle composite. This actuator can be integrated into a flexible matrix to create a larger interface, however it requires again a high actuation voltage of 1 kV.

Magnetic actuators

Magnetic actuators can be integrated into a flexible matrix for haptic rendering using independently controlled actuators [87, 88]. These actuators are embedded in a flexible matrix composed of different silicone layers (Fig. 1.17). This technology is presented as an "e-skin"-type wearable solution. The actuators vibrate from 100 to 300 Hz with a maximum amplitude of 35 µm at a power of 35 mW. The size of the actuators is on the order of 20 mm in diameter, resulting in a low-resolution interface. In addition, the interface is only suitable for vibrotactile applications.
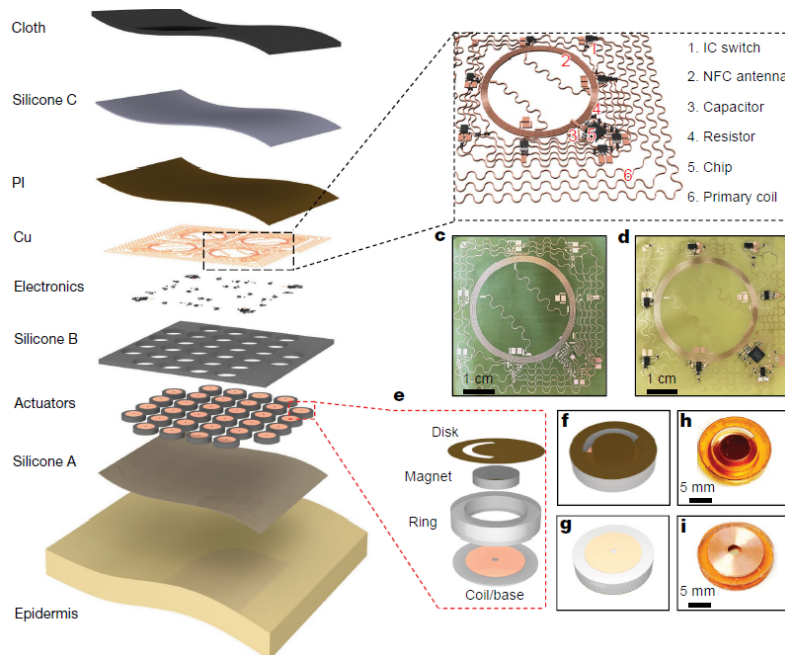
Figure 1.17: Haptic interface with magnetic actuators [87].

Electrostatic actuators

Here we focus on an electrostatic transducer technology that could be used to create a flexible interface. Trase [89, 90] proposes a solution based on two polymer films, separated by an air gap of height h, and a flexible electrode. When a high voltage is applied across the electrode, the length of the electrode in contact with the two polymer films increases, and the transducer compresses. This solution enables large displacements of up to 3 mm here, at a maximum voltage of 300 V. However, the haptic effect generated is not very significant. The user only detects variations in amplitude, for relatively high working voltages.

Hydraulic actuators

The actuator proposed by Ma et al. [91] is a very compact electrohydraulic actuator, requiring no hydraulic circuit. The actuator can be attached to a flexible die, for example. The actuator consists of a liquid and a dielectric film trapped between two flexible electrodes. When the electrodes are energized, a Maxwell force is generated that squeezes the dielectric fluid in the center and deforms the top and bottom PDMS layers. The characteristics of this actuator are as follows: response time 0.15 s; maximum displacement 1.1 mm; maximum force 1 N/cm^2; operating frequency 20 Hz. The problem here is the required voltage (12 kV), which makes this principle unsuitable for consumer applications for the time being. Grasso et al. [92] propose a similar device named HAXEL (Hybraulically Amplified Taxels) as presented on Fig. 1.19.a). This device is bonded directly to the finger, but can also be designed to have a larger surface area for touch interaction.
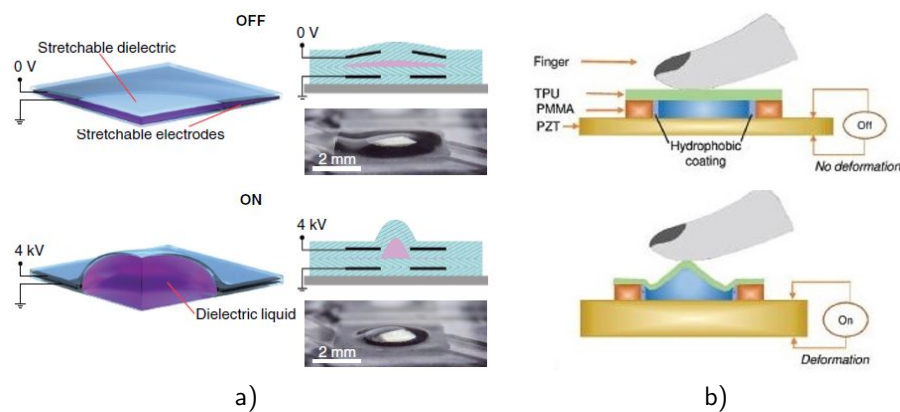
Figure 1.18: a) HAXEL [92]; b) Actuator based on acoustofluidics [93].

Akther et al. [93] develop an alternative based on acoustofluidics (Fig. 1.19.b).   The piezoelectric elements create an acoustic pressure field in a chamber. This pressure field acts on the liquid trapped in the chamber, resulting in the creation of two forces: the acoustic radiation force and the viscosity force. These two forces act together on a deformable upper membrane, resulting in haptic feedback for the user. The deformation obtained at the membrane surface can reach 100 µm in a static case and 0.5 µm for dynamic excitation at 1 kHz. This technology is interesting and could be applied to a flexible interface. Each element is independent, and there is no hydraulic circuit. However, this solution requires an accurate control of acoustofluidics.

Alternative actuators

A flexible haptic solution based on a pneumatic technology has also been developed [94]. This interface includes a membrane made of a polymer shape memory actuator, which is heated and deformed from electrodes by Joule effect. In addition, a pressurized membrane is used to circulate air to shape the interface as desired.   This solution allows for large deformations, with an average displacement of 275 µm per pixel achieved at a force of 225 mN. However, the setup is challenging as it requires the configuration of both pneumatic and electrical circuits. Additionally, researchers have developed thermohaptic solutions [95]. These solutions use the Joule effect to heat the surface and the Peltier effect to cool it down. Users will only feel the thermal effects, not deformation as with previous technologies.
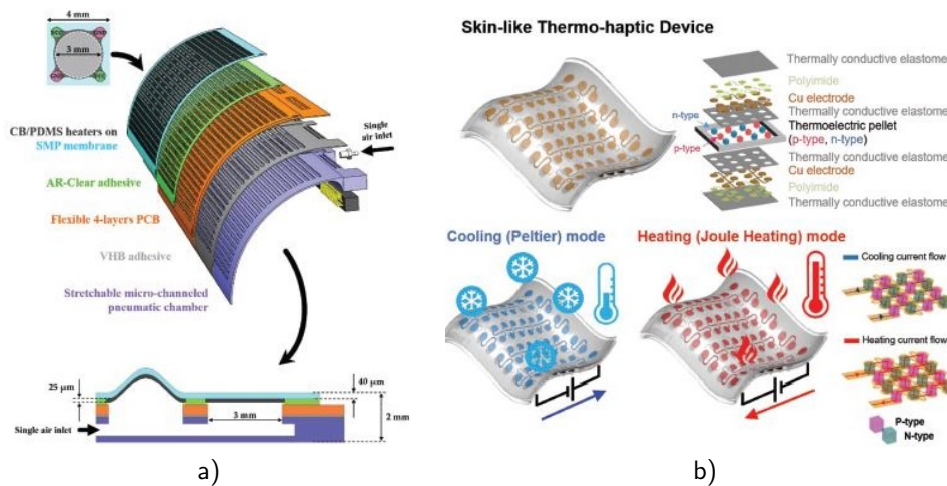
Figure 1.19: a) Pneumatic solution [94]; b) Thermohaptic solution [95].

1.4.4   How to generate a complex haptic effect ?

All of these technologies provide different sensations. Some of them are shape-changing surfaces that allow the creation of relief or topology, while others are more vibrotactile solutions based on combining actuators with a flexible matrix. None of them offers a flexible solution using friction modulation for texture reproduction.

In fact, the solutions presented here do not use wave propagation. However, as seen in the previous section, the use and propagation of waves provides the best haptic rendering, especially with friction modulation. The problem here is that waves are highly attenuated in a soft matrix. It is therefore impossible to develop a fully flexible interface using surface haptics technologies based on wave propagation.

1.5   Haptic interface proposed

Our goal is to obtain an interface able to generate complex sensations, particularly in terms of texture. In view of the state of the art, a friction reduction solution seems to be an interesting option as presented in [63, 64]. Moreover we want also a flexible or semi-flexible solution. However, as we saw in the flexible haptics section, the attenuation of waves in a flexible matrix means that we cannot create a completely flexible solution using friction reduction. The solution proposed for example in [87] is to integrate resonator in a simple or multilayer matrix. Finally the issue is also to propose a continuity or a localization of the haptic feeling by interaction between resonators. As synthesized in the table 1.3, our goal is to propose the first flexible solution using localized or continuous friction modulation with haptic resonators integrated in a soft matrix.

Table 1.3: Positioning of our technology.

	Texture	Flexible	Feeling	
			Localized	Continuous
Ultrasonic lubrication screens [63, 64]	x			x
Metamaterials [71]	x		x	
Flexible device		x	x	
Our technology	**x**	**x**	**x**	**x**

So, to overcome this issue, we decided to work on a hybrid solution combining small rigid haptic

surfaces with ultrasonic lubrication and a flexible and soft matrix, as shown in Fig. 1.20.
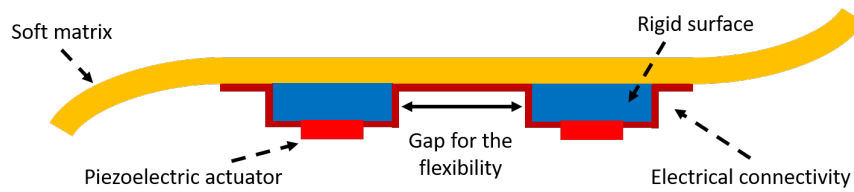
Figure 1.20: Concept of the haptic interface.

Each small rigid haptic surface, actuated by a piezoelectric actuator, hereafter called haptic resonator, allows a localized texture sensation by ultrasonic lubrication. The flexible matrix is placed directly on the haptic resonators and ensures the flexibility of the solution thanks to a gap between the resonators. With this solution, the user's finger is in direct contact with the soft surface and not with the rigid surface, as is the case with rigid touchscreens. A combination of haptic resonators can also be used to create large areas of texture. Thanks to its matrix geometry, this concept makes it possible to localize the haptic texture feedback, thus enabling multi-touch or even multi-user applications. For example, it can be used to create a flexible haptic wristband as shown in Fig. 1.21 or for a larger area as a conformable haptic car dashboard.
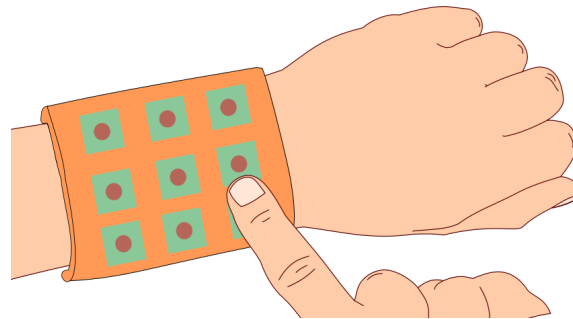
Figure 1.21: Concept of haptic wristband.

In the remainder of the manuscript, the development of this technology is presented. Chapter 2 presents the development of a haptic resonator, and, in chapter 3, the design of a nine-resonators surface is outlined. In chapter 4, the realization of a demonstrator is explained, and the evaluation of the haptic capabilities of this new haptic solution is described in chapter 5.

Chapter 2

Development of a haptic resonator integrated into a flexible matrix

Contents

2.1 Introduction

The main objective of this chapter is to develop and validate the feasibility of a small-scale haptic resonator that integrates friction reduction into a flexible matrix.

The design of the flexible haptic interface is based on a unit cell, named 'haptic resonator' in the remaining of this work, that creates a tactile stimulation with friction reduction on a limited area, and which can be assembled to form a larger area where each unit cell can be energized independently. Therefore, it is necessary to define, validate and evaluate such haptic resonator before implementing

25

it in a large tactile display. The design of the haptic resonator should result in a compelling tactile
feedback on a limited area. For this purpose, its shape, size and material should be adequately chosen
in order to achieve this goal with effectiveness, and our design methodology is described in section 2.2.
Then, we detail in section 2.3 the realization and the validation of the haptic resonators. To be applied
on a flexible haptic interface, the haptic resonator should be able to isolate the tactile stimulation
on a defined area, but also to be connected with others in order to create the larger zone where the
tactile stimuli are connected as wanted. With this regard, we select in 2.4 the polymer sheet that will
compose the flexible matrix of tactile resonators. Finally in 2.5, a tribological study is conducted to
assess friction reduction, followed by a psychophysical evaluation of the haptic resonator in order to
validate the proposed design.

2.2 Design of a haptic resonator

2.2.1 Proposed solution

A haptic resonator is based on a rigid body that puts in vibration the flexible matrix, which is a soft
and thin sheet of polymer material. An actuator bonded to the rigid part generates the forces necessary
for the vibration, leading to the conditions for active lubrication (Fig. 2.1).

Figure 2.1: Concept of the haptic resonator.

To be efficient, the vibration amplitude should be at around 1 μm_{pp} at an ultrasonic frequency,
i.e. above 20 kHz. In the remaining of this work, several decisions were made prior to an optimization
process. First, we decided to define our haptic resonators with a typical area around 1 cm x 1 cm
because it is the average size of a human's fingertip.

The plate could have a variety of geometries such as rectangular, square, circular or polygonal shape
with five or more sides. However, for the purpose of validating the feasibility of the concept, we have
decided to keep it simple and choose only two shapes: rectangular and square. The rectangular shape
was chosen for its similarity to the classical tactile screen used for ultrasonic lubrication [64], while the

square shape was chosen for its simplicity.

For the material, several choices are possible, such as glass, silicon or metal substrate as used by Watanabe to prove the squeeze film effect [56]. We have chosen the glass, because it is commonly used in microelectronic processes, especially for creating touchscreens - a feature that will make our devices easier to build. The glass substrate has a thickness of 500 µm, which is the minimum thickness available.

Various piezoelectric materials are used for actuator applications and can therefore be used for haptic interfaces. These include ceramic or thin-film PZT [65, 66, 67] and AlN [68]. Other materials for actuation are developed and could be used for haptic solutions such as ZnO [96], PVDF [97] or KNN. The table 2.1 shows the main parameters of these materials, adapted from [98].

Table 2.1: Piezoelectric materials.

Materials	Characteristics	Piezoelectric coefficient	
		e_{31} (C/m^2)	d_{31} (pm/V)
PZT	Ceramic or Thin-film / Lead	10-17	150-300
AlN	Thin-film / Lead-free	0.6	2
ZnO	Ceramic or Thin-film / Lead-free	0.6	5.2
PVDF	Thin-film / Lead-free	0.05	24
KNN	Thin-film / Lead-free	6.3	163

For the friction reduction interface, the PZT material is the most interesting. It has the highest piezoelectric coefficients of d_{31}, which characterizes the coupling between deformation and the applied electric field, and e_{31}, which characterizes the coupling between stress and load. These high coefficients guarantee significant displacements on the vibrating surface, thereby resulting in high haptic effects. Moreover, we decide to begin with PZT ceramics that are currently available on the market, ceramics with thicknesses greater than 100 µm. As our technology advances, it may be interesting to consider thin-film or lead-free technologies such as KNN, which have great potential for actuator applications.

We have introduced the concept of the haptic resonator and the assumptions made. The following section will focus on the design of this haptic resonator, starting with the theory of vibrating plates.

2.2.2 Vibrating plates theory

In this section we develop the theory of vibrating plates, in order to understand the key elements of the problem to design these different haptic resonators.

We consider an isotropic homogeneous plate of constant thickness h and infinite lateral dimensions (Fig. 2.2). Since the thickness of the plate is thin, 500 µm, the two Rayleigh waves formed at the two surfaces $h/2$ and $-h/2$ will couple to form a Lamb wave [99, 100, 101].
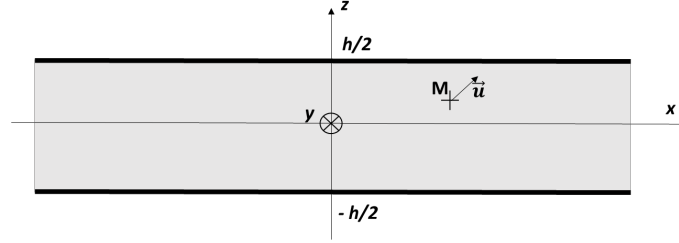
Figure 2.2: Homogeneous plate of thickness h.

If we consider $M(x, y, z)$ a point in the plate, the particle at M undergoes a displacement $u(u_x, u_y, u_z)$ due to the deformation produced by the Lamb waves which are polarized in the plane (x, z) of the plate, and decoupled from horizontal transverse waves (SH) moving along y. The assumption of plane deformation in the (x, z) plane implies $u_y = 0$ and $\partial/\partial y = 0$.

The objective of this part is to obtain the analytical formulation of the displacement vector u. For that purpose, the potential method is adopted, based on the Helmholtz decomposition. The displacement components of a Lamb wave propagating along the x axis are expressed as follows:

$$u_x = \frac{\partial \phi}{\partial x} - \frac{\partial \psi}{\partial z} \tag{2.1}$$

$$u_z = \frac{\partial \phi}{\partial z} + \frac{\partial \psi}{\partial x} \tag{2.2}$$

where the potentials ϕ and ψ validate the wave propagation equations:

$$\frac{\partial^2 \phi}{\partial x^2} + \frac{\partial^2 \phi}{\partial z^2} - \frac{1}{c_L} \frac{\partial \phi}{\partial t^2} = 0 \tag{2.3}$$

$$\frac{\partial^2 \psi}{\partial x^2} + \frac{\partial^2 \psi}{\partial z^2} - \frac{1}{c_T} \frac{\partial \psi}{\partial t^2} = 0 \tag{2.4}$$

with $c_L = \sqrt{\frac{E(1-\nu)}{\rho(\nu+1)(1-2\nu)}}$ the longitudinal wave celerity, $c_T = \sqrt{\frac{E}{2\rho(\nu+1)}}$ the transverse wave celerity, E the Young modulus, ρ the density and ν the Poisson coefficient of the material of the plate.

To solve the equations, harmonic solutions are sought as shown here:

$$\underline{\phi} = \Phi(z)e^{i(kx-\omega t)}, \ \underline{\psi} = \Psi(z)e^{i(kx-\omega t)} \tag{2.5}$$

where k is the wave number and ω the pulsation. We insert these solutions into the equations 2.3, 2.4 and obtain :

$$\frac{\partial^2 \Phi}{\partial z^2} + p^2 \Phi = 0, \ \frac{\partial^2 \Psi}{\partial z^2} + q^2 \Psi = 0 \tag{2.6}$$

with

$$p^2 = \frac{\omega^2}{c_L^2} - k^2, \ q^2 = \frac{\omega^2}{c_T^2} - k^2 \tag{2.7}$$

The normal σ_{zz} and tangential σ_{xz} mechanical stresses are defined after the Hooke's law [101]:

$$\sigma_{zz} = (\lambda_L + 2\mu_L)(\frac{\partial u_x}{\partial x} + \frac{\partial u_z}{\partial z}) - 2\mu_L \frac{\partial u_x}{\partial x} \tag{2.8}$$

$$\sigma_{xz} = \mu_L(\frac{\partial u_x}{\partial z} + \frac{\partial u_z}{\partial x}) - 2\mu_L \frac{\partial u_x}{\partial x} \tag{2.9}$$

with $\lambda_L = \frac{E\nu}{(1+\nu)(1-2\nu)}$ the Lamé's first parameter and $\mu_L = \frac{E}{2(1+\nu)}$ the Lamé's second parameter. Thus introducing with Φ and Ψ in 2.8 and 2.9 :

$$\sigma_{zz} = \mu_L \left[(k^2 - q^2)\Phi + 2ik\frac{\partial \Psi}{\partial z}) \right] \tag{2.10}$$

$$\sigma_{xz} = \mu_L \left[(q^2 - k^2)\Psi + 2ik\frac{\partial \Phi}{\partial z}) \right] \tag{2.11}$$

The boundary conditions of the plate imply that σ_{zz} and σ_{xz} are equal to 0, because the plate is free to move at the upper and lower face. Thus the cancellation of these constraints for $z = \pm h/2$ implies that they must be even or odd. In this way, the solutions are of type :

$$\Phi(z) = A cos(pz + \alpha) \tag{2.12}$$

$$\Psi(z) = B sin(qz + \alpha) \tag{2.13}$$

with $\alpha = 0$ for odd stress and $\alpha = \pi/2$ for even condition.

So, introducing 2.12 and 2.13 in u_x and u_z we obtain for the components of the displacement field:

$$u_x = [ikAcos(pz + \alpha) - qBcos(qz + \alpha)]e^{i(kx - \omega t)} \tag{2.14}$$

$$u_z = [-Apsin(pz + \alpha) + ikBsin(qz + \alpha)]e^{i(kx - \omega t)} \tag{2.15}$$

Symmetrical modes correspond to $\alpha = 0$, i.e. symmetrical u_x longitudinal components and opposite u_z transverse components.
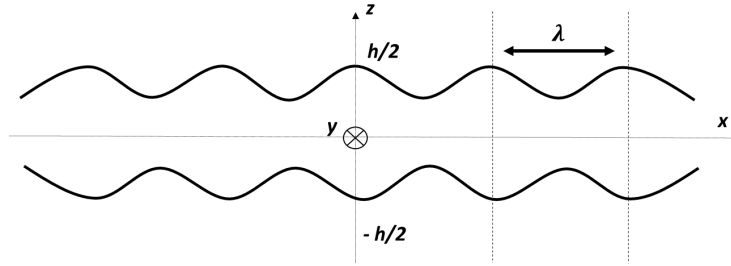
Figure 2.3: Symmetrical plate mode S_0.

Antisymmetrical modes correspond to $\alpha = \pi/2$, i.e. opposing longitudinal components u_x and symmetrical transverse components u_z. These modes are flexural modes, as the mean plate displacement is normal to the median plane.
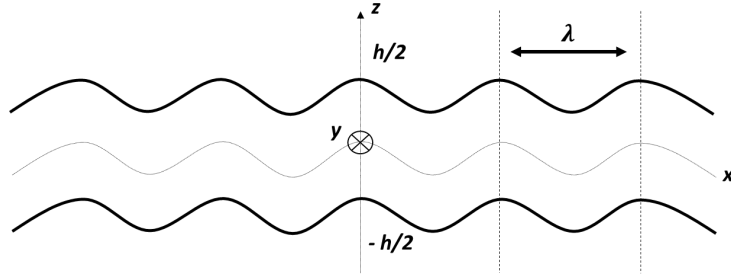
Figure 2.4: Antisymmetrical plate mode A_0.

Here again, we consider $\sigma_{zz} = 0$ and $\sigma_{xz} = 0$. Introducing 2.14 and 2.15 into 2.10 and 2.11 leads to :

$$(k^2 - q^2)Acos(p\frac{h}{2} + \alpha) + 2ikqBcos(q\frac{h}{2} + \alpha) = 0 \tag{2.16}$$

$$(q^2 - k^2)Bpsin(p\frac{h}{2} + \alpha) - 2ikqAsin(q\frac{h}{2} + \alpha) = 0 \tag{2.17}$$

An obvious solution is $A = B = 0$. The other solutions are those canceling the determinant of the system formed by the two equations 2.16 and 2.17 which is :

$$-(k^2 - q^2)cos(p\frac{h}{2} + \alpha)sin(q\frac{h}{2} + \alpha) - 4k^2qpcos(q\frac{h}{2} + \alpha)sin(p\frac{h}{2} + \alpha) = 0 \qquad (2.18)$$

After simplifications with 2.7 we obtain the dispersion relation of the Lamb waves :

$$\frac{\omega^4}{c_T^4} = 4k^2q^2(1 - \frac{p}{q}\frac{tan(p\frac{h}{2} + \alpha)}{tan(q\frac{h}{2} + \alpha)}) \qquad (2.19)$$

Then, using a numerical method, we find the pairs $(\omega$, k) of each mode. Fig. 2.5 presents the evolution of the phase velocity $V_\Phi = \omega/k$ and the wave number of the Lamb modes for a 500 µm thick glass plate.
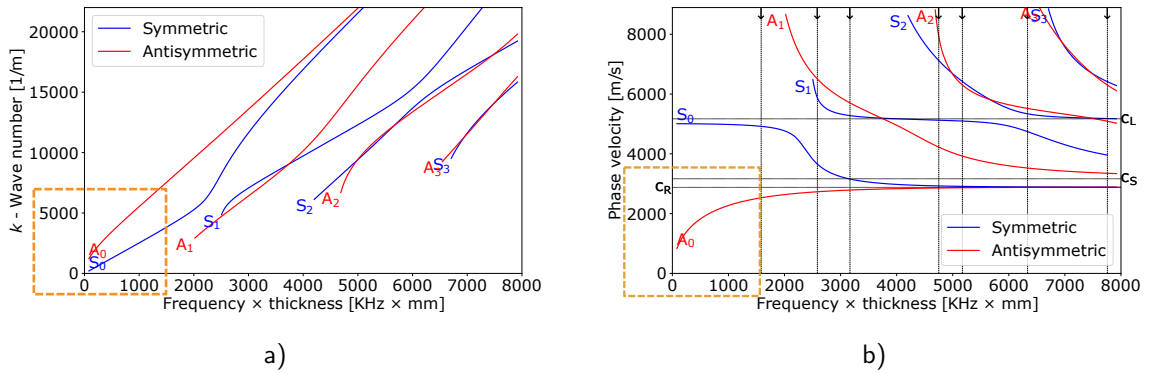
Figure 2.5: a) Wave number evolution for the Lamb mode of a glass plate; b) Phase velocity evolution for the Lamb mode of a glass plate.

These curves show the dispersive nature of Lamb waves. The wave vector is non-linear with frequency. The phase and group velocities (not plotted here) also vary with wave frequency. As shown earlier, the thickness of the plate is 500 µm. If we assume a frequency below 1 MHz for the resonator we see in Fig. 2.5 that the modes A0 and S0 are both possible. The other mode cannot be obtained for this range of frequency x thickness.

Therefore, the remaining of this chapter presents the design of a haptic resonator, that exploits the modes A0 and S0. This design will define the operating frequency f, the wavelength λ and the resonator's length L. But first of all, the objectives and constraints to this design are precised.

2.2.3 Constraints and methodology

An optimization loop requires constraints to be defined for the design variables. In this section and in Fig. 2.6, we describe the constraints for f, λ and L and the methodology used to design and optimize haptic resonators.
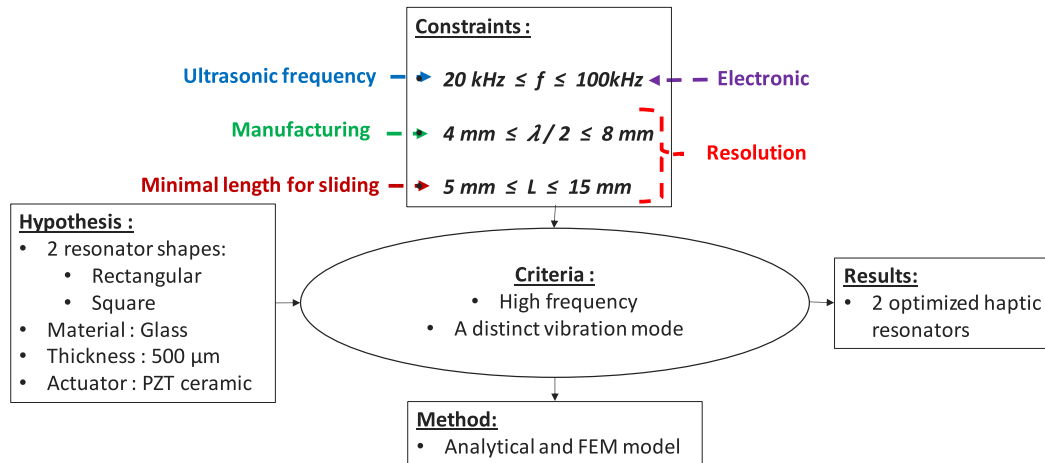
Figure 2.6: Methodology to design two haptic resonators.

As explained before we want a small-size haptic resonator with a good resolution. This is why we decided to define our haptic resonators with an area close to 1 cm x 1 cm which is the size of a human's fingertip. However, the exact size of the haptic resonator is made variable between a upper and a lower value, in order to allow the optimization of the device. The maximum value is arbitrary set to 15 mm, while the minimum value is set at 5 mm, in order to allow the finger to slide over it. Because we exploit ultrasonic lubrication in the device, the vibrating plate has to vibrate in an ultrasonic mode with a frequency above 20 kHz. However, because electronic becomes more difficult to realize when the frequency is high, we limit the operating frequency below 100 kHz. Optimization design of ultrasonic tactile device have shown that the half-wavelength of the vibration should be smaller than the size of user's finger. Otherwise, vibration nodes may be felt when sliding across the vibration. Therefore, we set $\lambda/2 \leq 8\ mm$. The lower limit is defined by the manufacturing process. The actuator often has the same size as $\lambda/2$. Because we want to use commercial piezoelectric ceramics, a minimal size of 3 mm is purchasable. Therefore, we set the minimal half-wavelength to 4 mm, leading to $4\ mm \leq \lambda/2 \leq 8\ mm$.

The two criteria selected for the optimization algorithm are to show a vibration mode clearly sepa-

rated to its neighboring one and to get the highest resonant frequency. Indeed, it has been shown in [61] that increasing the operating frequency results in better ultrasonic lubrication.

This methodology will be used in order to design two types of devices : one rectangular and one square.

2.2.4 Design of a rectangular resonator

Design of a rectangular plate

Since $20\ kHz \leq f \leq 100\ kHz$, frequency have to be between 20 kHz and 100 kHz. The phase velocity $V_\Phi = \frac{\omega}{k} = \frac{2\pi f}{\frac{2\pi}{\lambda}} = f\lambda$ has for maximum $100\ kHz * 16\ mm = 1600\ m/s$. At this velocity the mode S0 is impossible as observed on Fig. 2.5.b). Thus the A0 mode is chosen.

Since the frequency will remain lower than 100 kHz, and the wavelength will be longer ($\lambda/2 \geq 4$ mm) than the substrate thickness (500 µm), we can analyze the asymptotic behavior of the dispersion relation for an antisymmetric mode A0, i.e. when $k \to 0$ and $\omega \to 0$. Thanks to a limited development of the tangent function, we have :

$$\frac{\omega^4}{c_T^4} \approx 4k^2q^2(1 - \frac{1 - p^2h^2/12}{1 - q^2h^2/12}) \approx \frac{4}{3}h^2k^2q^2(p^2 - q^2) \tag{2.20}$$

We therefore obtain the dispersion relation by replacing the coefficients p and q :

$$\omega = \frac{c_P}{\sqrt{12}}k^2h \tag{2.21}$$

with $c_P = 2c_T\sqrt{1 - \frac{c_T^2}{c_L^2}}$

Again by replacing c_P in 2.21 with the value of c_T and c_L defined in 2.3 and 2.4, we find the dispersion relation of a flexural wave according to a Kirchoff model :

$$\omega = \sqrt{\frac{Eh^2}{12\rho(1 - \nu^2)}}k^2 \tag{2.22}$$

For this low-frequency A0 mode, the flexural mode $(n,0)$ is defined by its number of nodes n in the desired direction. For example in Fig. 2.7, an A0 mode with 12 nodes for a plate of glass with a thickness of 500 µm and an arbitrary length L simulated with COMSOL is presented.
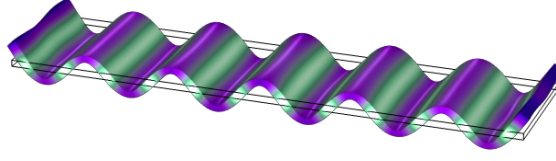
Figure 2.7: Example of an A0 mode for a plate of glass with arbitrary dimensions.

This finite dimension L imposes the cancellation of stresses at the ends of the plate, i.e. in $\pm L/2$. In this way it can then be shown that k takes discrete values :

$$k = \frac{\pi}{L}(n + \frac{1}{2}) \tag{2.23}$$

By introducing 2.23 in 2.22 the equation defining our resonant frequency to obtain the A0 modes, in this case flexural because at low frequency, as a function of the plate length L and the number of nodes become :

$$\omega = \sqrt{\frac{Eh^2}{12\rho(1 - \nu^2)}} \left(\frac{\pi}{L}(n + \frac{1}{2})\right)^2 \tag{2.24}$$

In equation 2.24, the width of the plate is not taken into account. In this work, a width of 10 mm is set arbitrary, as it corresponds to the width of a fingertip. We calculate the resonance frequency of a glass plate ($E = 65\ GPa$, $\rho = 2300$ kg/m^3 and $\nu = 0.2$) with a thickness h = 500 µm, a width of 10 mm and a length L ranging from 11 mm to 15 mm. For each length, we note the resonance frequency of the A0 mode and the half wavelength, which are plotted in Fig. 2.8 as a function of the number of vibration nodes on the plate.

Fig. 2.8 shows that increasing the number of vibration nodes increases the resonance frequency, but also decreases the half wavelength. In this figure, the design that fulfills the constraints in frequency and wavelength, with the highest frequency is for f= 66.9 kHz with L = 15 mm and $\lambda/2$ = 4.3 mm. Another solution could be L = 14 mm and $\lambda/2$= 4 mm, for f= 76.8 kHz. However, the aim here is to have a Lamb A0 mode with well-paralleled vibration nodes. For this purpose it is preferable to have the longest possible length. The closer the length and width, the more distorted the A0 mode [102]. For this reason, 15 mm is preferred to 14 mm. However, practically, the geometrical manufacturing precision would allow $14\ mm \leq L \leq 15\ mm$ to still fulfill the constraints, which is acceptable.
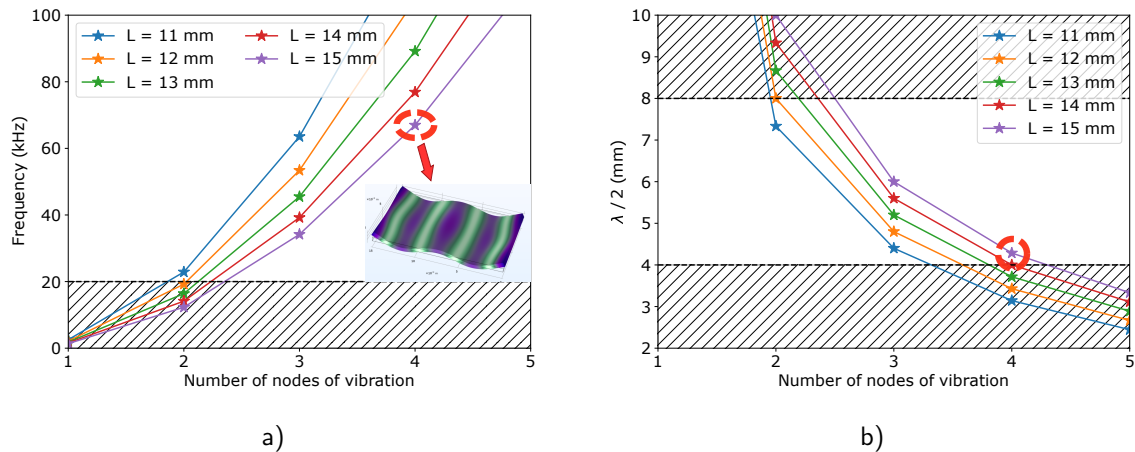
Figure 2.8: Evolution of Lamb A0 modes as a function of the length L and the number of nodes.

For the value of $L = 15$ mm we calculate with COMSOL all the vibration modes. The A0 mode is confirmed for $f = 66.9$ kHz and presented in Fig. 2.8.a). The previous plate mode obtained is at 52.2 kHz and the next is at 75.5 kHz. This provides a wide enough frequency band to activate the mode without interfering with either plate mode.

Thus, we select a glass plate that measures 10 mm x 15 mm x 500 µm.

Addition of an actuator

These results are obtained without the piezoelectric actuator that will create the vibration. To be efficient, the actuator should be placed on and limited to an antinode of vibration. Since the selected vibration mode has three vibration antinodes, we have decided to use only one actuator, placed on the central antinode. Finally, we selected a PZT ceramic with a width of 3 mm and a thickness of 200 µm after a study of the products available on the market. Again COMSOL is used as the simulation software, and the vibration mode at 66.9 kHz is presented in Fig. 2.9, actuated by its PZT actuator.
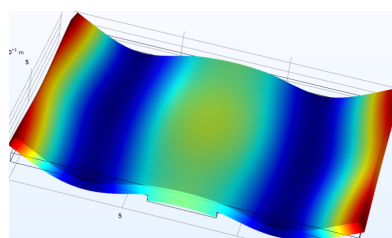
Figure 2.9: Displacement field at resonance with the PZT actuator.

This result shows that even with the actuator, the resonance frequency has not shifted and the condition on $\lambda/2$ is maintained. With the ceramic added, the lower mode has shifted to 49 kHz, becoming the closest mode, while the upper mode is no longer reachable. So the mode is well separated. This validates the design.

2.2.5 Design of a square resonator

Design of a square plate

Due to its geometry, the square plate is a special case of the rectangular plate, where the width is equal to the length. As a result, the square plate can be considered in the same way as the rectangular plate but with different vibration modes. In this section, we will select a specific mode of vibration of the square plate and design this plate to meet the requirements of the application and compare it with the previous designed rectangular plate of section 2.2.4.

The first vibration modes of a free-free square plate are known from Chladni's figures (1787), as presented on Fig. 2.10 for an example of a square plate. Each mode is a combination of two transverse modes solving the wave equation in the x and y directions simultaneously. Thus, obtaining a square plate vibration mode is equivalent to combining two rectangular plate vibration modes. The order of appearances of these modes can vary according to the material and its dimensions.
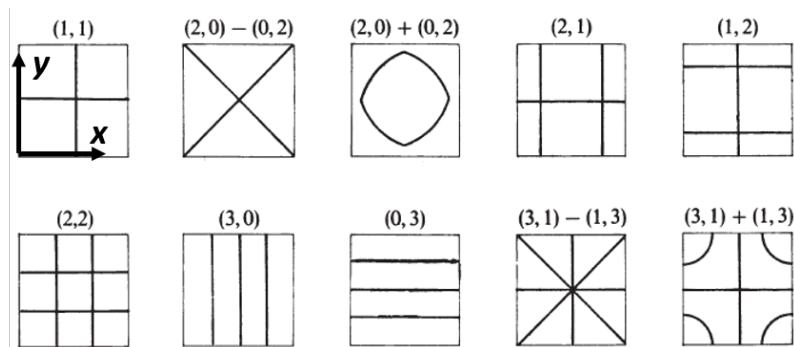
Figure 2.10: First eigenmodes of a square plate with nodal lines [103].

The nodal lines of the vibration modes are thus found along the two axes of the plane. The first two modes do not appear to be of interest because there is a node of vibration at the center. The third mode (2,0) + (0,2), which combines two nodal lines in the two main directions shows a vibration antinode

in the center of the plate. Thus a cylindrical PZT ceramic placed at the center of vibration would easily actuate this mode. Fig. 2.11 shows how to combine this mode, taken from [103]. Conversely, the following modes do not seem very interesting.
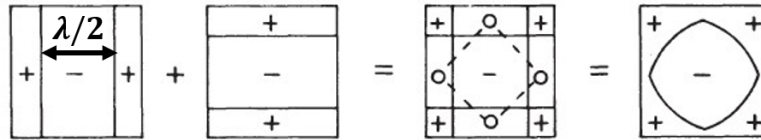
Figure 2.11: Plate mode selected for the square resonator.

Various works, by Leissa [104], Waller [102] and others, have made it possible to quickly approximate the first vibration modes.

$$\omega = \beta \sqrt{\frac{Eh^2}{\rho L^4 (1 - \nu^2)}} \tag{2.25}$$

With L the size of the square and β a variable coefficient depending on the mode of the free-free square plate [105], $\beta = 6.91$ for the (2,0+0,2). The previous mode (2,0 - 0,2) corresponds to $\beta = 5.94$, indicating a 14 % decrease in frequency, while the next mode (2,1 - 1,2) corresponds to $\beta = 10.39$, indicating a 50 % increase in frequency. Therefore, the selected mode (2,0+0.2) appears distinct from the other modes. This will be confirmed with the choice of the length L.

From these values, the evolution of the frequency of the mode (2,0+0,2) for $h = 500$ µm and as a function of its side L is plotted Fig. 2.12.
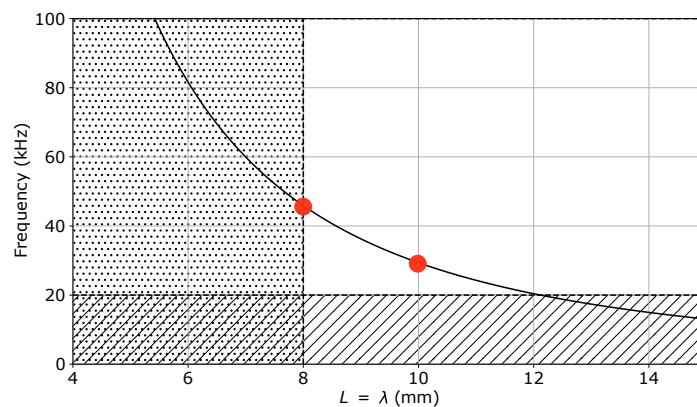
Figure 2.12: Evolution of the frequency for the (2,0 + 0,2) mode.

As previously stated, the objective is to achieve the highest possible frequency, which requires reducing the size of the square resonator in this condition. In the case of a square plate, the length of the plate L is equal to the wavelength since there are modes (2,0) in each direction. Therefore, the minimum length of the plate is $L \geq 8$ mm to satisfy the constraint on the half-wavelength.

Since the frequency increases when L decreases, and because the frequency for $L = 8$ mm is inside the frequency constraint, $L = 8$ mm is chosen. The approximated resonance frequency is then $f = 45.9$ kHz. However, we also considered $L = 10$ mm, for manufacturing purposes as presented in the remainder of this chapter, which leads to $f = 29.8$ kHz.

A COMSOL eigenmode analysis of the two square glass resonators is then conducted. The frequencies obtained by approximation with the equation 2.25 agree with the FEM model in COMSOL. The selected mode has a frequency of 29.8 kHz for the 10 mm x 10 mm resonator. The nearest neighbor mode is the mode (2,0-0,2) for $f = 25.5$ kHz in this situation. For the 8 mm x 8 mm resonator, the mode selected is for $f = 46.6$ kHz and the nearest mode, (2,0-0,2), is at 40.4 kHz. The differences between the selected mode and their nearest modes corresponds to a decrease of 14 % as expected with $\beta = 5.94$ in the equation 2.25.
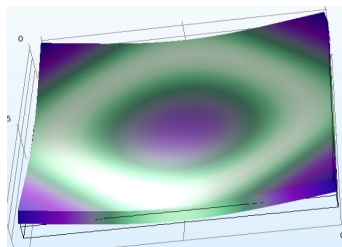
Figure 2.13: Mode selected for the 10 mm x 10 mm x 500 μm square plate.

On Fig. 2.13 we observe the mode for the 10 mm x 10 mm resonator. It shows a vibration antinode in the center of the plate. Therefore, to actuate the plate, an unique piezoelectric cylinder will be placed in the center. In the next section, the actuator is selected from the commercial products available in the market.

Addition of an actuator

For the cylindrical PZT actuator, a radius of 2.5 mm is chosen, corresponding to the radius of the vibration antinode. As for the rectangular PZT ceramic, a thickness of 200 μm is selected according

to market availability.

After adding the PZT actuator, the vibration mode at 29.8 kHz is confirmed with COMSOL and shown in Fig. 2.14. In addition, the nearest mode (2.0-0.2) is no longer present. The PZT actuator with its central placement prevents this mode from occurring. The closest mode is now a mode at 79.1 kHz.
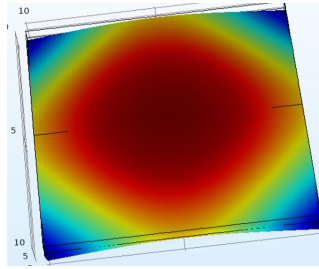
Figure 2.14: Displacement field at resonance with the PZT actuator for the 10 mm x 10 mm resonator.

The same is done for the 8 mm x 8 mm resonator. The goal is to have a ceramic with a diameter of 4 mm or less. Since a 3 mm diameter ceramic is easily available on the market, we choose a 3 mm diameter actuator with a thickness of 200 µm. Validation is also performed with COMSOL, which confirms the frequency and the distinct mode.

2.2.6   Resonator dimensions

To sum up, two different haptic resonators with the characteristics shown in the table 2.2 have been selected and sized. These haptic resonators will now be realized and their efficiency tested.

Table 2.2: Resonator dimensions.

	Rectangular resonator	**Square resonator**
Material	Glass-500µm	Glass-500µm
Size	10 mm x 15 mm	10 mm x 10 mm / 8 mm x 8 mm
Resonance frequency	66.9 kHz	29.8 kHz / 46.6 kHz
Actuator	PZT ceramic	PZT ceramic
Actuator size	10 mm x 3 mm x 200 µm	Ø 5 mm x 200 µm / Ø 3 mm x 200 µm

2.3 Realization and validation of resonators

2.3.1 Realization

In both cases, a glass substrate (Eagle XG) with a diameter of 200 mm and a thickness of 500 µm is cut to the desired dimensions in the cleanroom at CEA-Leti. PZT ceramic (PI 255) is then bonded to the desired areas using UV epoxy glue. The actuator is aligned by hand in the center of the resonator. Thus, for the square resonator, we prefer to focus on the larger dimensions of 10 mm x 10 mm. When manufacturing becomes more mechanized in chapter 4, we will also produce 8 mm x 8 mm resonators. Finally, two wires are soldered to the two ceramic electrodes. Fig. 2.15 displays the two types of resonators created.
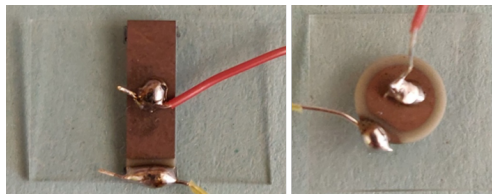
Figure 2.15: a) Rectangle resonator; b) Square resonator.

2.3.2 Electromechanical evaluation

Using an impedance analyzer (HP 4194A), the impedance of the equivalent circuit formed by the PZT ceramic and the glass plate, based on a Butterworth Van Dyke (BVD) model, is measured for each type of resonator. In this way, the resonator is electrically modeled by an electrical capacitance C_0 associated in parallel with a branch RLC corresponding to the mechanical part of the resonator (Fig. 2.16). This
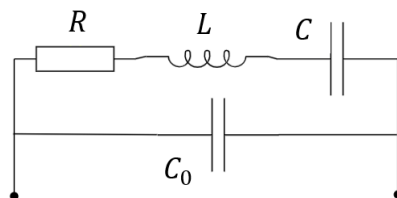
Figure 2.16: Butterworth Van Dyke model for a piezoelectric transducer.

allows us to calculate the impedance of the haptic resonator:

$$Z = \frac{1}{j\omega C_0} / (R + j\omega L + \frac{1}{j\omega C}) \tag{2.26}$$

that is :

$$Z = \frac{R + j\omega L - \frac{j}{\omega C}}{1 - \omega^2 C_0 L + \frac{C_0}{C} + j\omega R C_0} \tag{2.27}$$

With the pulsation at resonance ω_r and at antiresonance ω_a :

$$\omega_r = \sqrt{\frac{1}{LC}} \tag{2.28}$$

$$\omega_a = \omega_r \sqrt{1 + \frac{C}{C_0}} \tag{2.29}$$

The impedance modulus obtained is compared to the model developed in COMSOL. The surface displacements at resonance are measured using a SIOS laser vibrometer (LSV 2500 NG).

Rectangular resonator

As shown in Fig. 2.17, the impedance modulus plot confirms the presence of the A0 mode at 65 kHz. The small variation between the measurement and the model, 65 kHz instead of 66.9 kHz, could be due to uncertainties in the resonator dimensions caused by the glass dicing, the misplacement of the actuator and the electrode wire welding. The A0 mode is distinct from the nearest mode at 48.2 kHz.
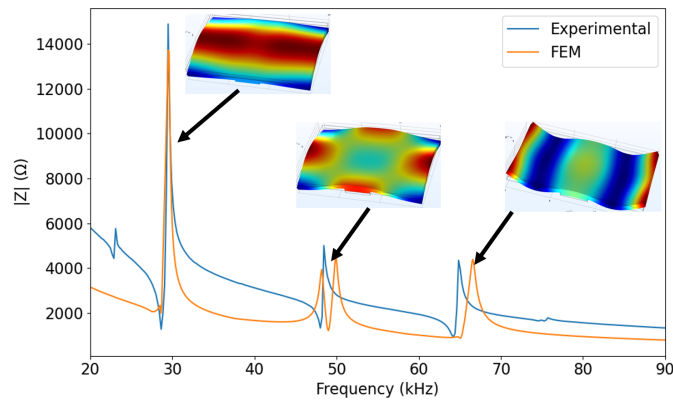
Figure 2.17: Rectangular resonator impedance compared with COMSOL model.

For the chosen A0 mode, a single spot laser measurement is carried out, and we measured a maximal displacement of 1.1 μm for a voltage amplitude of 20 Vpp. Hence, the measurements confirm the simulation. The actual rectangular plate is similar to the digital prototype, and the resonance frequency matches the simulated one.

Square resonator

The same measurements were carried out on the square resonator. The impedance analyzer measurement shows the resonance at 28.6 kHz in Fig. 2.18, instead of 29.8 kHz with our FEM study.

Moreover we see that due to the addition of the PZT actuator the mode is well isolated. The nearest mode is at 77.3 kHz instead of 79.1 kHz for the FEM model on COMSOL.
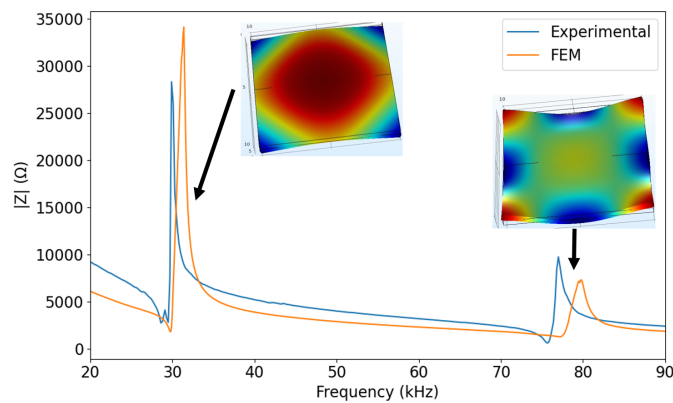
Figure 2.18: Square resonator impedance compared with COMSOL model.

A laser vibrometer measurement confirms displacements of 1.2 μm at 20 Vpp at resonance.

2.3.3 Selection of the design

The two haptic resonators were briefly evaluated from the perspective of the tactile feeling they produce in several test conditions: with a constant voltage amplitude (100 Vpp) or with an amplitude modulated voltage (from 50 Hz to 500 Hz). The tactile perception was very similar for both designs, even if the working frequencies are different. This may justify the constraints defined in section 2.2.3, which may lead to haptic resonators with similar performances. However, this test shows that considering only the haptic performance only is not enough to prefer one design or the other.

The square structure appears more suitable for creating a flexible and conformable interface obtained by repetition of the same pattern. Indeed, the rectangular structure has a predominant direction due to the difference in length between its sides, resulting in a dominant direction in the bending of the surface, not the square structure. Additionally, the square structure is easier to obtain than the rectangular one. It is easier to center the circular PZT ceramic in the middle of the square structure than to center the rectangular PZT ceramic on an A0-mode vibration antinode of the rectangular structure. In fact, a small geometric defect will greatly alter the A0 mode and thus the location of a vibration antinode. Also, the square resonator with its out-of-plane mode has never been used to create a friction-reducing haptic interface, making it innovative.

Therefore, the design of the flexible tactile display continues with the square haptic resonator in the next section of this chapter.

2.4   Identification of the flexible matrix

Once the haptic resonators have been selected and designed, the next step is to identify the flexible layer that will connect them together to form the flexible tactile display. First, the material of this layer is selected. Then we characterize the friction modulation to confirm that this layer can transmit the ultrasonic vibrations.

2.4.1   Selection of some polymer films

Several polymer films used in electronics processes are selected for testing in our application. These films are a poly ether ketone (PEEK) film, a KAPTON polyimide film, a PET polyester film and a polycarbonate (PC) film. They have different mechanical properties as shown in the table 2.3 (E_p, ρ_p, ν_p). PEEK and KAPTON films have been widely used in microelectronics and are particularly popular as thermal insulation films due to their high thermal stability. These materials are capable of withstanding temperatures in excess of 200°C. PC and PET films, on the other hand, are transparent but less resistant to high temperatures (maximum 140°C).

Table 2.3: Selected polymer characteristics.

Materials	E_p (GPa)	ρ_p (kg/m^3)	ν_p
PC	2.2	1200	0.3
PET	5	1390	0.37
PEEK	3.5	1350	0.4
KAPTON	3	1420	0.4

2.4.2 Identification of the best polymer film for our application

In this section, our objective is to determine which polymer(s) will provide the most satisfying tactile experience. This is due to the fact that the user's finger will be in contact with this material. We therefore need to ensure that the feeling is satisfying. However, we also have to select a material that will attenuate vibrations the least.

FEM study

A Finite Element Method (FEM) study is conducted in COMSOL to analyze the behavior of the four chosen polymers that are used in the haptic resonator, as illustrated in Fig. 2.19. The model assumes that the polymer plate edges are free, while the adhesive layers are excluded. The PZT ceramic (PZT-5A on COMSOL) is supplied with a 20 Vpp voltage. An isotropic damping of 0.014, obtained from experimental measurements on the resonator without polymer, is taken into account in the glass for the COMSOL model. For each polymer film, an isotropic damping of 0.2 is also used. This represents the damping of both the polymer film and the adhesive layer, not simulated here.
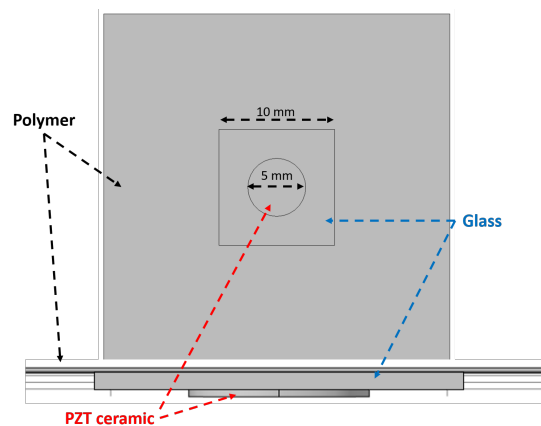
Figure 2.19: Assembly geometry created on COMSOL.

The study highlights the propagation and damping of vibrations in the polymer. The propagation behavior is uniform for each polymer. The vibrations of the haptic resonator generate a flexural wave on the polymer film, as shown in Fig. 2.20, which provides an example for the PEEK film. Further examination of this flexural wave will be presented in the subsequent chapter.
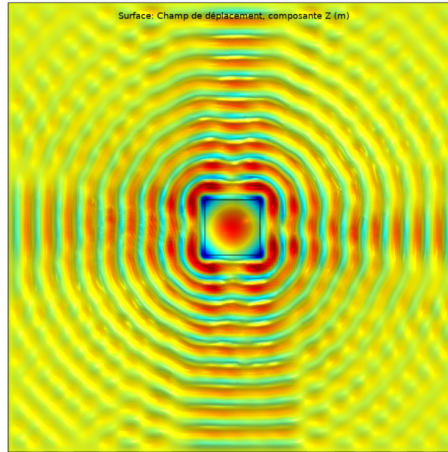
Figure 2.20: Displacement field for the resonance obtained for a PEEK film with the model.

Moreover, the characteristics of each polymer induce slight changes in the resonant frequency and displacement amplitude. The first resonant frequency shifts to a lower frequency, as shown in Fig 2.22 and Table 2.4. This shift occurs because adding a polymer layer is equivalent to adding a mass to the vibrating square plate, resulting in a decrease in frequency.

Additionally, the inclusion of the polymer film alters the RLC branch that corresponds to the mechanical aspect of the resonator of the BVD model. Consequently, the equivalent resistance R increases. Thus, reducing the equivalent resistance R mitigates the impact of the polymer film on the resonator. At resonance, the impedance Z is equivalent to the resistance R [106]. Thus, minimizing the impedance modulus $|Z|$ corresponds to minimizing the resistance caused by the polymer film. For this point, it is evident that PC is not as effective as the other three polymers, as the absolute value of $|Z|$ at resonance is significantly higher. This difference can be attributed to the larger thickness of the PC film, which is 175 µm compared to 100 or 75 µm for the other polymers.

KAPTON and PEEK films exhibit the most significant impedance variation $\Delta|Z|$ between resonance and antiresonance, and have the narrowest bandwidth Δf between these frequencies. As a result, assemblies containing PEEK or KAPTON have a superior quality factor than the assembly with the

PET film.

Thus for the PC and the PET, the films disturb more the resonance of the plate and add more attenuation (Fig. 2.22).

Experimental study

To confirm this study, each polymer is integrated with a glass plate and a PZT ceramic previously studied by using the epoxy EPOTEK OG116-31 glue (Fig. 2.21). For each polymer film five assemblies are done in order to limit the impact of the dispersion of the fabrication on the results.
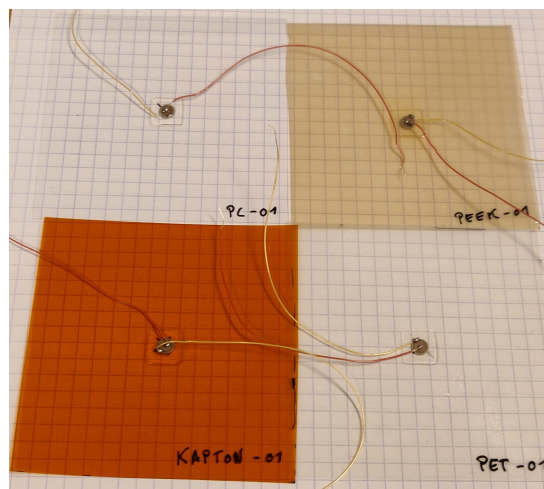
Figure 2.21: Polymer film assemblies.

The mean absolute impedance is then plotted for the first resonance and compared to the impedance of the FEM model as shown in Fig. 2.22.

The results align between the COMSOL study and the experimental measurements. The PEEK and KAPTON films are the most appropriate. However, there was a slight discrepancy in the resonance frequencies between simulation and experiment. The main reason is that the model excluded the adhesive layer and the solder wires. The discrepancy could also be attributed to the uncertainty in the dimensions of the glass plate due to cutting. In addition, these add resistance and damping that change the impedance.

The amplitude of vibration at resonance for each sample is measured with a laser vibrometer for a sinusoidal signal of 20 Vpp and averaged over the five samples per polymer. These results are listed in
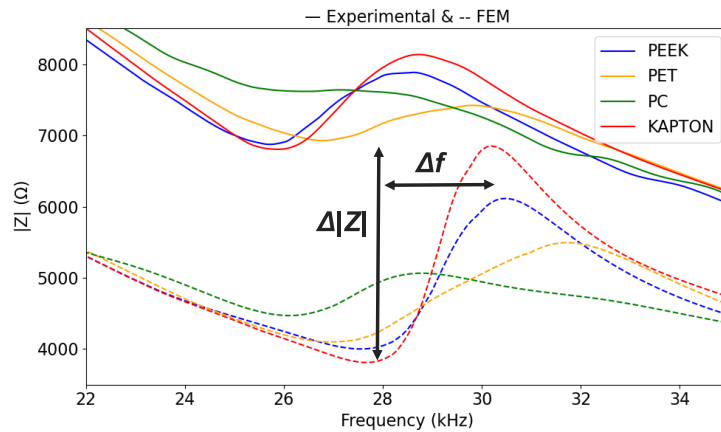
Figure 2.22: Impedance modulus obtained with the FEM study (- -) and experimental (−) results.

table 2.4.

Table 2.4: Resonance frequency (FEM and experimental) and maximal displacement measured.

	Resonance frequency (kHz)		Maximal displacement
	FEM	Experimental	(μm)
Without Polymer	29.8	28.6	1.2
PC - 175 μm	26.1	25.7	0.5
PET - 100 μm	27	26.8	0.6
PEEK - 100 μm	27.6	25.8	0.9
KAPTON - 75 μm	27.7	25.9	0.8

A mapping of the elementary haptic resonator is also carried out for one sample of each polymer film, with a Polytec OFV-5000 modular vibrometer base with a sensor head OFV-505 and with a resolution of 0.5 mm, as presented in Fig. 2.23.

The displacements, measured at 20 Vpp, reach almost 1 μm for the KAPTON and PEEK films. This clearly shows that haptic feedback will still be possible, despite the add of a layer of adhesive and a polymer film that act as a vibration-damping layer. With a better manufacturing process the efficiency of the solution will be improved. Finally the propagation of the wave in the polymer sheet is confirmed as observed on the FEM model, and exploited in the next chapter to create the flexible haptic surface.

To sum up KAPTON and PEEK films are selected as the flexible matrix of the haptic resonators. The haptic feeling of this new solution will now be tested by a tribological study followed by a psychophysical study.

a)   b)
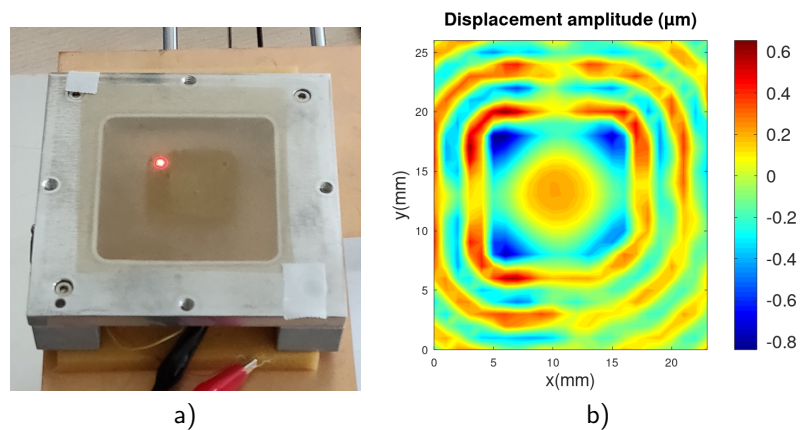
Figure 2.23: a) Setup for measurement ; b) Displacement amplitude for the mode of vibration (PEEK assembly - 20 Vpp).

2.5   Quantification of the haptic response

The aim is to validate the friction reduction and tactile detectability of the developed solution.

2.5.1   Quantification of the friction reduction

To validate the ability of a haptic resonator to produce a reduction in friction under active touch conditions, a tribological study is carried out.

Protocol

To this end, a resonator is mounted on a rigid frame, and a 3-axis sensor (K3D40 Me-System) placed under the surface is used to measure the normal F_n and tangential F_t forces produced by the finger on the polymer sheet, Fig. 2.24, thus enabling the calculation of the friction coefficient $\mu = F_t/F_n$.
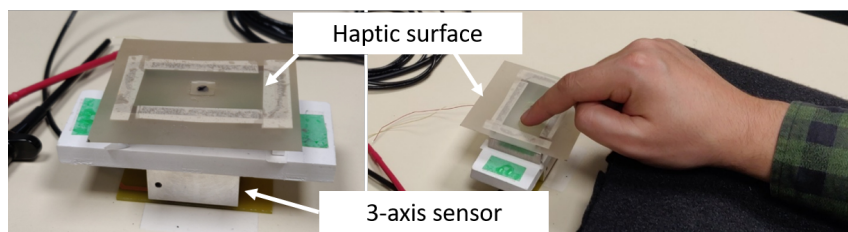
Figure 2.24: Setup for the tribological study.

A sinusoidal voltage at the first resonant frequency of the haptic resonator is modulated by a 5 Hz square signal in order to create the friction modulation. The voltage amplitude is set between 20 V peak to peak (20 Vpp) to 140 Vpp. 8 subjects take part to this experiments. During the tests, the participants explore the surface laterally during 20 s at a velocity of 50 mm/s, while applying a normal force F_n of 0.2 N. To ensure the velocity and the normal force, a training phase is performed for each participant.

Results / Discussion

The typical response for one participant is depicted in Fig. 2.25.a) with a voltage of 100 Vpp and corresponding to one swipe across the surface. It should be emphasized here that the friction reduction produced by the ultrasonic vibration occurs all over the haptic resonator, and not only on top of the plate, as expected from the results of Fig. 2.23.
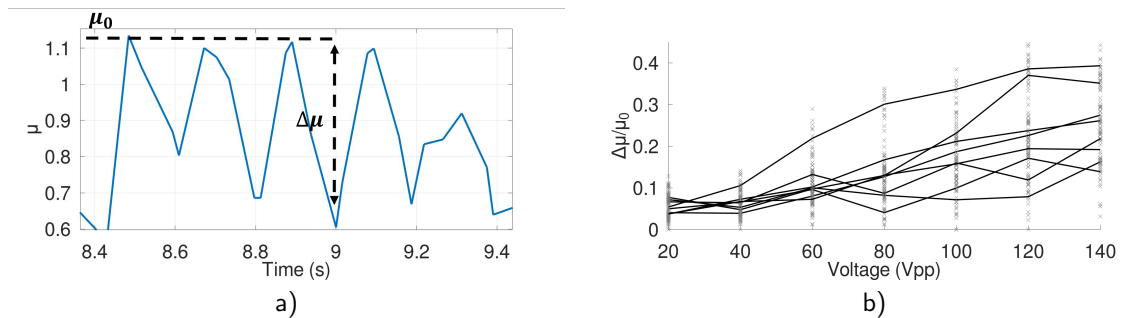
Figure 2.25: a) Friction coefficient during 1 s for one subject at 100 Vpp; b) Friction contrast at different applied voltage for each subject.

The friction contrast $\Delta\mu/\mu_0$ [107] is then calculated and plotted for the 8 subjects in Fig. 2.25.b) as a function of the applied voltage. On each graph a cross represents a value of the friction contrast on a swipe of the surface. The median of these values is then plotted. As expected, the friction contrast increases as the applied voltage increases. However, depending on the participants, the friction contrast evolves in a more or less important way. It hardly reaches 0.2 for some participants while for others it reaches 0.4 at 140 Vpp. The sweep velocity may have been too high. Indeed, the sweep velocity plays a very important role in the performance of friction reduction [60].

The friction reduction has been quantified for this prototype haptic resonator. A more extensive tribological study will follow when a complete surface is realized.

2.5.2 Psychophysical evaluation

We now want to evaluate the discrimination of haptic resonators through a study with two independent resonators. The idea is to see if the sensation is well localized and detectable by the user. For that purpose, we have conducted a psychophysical study on the two haptic resonators prototype of Fig. 2.26.a).

Protocol

The protocol is as follows. We energize the left (L) resonator, or the right (R) resonator or none (∅). The solution where both resonators are energized is not evaluated since we aim to validate the perception of a single haptic resonator. The voltage supplied to the plates is at a voltage amplitude $V = [20, 30, 40, 60, 80]$ Vpp and is modulated by a square signal at a frequency $f_m = [50, 250, 500]$ Hz. Participants are presented with each condition, in a random order, and each set is repeated 10 times, leading to $3 \times 3 \times 5 \times 10 = 450$ tests. The experiment duration is approximately 60 minutes. Data were collected from 9 consenting and inexperienced volunteers (3 females and 6 males) between 22 and 28 years old. Participants were asked to slide their index finger across the entire surface, were phonically isolated with headphones playing white noise, and were blindfolded. They were asked to answer 'L', 'R' or 'None', depending on where they perceived the stimulus.

Results / Discussion

As expected and presented in Fig. 2.26.b), the mean correct ratio answer increases when the voltage applied to the PZT ceramics increases, this voltage being directly related to the vibration amplitude of the resonator. This rate reaches 1 above 80 Vpp. The modulation at 250 Hz allows to have the best rates of correct answers. This was also expected since this frequency is the optimal frequency for detection with the haptic sensation finger [11]. Thus for an applied voltage of 30 Vpp, the mean correct answer ratio reaches 92 %.

The confusion matrix is given for a voltage of 40 Vpp in Fig. 2.27. The resonator R seems less detectable. This might be due to a lower vibration amplitude than for L resonator, which can be due to an incorrect driving frequency. However, this does not affect the study carried out.

Hence this study validates the concept of haptic resonator for a flexible haptic surface. The sensation
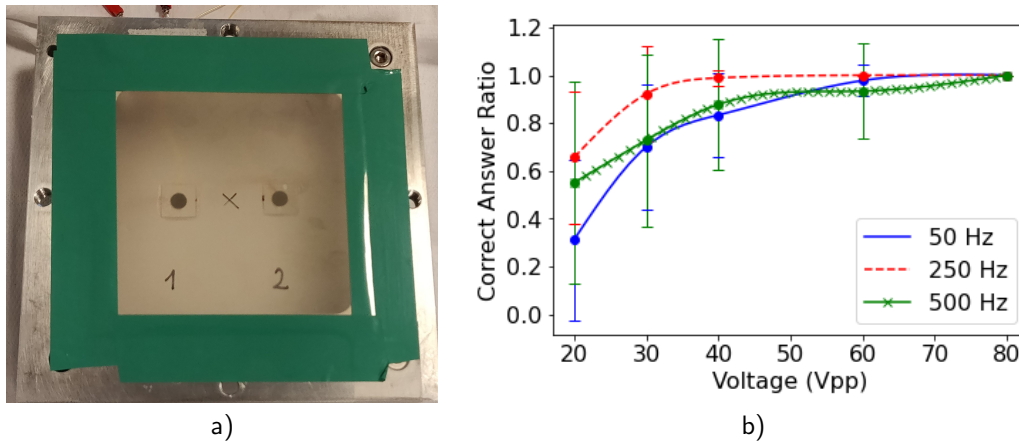
Figure 2.26: a) Surface used for the psychophysical test; b) Mean correct answer ratio.

Figure 2.27: Confusion matrix at 40 Vpp.

can be localized around one resonator and is well detectable by the users. Different signals allow to modulate the haptic feeling.

2.6 Conclusion

This chapter introduces a haptic resonator integrated in a flexible matrix. Firstly the design, based on analytical and numerical developments, of two different haptic resonators is explained, each consisting of three components: a square or rectangular glass plate vibrating at an ultrasonic frequency, a piezoelectric PZT actuator, and a polymer film. Electromechanical characterizations were carried out to validate the design. The square haptic resonator was chosen for its performance and characteristics. Different polymer films were compared, and the 100 µm-thick PEEK film and the 75 µm-thick KAPTON film were selected. Despite non-optimized manufacturing with manual bonding and rather coarse soldering, displacements of around 1 µm were obtained for 20 Vpp. Improved performance can be expected with

a more sophisticated manufacturing process. Additionally, a tribological study confirmed the reduction in friction on the haptic resonators. Lastly, a psychophysical study confirmed the detectability of the resonators. For an actuation signal of 30 Vpp at resonance and modulated at 250 Hz, the resonators are detected by the participants in 92 % of cases.

This chapter also discusses the creation of a flexural wave on the polymer due to the resonator vibration. The following chapter will analyze this wave and use it to develop a haptic interface with 9 resonators arranged in a 3 x 3 matrix, allowing for localized or continuous sensations through friction modulation.

Chapter 3

Design of a flexible haptic surface of 9 resonators

Contents

3.1 Introduction

The aim of this chapter is to design a surface with nine haptic resonators based on the unitary element that was developed and validated in the previous chapter. As demonstrated, the haptic resonator generates a flexural wave on the surface of the polymer film. This wave is analyzed in this chapter to achieve localization of friction reduction or continuity of the haptic feedback. The chapter starts by examining the wave produced by the haptic resonator and the displacement field on the polymer surface in 3.2. Then, it presents the interaction between two resonators coupled to the same polymer

film. A clamped-free beam model is chosen to model the polymer film between two resonators and the distance between two resonators is optimized to maximize the displacement in 3.3. Furthermore, an 3 x 3 array of haptic resonators is presented with a model to subdivide the surface in 3.4. We highlight the potential to obtain local and large tactile shapes. The chapter concludes by emphasizing the flexibility of the 9-resonator haptic surface in 3.5.

3.2 Displacements generated by one haptic resonator

In this section, we analyze the wave and the displacements generated by a haptic resonator.

3.2.1 On the haptic resonator

When the resonator is active due to the mode of vibration selected for the square plate in chapter 2, the displacement on the resonator can be expressed like this :

$$u_z(x, y, t) \propto U_{z_0} e^{j(\omega t + \phi)} * (\cos \frac{\pi}{2} \frac{x}{R_{mode}} + \cos \frac{\pi}{2} \frac{y}{R_{mode}}) \tag{3.1}$$

with $U_{z_0} e^{j(\omega t + \phi)}$ the vibration amplitude at the resonator center depending of the resonator excitation, R_{mode} the radius of the antinode of vibration, i.e. 2.5 mm for the 10 mm resonator.

3.2.2 On the polymer film

The focus is now on understanding the wave generated on the polymer surface by the vibration of the haptic resonator.

To obtain the characteristics of the wave, we consider a Kirchoff model to represent it in the polymer. The polymer film is considered isotropic, homogeneous and infinite. The plate is initially flat. Deformation is considered to be pure bending (Kirchoff-Love hypothesis) and vertical deformations are small and linear. The equation for a thin plate is then introduced:

$$D_p \nabla^4 u_z(x, y, t) + \rho_p h_p \frac{\partial^2 u_z(x, y, t)}{\partial t^2} = 0 \tag{3.2}$$

With $u_z(x, y, t)$ the transverse displacement, $D_p = \frac{E_p h_p^3}{12(1-\nu_p^2)}$ the flexural rigidity for the polymer film

with h_p the thickness, E_p the Young's modulus, ν_p the Poisson's ratio and ρ_p the density.

Thus the displacement, solution of the equation 3.2, on the polymer film is the sum of propagating and evanescent terms :

$$u_z(r,t) = A_1 e^{-jk_w r} + A_2 e^{jk_w r} + A_3 e^{-k_w r} + A_4 e^{k_w r} \tag{3.3}$$

with r depending of the propagation direction, A_1, A_2, A_3 and A_4 proportional to $e^{j(\omega t + \phi_A)}$ with ω the pulsation, ϕ_A the phase and depending of the boundary condition, and k_w the wave number on the polymer.

During simulations and measurements carried out to select the polymer, the wave was observed in the polymer film (Fig. 3.1).
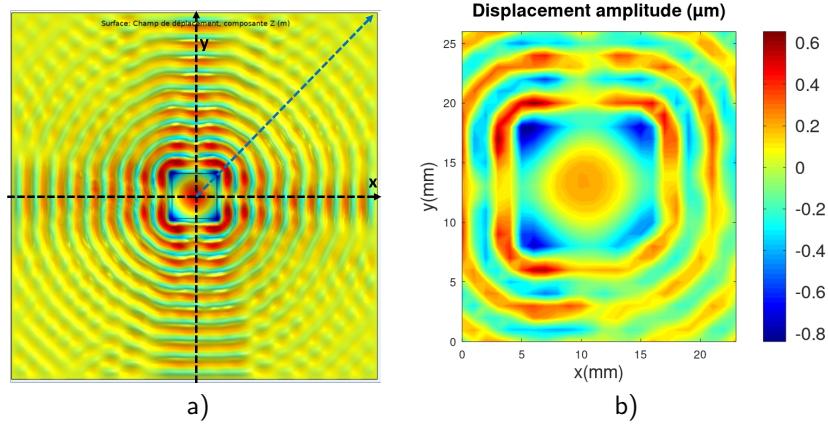
Figure 3.1: a) FEM and b) Mapping of one resonator at the resonance.

The polymer film exhibits a wave with four primary directions ($+x$, $-x$, $+y$, and $-y$) and four secondary directions corresponding to the corners of the plate. This is because the haptic resonator has a square shape, resulting in four resonant sides of the plate that generate planar waves perpendicular to the sides. In contrast, four spherical waves are created in the corners of the vibrating plate.

The pulsation on the polymer film as a function of the wave vector can be defined as presented before with the equation 2.22 :

$$\omega = \sqrt{\frac{E_p h_p^2}{12\rho_p(1 - \nu_p^2)}}(k_w)^2 \tag{3.4}$$

Here, there are no particular constraints on wavelength, as the polymer film is consider infinite. So the

wavelength in the polymer λ_p can be determined at the resonance :

$$\lambda_p = \frac{2\pi}{k_w} \tag{3.5}$$

Because the pulsation ω is fixed by the frequency of the haptic resonator, the wavelength is a direct result of the selected polymer (material properties), its thickness and the resonator frequency :

$$\lambda_p = 2\pi \left(\frac{E_p}{12\rho_p(1-\nu_p^2)} \right)^{1/4} \left(\frac{h_p}{\omega} \right)^{1/2} \tag{3.6}$$

Fig. 3.2 shows the wavelength variation as a function of the haptic resonator frequency for the two polymer films used.
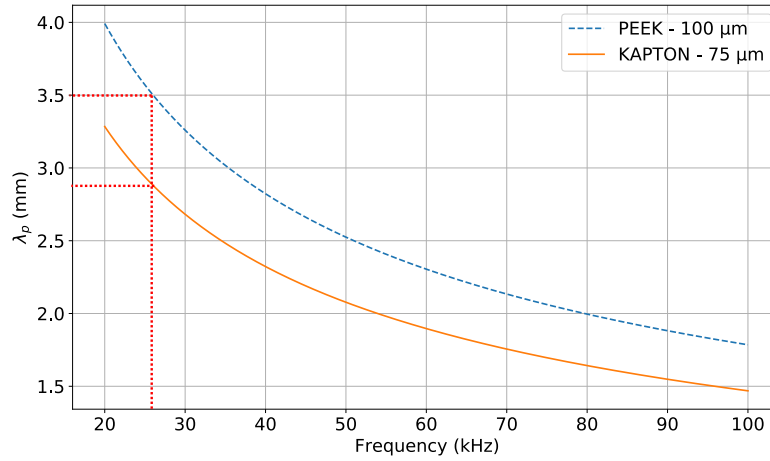
Figure 3.2: λ_p on the polymer films.

In the situation presented in the chapter 2, the resonance frequency is 26 kHz for the two situations, which corresponds to a wavelength of 3.5 mm for PEEK-100 μm and 2.9 mm for KAPTON-75 μm.

3.3   Development of a two-resonator haptic system

As seen above, a resonator driven at its resonant frequency creates a flexural wave on the polymer surface. Here, therefore, two resonators are combined and interference phenomena occur. In this situation, the polymer surface is no longer considered infinite, since it is limited between the two

resonators A and B by a distance L_p. The aim is to optimize this distance without changing the wavelength λ_p, which is already small at 3.5 mm or 2.9 mm. In fact, the half-wavelength $\lambda_p/2$ characteristic of friction modulation is 1.75 mm or 1.45 mm, which is very close to the spatial resolution under the finger, about 1 mm, and thus could be problematic for detectability by friction modulation.

In this section, we optimize the distance between two resonators to maximize the transverse displacements on the polymer surface with λ_p fixed.

As we have seen, the wave emitted by a resonator has four main directions of propagation. We place another resonator in a main propagation direction $+x$ (Fig. 3.3).
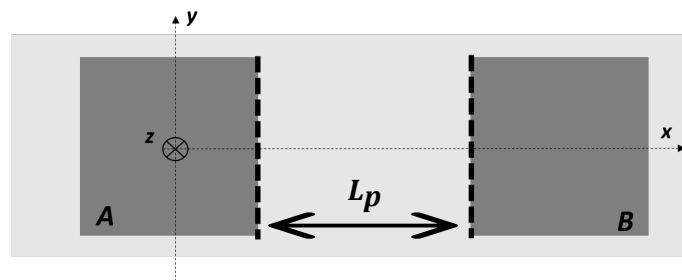
Figure 3.3: Schematic diagram of two haptic resonators.

3.3.1 One active and one resonator

In the first case, only one resonator is being actuated while the other remains off.

Observations

On the COMSOL model of the haptic resonator with the polymer film of chapter 2 we add the second resonator, separated by a distance L_p, which remains passive (non-activated). We then plot the displacement field at the resonance for the two situations : a) vibration mode without and b) with adjacent passive resonators (Fig. 3.4).

As we can see, the wave emitted by the active resonator is reflected by the passive resonator (Fig. 3.4.b). In this way, a standing wave is created between the two resonators, enabling the wave to be localized.

We now vary the distance L_p between the two resonators in the COMSOL model. The transverse displacement in the (x, z) plane is then plotted in Fig. 3.5 for a 100 µm-PEEK film structure for a

a)   b)
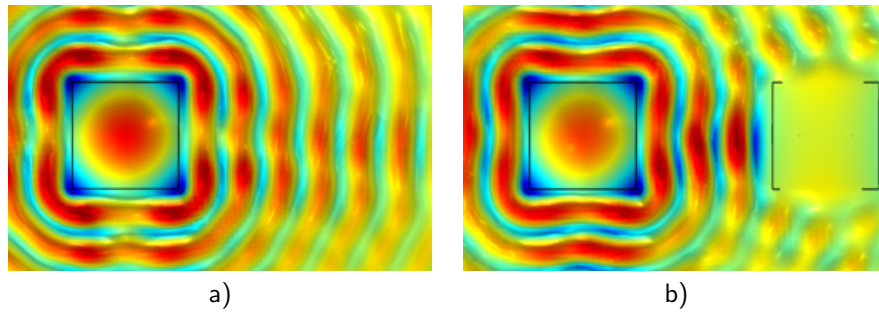
Figure 3.4: Vibration mode without (a) and with (b) adjacent passive resonators.

frequency of 26 kHz.
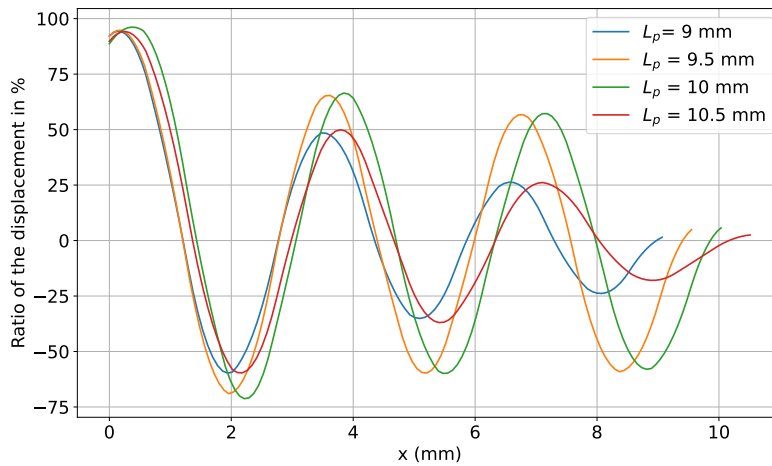
Figure 3.5: Displacement amplitude on the polymer film between one active and one passive resonator for various L_p.

The displacement amplitude between the two resonators varies with distance, and a specific distance between 9.5 and 10 mm enables the flexural displacement between the two resonators to be maximized. Additionally, the displacement is zero or close to zero at the passive resonator, while it is maximum at or just after. The behavior of the polymer film between the two resonators is similar to that of a beam that is free on one side (for x = 0) and clamped on the other side (for x = L_p).

To confirm this, a two-resonator assembly is made and laser vibrometer measurements is carried out. We can find on Fig. 3.6.c) this assembly for a distance L_p of 24 mm between the two resonators on a 100 µm-PEEK film. The surface displacement is plotted in Fig. 3.6 in the (x, y) and (y, z) planes if only one resonator is active (the left one).
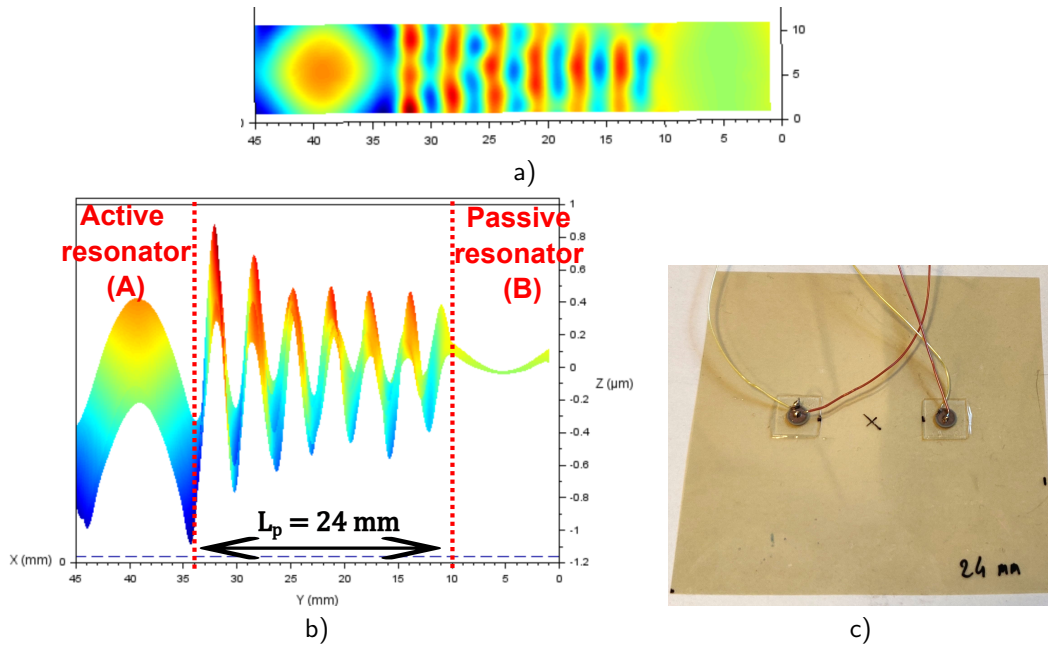
Figure 3.6: Measurement of the displacement field for $L_p = 24$ mm : a) Top view, b) Transverse view and c) Assembly used.

Adding a second resonator at a distance of L_p from the first creates a standing wave with parallel wavefront between the two resonators. The wave emitted by the active resonator is reflected by the passive resonator due to the change of medium between the polymer and the resonator. This creates a mirror or acoustic barrier at the boundary of the passive resonator, as shown in Fig. 3.7. Thus, due to the significant difference in stiffness between the two media, the displacement at the passive resonator is negligible and can be considered null. Additionally, the displacement is maximum at the boundary of the active resonator.
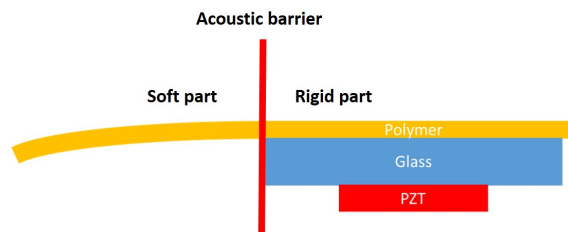
Figure 3.7: Drawing of the acoustic barrier.

As observed by both the FEM simulation and measurements, the polymer film between the active

and passive resonators can be approximated as a vibrating beam with a fixed edge for the passive resonator and a free edge for the active resonator. The displacement on the passive resonator is negligible and can be considered as zero. To simplify, we also assume that the displacement is maximal at the boundary of the active resonator.

Model as a clamped-free beam

We now develop the model of a clamped-free beam to choose a distance L_p that allows to optimize the displacement between an active and a passive resonator. The wavelength λ_p is fixed by the resonator frequency. We do not consider the damping in this model.

The solution 3.3 of equation 3.2 can be rewritten as:

$$u_z(x) = a\ sin(k_w x) + b\ cos(k_w x) + c\ sinh(k_w x) + d\ cosh(k_w x) \tag{3.7}$$

With conditions a, b, c and d determined according to the boundary conditions. Here, because we consider the passive resonators B fixed at L_p, we have: $u_z(L_p) = 0$ and $u_z'(L_p) = 0$. On the other hand, we consider the free end, i.e. zero moment and zero shear force at A for $x = 0$ with $u_z''(0) = 0$ and $u_z'''(0) = 0$.

Thus we obtain this linear system :

$$\begin{pmatrix} sin(k_w L_p) & cos(k_w L_p) & sinh(k_w L_p) & cosh(k_w L_p) \\ cos(k_w L_p) & -sin(k_w L_p) & cosh(k_w L_p) & sinh(k_w L_p) \\ 0 & -1 & 0 & 1 \\ -1 & 0 & 1 & 0 \end{pmatrix} \begin{pmatrix} a \\ b \\ c \\ d \end{pmatrix} = \begin{pmatrix} 0 \\ 0 \\ 0 \\ 0 \end{pmatrix} \tag{3.8}$$

Non-zero solutions of this linear system are those canceling the determinant. Thus k_w have to verify this equation :

$$1 + cos(k_w L_p)cosh(k_w L_p) = 0 \tag{3.9}$$

Solving this equation gives us the value of $k_w L_p$. The first value is for the fundamental mode with $k_w L_p = 1.875$. The second value is for the first harmonic with $k_w L_p = 4.694$, and the third for

$k_w L_p = 7.855$. For the highest harmonic, the value of $k_w L_p$ is :

$$k_w L_p = (2n+1)\frac{\pi}{2} \tag{3.10}$$

where n is the number of nodes along the polymer film between two resonators.

Fig. 3.8 shows the first mode of an undamped free-clamped beam with a distance normalized to 1.
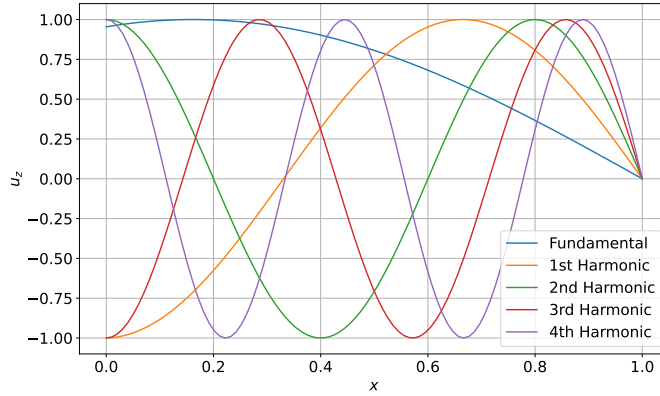
Figure 3.8: First mode of vibration of an undamped free-clamped beam.

In our situation, the wavelength λ_p is fixed by the frequency of the resonator. Since $\lambda_p = 2\pi/k_w$, the value of L_p that allows to maximize the displacement between two resonators is :

$$L_p = \frac{\lambda_p}{2}(n + \frac{1}{2}) \tag{3.11}$$

Thus, the distances L_p which allow to maximize the displacement between the resonators for the PEEK film and the KAPTON film for the frequency of 26 kHz, and thus for $\lambda_p = 3.5$ mm for PEEK-100 μm and $\lambda_p = 2.9$ mm for KAPTON-75 μm are presented in the Table 3.1.

For the PEEK film, for $n = 5$, the value of L_p corresponds to the value observed in Fig. 3.5. In fact, in the FEM simulation, the maximum of the amplitude was for a distance L_p between 9.5 and 10 mm, which is consistent with 9.6 mm for the model of a freely clamped beam. In addition, for the realization with a distance L_p of 24 mm in Fig. 3.6, we observe 13 nodes between the two resonators. This is consistent with the model's optimal length of 23.7 mm for 13 nodes. We are therefore close to the optimal coupling distance in this situation.

Table 3.1: Optimum distance L_p between two resonators for PEEK 100 µm and KAPTON 75 µm at 26 kHz.

Number of vibration nodes	L_p - PEEK-100µm (mm)	L_p - KAPTON-75µm (mm)
3	6.1	5.1
4	7.9	6.5
5	9.6	8.0
6	11.4	9.4
7	13.1	10.9
8	14.9	12.3
9	16.6	13.8

3.3.2 Two active resonators

In this part we now consider the situation when the two resonators are activated with the same frequency and the same amplitude. We assume that the condition on the distance L_p of the equation 3.11 is fulfilled.

Superimposition of the displacements

As expressed before, the general expression of the displacement $u_{z_A}(x)$ without considering the boundary conditions is :

$$u_{z_A}(x) = a\ sin(k_w x) + b\ cos(k_w x) + c\ sinh(k_w x) + d\ cosh(k_w x) \tag{3.12}$$

To simplify, we assume that the amplitude does not vary along the polymer film because we validate the optimum distance of the equation 3.11. Thus the effects of $cosh$ and $sinh$ are ignored in this simplified model. As a result, we have:

$$u_{z_A}(x) = a\ sin(k_w x) + b\ cos(k_w x) \tag{3.13}$$

Here the boundary conditions imposed that, $u_{z_A}(L_p) = 0$, so $a\ sin(k_w L_p) + b\ cos(k_w L_p) = 0$. In addition, $k_w L_p$ is defined such as $cos(k_w L_p) = 0$ as it is optimized in the clamped-free beam model. Hence $a = 0$.

Thus the displacement induced by the resonator A with W_A the amplitude at the boundary is

considered as :

$$u_{z_A}(x) = W_A \ cos(k_w x) \tag{3.14}$$

The same is done for the displacement induced by the resonator B and we obtain :

$$u_{z_B}(x) = W_B \ cos\left(k_w(L_p - x)\right) \tag{3.15}$$

According to the principle of superposition, the displacement obtained with resonator A is superimposed on the displacement induced by resonator B. Moreover we assume the two resonators are identical so $W_B = W_A = W$. So the total displacement is :

$$u_{z_+}(x) = W \ cos(k_w x) + W \ cos\left(k_w(L_p - x)\right) \tag{3.16}$$

We develop $cos(k_w x) + cos(k_w(L_p - x))$ with $cos(p) + cos(q) = 2cos(\frac{p+q}{2})cos(\frac{p-q}{2})$. Thus we have:

$$u_{z_+}(x) = 2W cos\left(\frac{k_w L_p}{2}\right) cos\left(k_w(x - \frac{L_p}{2})\right) \tag{3.17}$$

Because we consider that the condition of the equation 3.10 is validated, we can also expressed the displacement as :

$$u_{z_+}(x) = 2W cos\left((2n+1)\frac{\pi}{4}\right) cos\left(k_w x - (2n+1)\frac{\pi}{4}\right) \tag{3.18}$$

$2W|cos((2n+1)\frac{\pi}{4})| = \sqrt{2}W$, so the absolute displacement amplitude at the polymer film is a factor of $\sqrt{2}$ greater than that at the resonator boundary.

And if the two resonators are out of phase with $W_B = -W_A$ we have :

$$u_{z_-}(x) = W cos(k_w x) - W cos(k_w(L_p - x)) \tag{3.19}$$

By developing $cos(k_w x) - cos(k_w(L_p - x))$ with $cos(p) - cos(q) = 2sin(\frac{p+q}{2})sin(\frac{q-p}{2})$ we obtain :

$$u_{z_-}(x) = 2W sin\left(\frac{k_w L_p}{2}\right) sin\left(k_w(x - \frac{L_p}{2})\right) \tag{3.20}$$

which can also be expressed as :

$$u_{z_-}(x) = 2W \cos\left((2n-1)\frac{\pi}{4}\right) \cos\left(k_w x - (2n+1)\frac{\pi}{4} - \frac{\pi}{2}\right) \tag{3.21}$$

The phase shift between the two situations is $\pi/2$, depending on whether the two resonators are in phase $W_B = W_A = W$ or in phase opposition $W_B = -W_A = -W$. The displacement amplitude is identical $\sqrt{2}W$, as is the wavelength λ_p, since the two resonators are considered identical.

On Fig. 3.9 we plot the displacement amplitude for $L_p = 11.4$ mm and $L_p = 13.1$ mm with a PEEK film using this model. W is considered unitary.

a)   b)
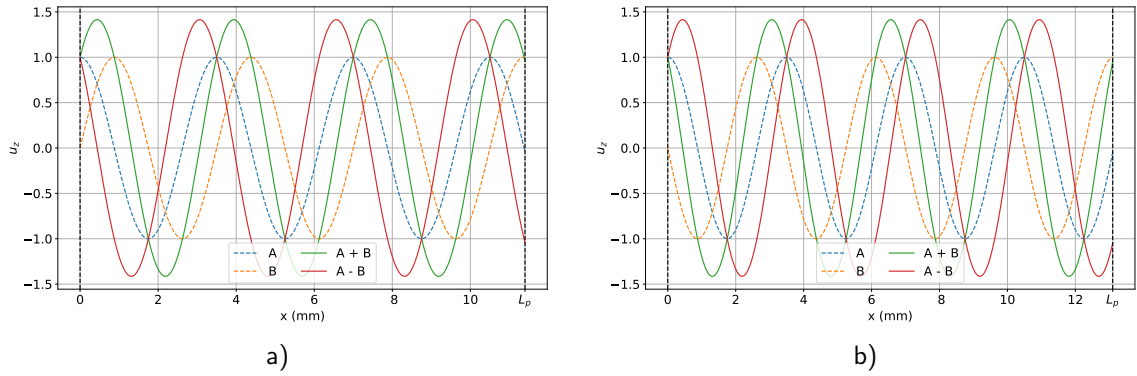
Figure 3.9: Transversal displacement for a) $L_p = 11.4$ mm or b) $L_p = 13.1$ mm with a PEEK film obtained with the model.

The displacement induced by resonator A, u_{z_A}, on the polymer film is in blue, and the displacement induced by resonator B, u_{z_B}, is in orange for $L_p = 11.4$ mm and for $L_p = 13.1$ mm. Thus, for each case where a resonator is active, we find the correct number of nodes as expected from our model in Table. 3.1. So there are 6 nodes along the polymer film for $L_p = 11.4$ mm and 7 nodes for $L_p = 13.1$ mm.

In Fig. 3.9.a), when $L_p = 11.4$ mm, A and B are in phase, in green, i.e. $W_B = W_A = W$, there are still 6 nodes, while when the resonators are in phase opposition, in red, there is an additional node. This is due to the $\pi/2$ phase shift observed between them in the expressions $u_{z_+}(x)$ of 3.18 and $u_{z_-}(x)$ of 3.21. However, this phase shift does not change the deformation amplitude at the polymer film, which is $\sqrt{2}W$ and the wavelength λ_p at the polymer film. For $L_p = 13.1$ mm, we observe that the number of nodes remains the same when the two resonators are in phase opposition, while it increases

by 1 to reach 8 nodes when they are in phase due to the phase shift of $\pi/2$.

Thus, if the number of nodes in the table 3.1 is even, the resonators must be in phase to have an unchanged number of nodes, while if the number of nodes is odd, the resonators must be in phase opposition.

The system of two active resonators is then modeled in COMSOL for cases where the distance L_p validates the equation 3.11 with a PEEK film assembly. We plot the case for $L_p = 11.4$ mm with in phase, Fig. 3.10.a), and out of phase resonators, Fig. 3.10.b).
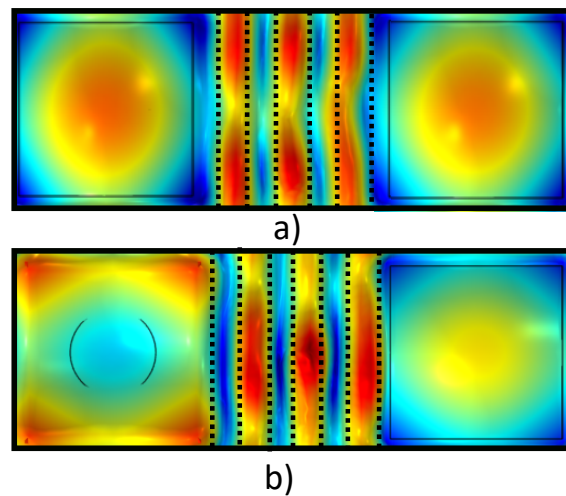
Figure 3.10: Transversal displacement for $L_p = 11.4$ mm : a) Resonators in phase with 6 nodes of vibrations, b) Resonators in out of phase with 7 nodes of vibrations.

As estimated with the simplified analytical model, we find 6 modes of vibration when the resonators are in phase and 7 nodes when they are out of phase. The phase shift between the two displacements is $\pi/2$. As a result, the wavelength is unchanged, i.e. $\lambda_p = 3.5$ mm at this frequency. The displacement amplitude is also consistent, with the maximum displacements on the polymer $\sqrt{2}$ times larger than the displacement at the resonator boundaries.

In Fig. 3.11.a) we present the case for in-phase resonators with $L_p = 14.9$ mm and in Fig. 3.11.b) the case for out-of-phase resonators with $L_p = 13.1$ mm. The simplified model is also validated for these two case.
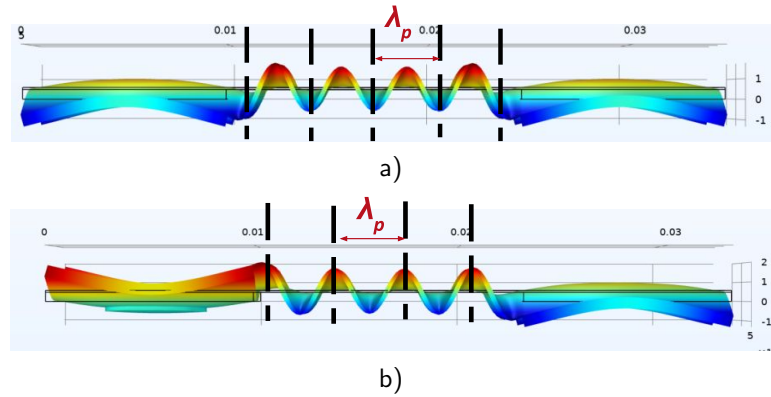
Figure 3.11: Cross-view of two haptic resonators on COMSOL: a) $L_p = 14.9$ mm , b) $L_p = 13.1$ mm.

Measurements

On an assembly of two resonators separated by 13.1 mm on a PEEK film, we measure the wavelength λ_p and the displacement on the surface for four different situations (Fig. 3.12). Situations a) and b) are when only one resonator is activated. Situation c) is when the resonators are in phase and the situation d) when they are in phase opposition.
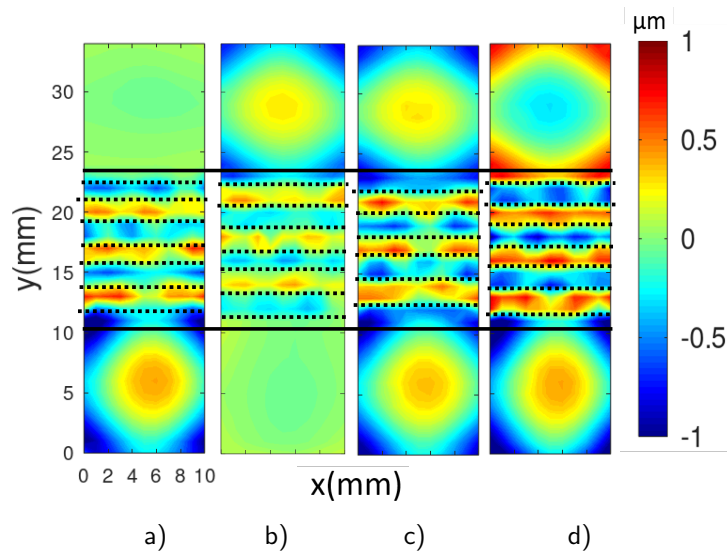
Figure 3.12: Amplitude displacement for 4 different situations.

A voltage of 20 Vpp is applied at the resonator frequency of 26 kHz. As expected, there are 7 vibration nodes for the cases where only one resonator is active, Fig. 3.12.a) and .b), and the case

where two resonators are in phase opposition, Fig. 3.12.d). However, in the case where only one resonator is active, the last vibration antinode before the passive resonator is hardly visible, as shown in Fig. 3.12.a) and .b) and in the transverse view in Fig. 3.13. This is due to the uncertainties of the components (materials, bonding and soldering) and the manufacturing process. The distance between the two resonators is also uncertain because it is made by hand, without a technique that is accurate to the millimeter.
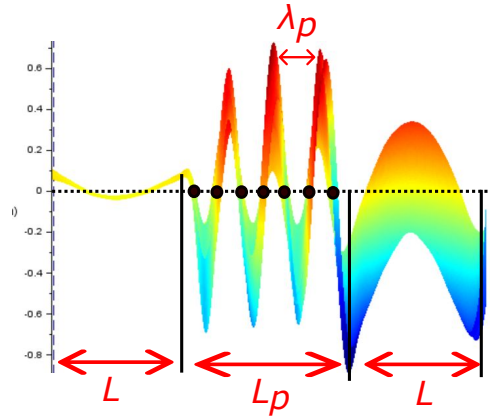
Figure 3.13: Transverse view for one active and one passive resonator for $L_p = 13.1$mm.

As a result, there are only 6 nodes on the polymer film instead of the 8 expected by the simplified model when the resonators are in phase in Fig. 3.12.c). However, we note that the phase shift between the $u_{z_+}(x)$ displacement for in phase resonators and the $u_{z_-}(x)$ displacement for out of phase resonators is indeed $\pi/2$.

The displacements for the first two plots are zero when the resonators are passive. The maximum displacement at the active resonator boundary is 0.8 µm (Fig. 3.13). When only one resonator is active (Fig. 3.12.a), .b) and Fig. 3.13), the maximum displacement on the polymer is 0.6 µm. Conversely, the displacement on the polymer film is larger when two resonators are active in Fig. 3.12.c) and.d). We still have 0.8 µm at the resonator boundary and a maximum of 1.2 µm on the polymer, which is an increase of 50 %, a little more than $\sqrt{2}$.

Despite the fact that the fabrication process is not really optimized since everything is done by hand, we obtain displacements in the order of 1 µm for a relatively low voltage (20 Vpp), we see that we can localize or create large areas of vibration as desired, thanks to the continuity on the polymer film between the resonators.

So, now that we have confidence in the model presented earlier, we will extend our surface to include nine resonators arranged in a 3 x 3 matrix.

3.4 Design of a 9-resonator surface

The aim is to develop a flexible 9-resonator interface. Thus, in this section, the focus is on a matrix of 3 x 3 haptic resonators.

3.4.1 Modeling

Each resonator, when activated, creates a flexural wave at the surface, as explained above. Our goal is to design a periodic structure with 3 x 3 resonators connected to a polymer film. Based on the previous section, the haptic resonators are spaced L_p apart to form a 3 x 3 matrix. As a result, the displacement amplitude between each resonator in x and y directions is maximized.

Fig. 3.14 shows a drawing of the situation with 9 haptic resonators coupled on a polymer plate.
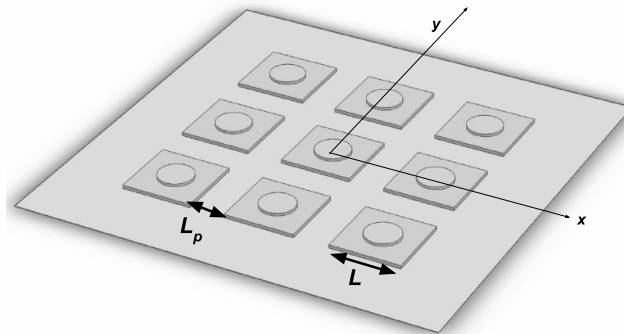
Figure 3.14: Interface of 9 resonators.

This gives us a structure similar to phononic crystals in metamaterials, but with an opposite goal to ours. In fact, periodic structures are commonly used in acoustic metamaterials to generate a bandgap and to capture vibrations generated by a piezoelectric actuator on a rigid surface, for example, through passive resonators. These resonators are defined as invariant in their state. As a result, passive resonators direct vibrations to a specific frequency band that can be calculated and optimized [108, 109, 110, 71].

In our situation the resonators can be active or passive as seen before. Thus, to express the

displacement on the surface, we can divide it into several vibration zones, as shown for 4 resonators in Fig. 3.15.
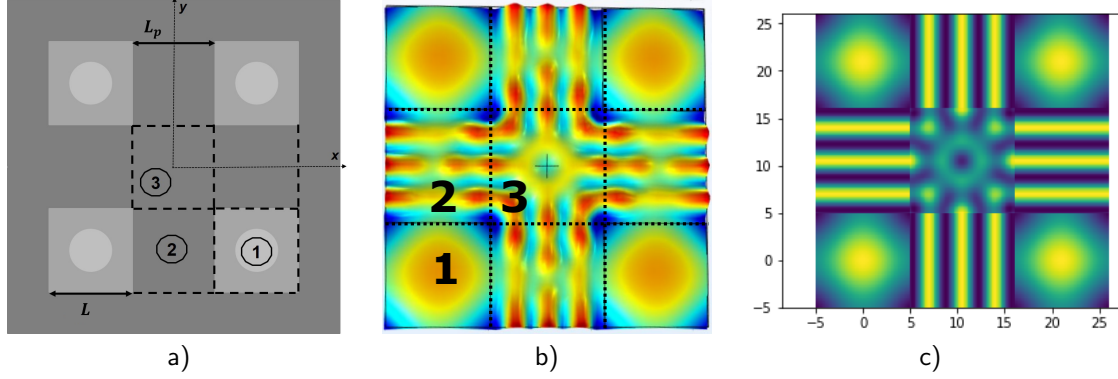
Figure 3.15: a) Model of 4 resonators, b) Displacements fields for $L_p = 11.4$ mm obtained with COMSOL and c) with the simplified model.

As can be seen in Fig. 3.15, three different areas of vibration can be determined for an array of 2 x 2 resonators, and by extension, for an array of 3 x 3 resonators:

1. The first zone is located at the top of the haptic resonator. Here we find the resonance mode selected in chapter 1 and simplify the displacement as presented in 3.2.1 to :

$$u_z(x, y, t) \propto U_{z_i} e^{j(\omega t + \phi_i)} * (\cos \frac{\pi}{2} \frac{x}{R_{mode}} + \cos \frac{\pi}{2} \frac{y}{R_{mode}}) \tag{3.22}$$

where U_{z_i} is the vibration amplitude at the i-th resonator center, ϕ_i is the phase, R_{mode} is the radius of the vibration antinode, i.e. 2.5 mm for the 10 mm resonator.

2. The second zone concerns the spaces between two resonators along either the x or the y axis. Here we find the wave sum presented in the previous section 3.3 for two resonators A and B. Thus, since we consider the condition on the distance L_p as respected, the amplitude of the displacement depends on whether only one (u_{z_A} or u_{z_B}) or both resonators are activated u_{z_+} as in the equation 3.18 or u_{z_-} in 3.21.

3. The last zone corresponds to the intersection of four resonators. Here we simplify the displacement as a superposition of four waves, for cylindrical coordinates. We neglect the various reflections

69

and transmissions of the waves emitted by the other resonators. The result is :

$$u_z(x,y,t) \propto \sum_{n=1}^{4} Z_i * e^{j(\omega t - k_w r)}, r = \sqrt{(x-x_l)^2 + (y-y_l)^2}$$

where Z_i are the vibration amplitudes at the boundary conditions either in the resonator angle between zones 1, 2 and 3 and x_l and y_l are the zone boundary coordinates.

This provides an overview of the shape of the displacement on the surface as presented for example in Fig. 3.15.c) for $L_p = 11.4$ mm. However, accurately calculating the displacement at any point on the surface using analytical methods is complex. Therefore, we use COMSOL to model the surface.

3.4.2 Tactile shape

To determine surface displacement, simulations were run in COMSOL under different scenarios. Multiple non-adjacent active resonators were used to create localized tactile shapes, while adjacent active resonators were used to obtain large tactile shapes on the haptic surface. The surface was assumed to be simply supported at its edges.

Localized tactile shape

At the resonance by choosing the activated resonators we create area of vibration and thus area of tactile feedback using friction reduction.

For example, Fig. 3.16 depicts the simulation results of two different situations for a PEEK film with $L_p = 11.4$ mm. For the first one two non adjacent resonators are activated at the same frequency since they are identical and for the second one a line of three active in-phase resonators and a single resonator are activated. A signal with a voltage of 40 V peak to peak at the resonance is used.

As observed the tactile shapes are well localized as expected due to the large reflection of the wave on passive resonators. The model, calibrated to be in agreement with our first experimental measurements, shows a maximum amplitude of displacement of 2 µm for 40 Vpp which is enough to produce haptic feeling. Conversely, the vibrations on the 3-resonator line are continuous. Thus we find as explained before different zones on the surface: on an active resonator, a stationary wave between two resonators and spherical wave between four resonators. The areas of vibrations are also clearly distinct. Only
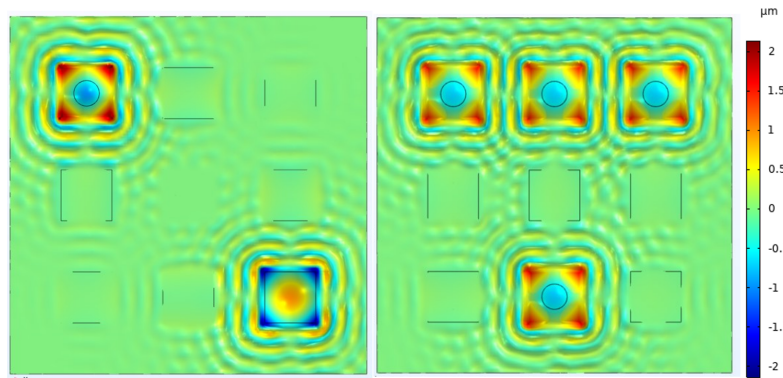
Figure 3.16: Displacement field for two points and for a line and a point.

the targeted areas vibrate and generate haptic feedback. This suggests multitouch possibilities, with a specific feel for each activated area.

Large tactile shape

Then Fig. 3.17 shows two other situations. The first one is the drawing of a "L" shape on the surface and the second one is a "+" shape for a PEEK film with $L_p = 11.4$ mm.
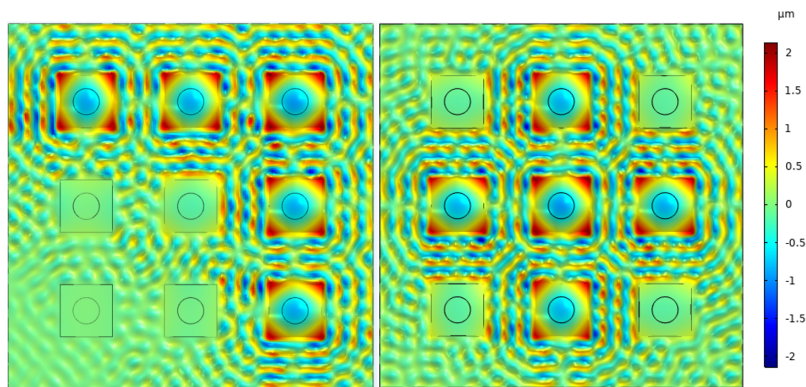
Figure 3.17: Displacement field for a "L" shape and a "+" shape.

The "L" shape is interesting because we clearly see the activated zone which can be similar as a path with two bands. In some way the wave is guided in band as in phononic crystals. Active resonators guide the waves in contrast to phononic crystal where passive resonators guide the wave. The "+" shape may be more challenging to discern. The wave propagation and reflections between active and passive resonators are likely to result in a relatively large active area. A study on shape recognition will

be conducted later to evaluate the detectability of this kind of shape.

Thus, the designed interface will enable localized or large-area sensing through the combination of haptic resonators. The surface displacements and resonance frequency are appropriate for ultrasonic lubrication.

3.4.3 Measurements

To confirm our modeling some interfaces are fabricated using the same process as before. 9 haptic resonators are made manually and then bonded to a KAPTON or a PEEK polymer film as presented in Fig. 3.18.
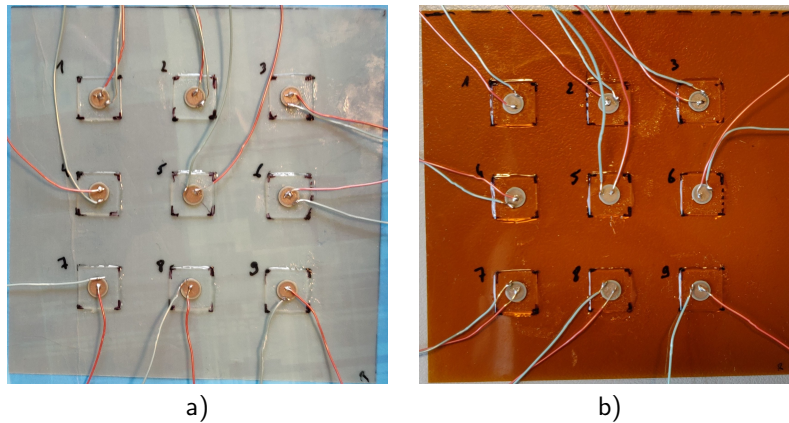
Figure 3.18: a) PEEK 100 µm with 9 resonators; b) KAPTON 75 µm with 9 resonators.

Vibration measurements are performed to validate the possibility of creating a tactile shape. Fig. 3.19 shows three different cases for a surface realized with a 100 µm thick PEEK film and for a space of 13.1 mm between each haptic resonator. The actuation signal is at 20 Vpp and the frequency is the same for each resonator. The resonators are in phase opposition for 13.1 mm with n = 7 as shown in the table 3.1.

The first plot in Fig. 3.19.a) allows to confirm the propagation of the wave when only one haptic resonator is activated. The passive resonators guide the wave on the polymer film generated by the active one. In addition, we can see that in the main directions of propagation, in this case $-x$ and $+y$, the zone directly behind a passive resonator also undergoes a slight displacement. This shows that the passive resonator, even when not actuated, transmits a part of the wave and is not a perfect acoustic

a)   b)   c)
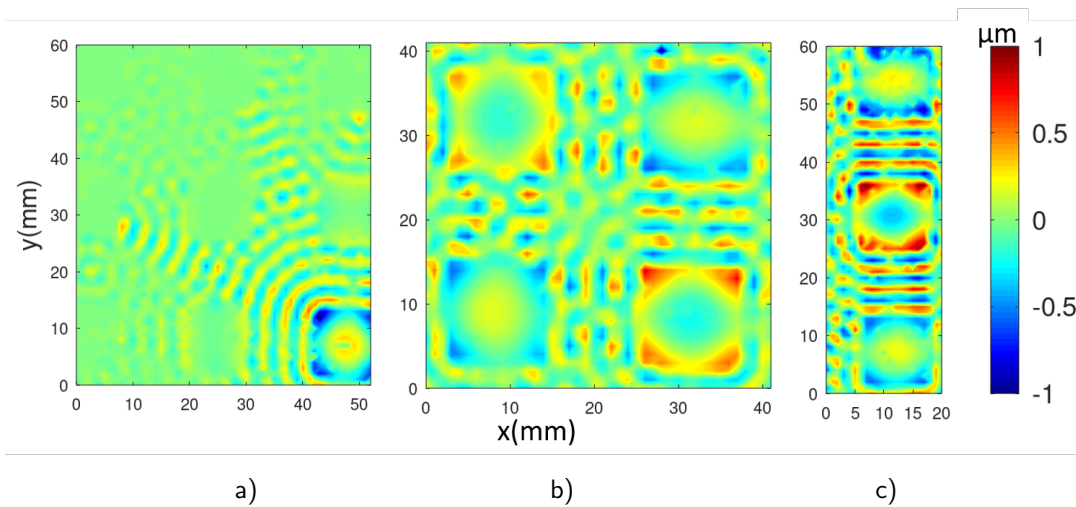
Figure 3.19: Displacement measurements for different configurations.

reflector, as considered in our model of the clamped free beam in the section 3.3.1. We will determine in use cases whether this affects the localization of the friction modulation feedback.

The second plot in Fig. 3.19.b) highlights the interaction between four haptic resonators. In this case, we can see that the area between the four resonators, zone 3 in Fig. 3.15, is a zone where the displacements are almost completely canceled out. So it seems that there is a destructive interference between the 4 components of the displacements and therefore there is no continuity of the vibrations in this area. We will see later if the user perceives this discontinuity. Furthermore, the frequency chosen to drive all the resonators does not seem to be optimal. The resonator mode is not very good either. This is due to the fact that the manufacturing is done manually. On Fig. 3.20 we can see the impedance of each resonator of this surface. The graph is very noisy. The module impedance varies by about ± 500 Ohms between each resonator, and the resonance occurs between 26 kHz and 28 kHz. This manufacturing uncertainty is due to the manual application of glue or soldering wire.

On the last plot, Fig.3.19.c), the resonance is much better. The parallel front wave between the resonators is well defined. It also confirms the wavelength of 3.5 mm for the 100 μm thick PEEK film at 26 kHz. Moreover, the displacement amplitudes are sufficient to obtain a haptic sensation with friction reduction, even if these realizations are not optimal because they are made manually.

73
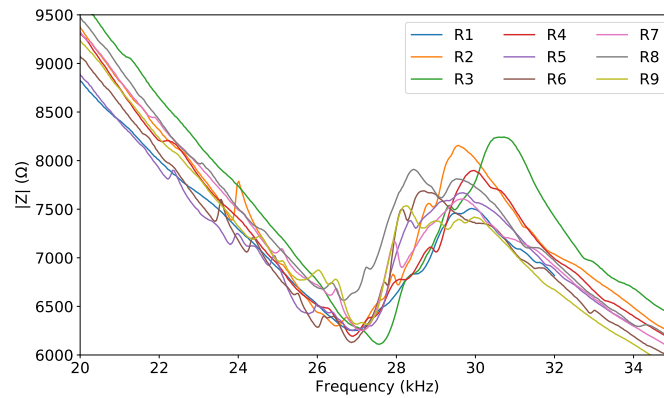
Figure 3.20: Impedance obtained for the 9 resonators of the surface with PEEK 100 µm and a space of 13 mm.

3.5 Flexibility of the haptic surface

In this part the flexibility of the interface is determined in a 1D model and compared to the flexibility of a homogeneous beam of polymer PEEK. Then the impact of the deformation of the surface on the mechanical response of the haptic resonators is analyzed.

The polymer film provides flexibility and conformability to the haptic interface (Fig. 3.21). It acts as a hinge, allowing the surface to bend. The flexibility is achieved by the thinness of the polymer film (75 µm for KAPTON or 100 µm for PEEK), the length of the gap between two resonators L_p (the length of the hinge) and the mechanical properties of the polymer film with a low Young's modulus.

The polymer between two resonators also guarantees conformability, or the capability to contour to any surface. The greater the distance between the resonators, the more conformable the surface. In this way, a large distance between two resonators allows surfaces with a small radius of curvature to be accommodated.
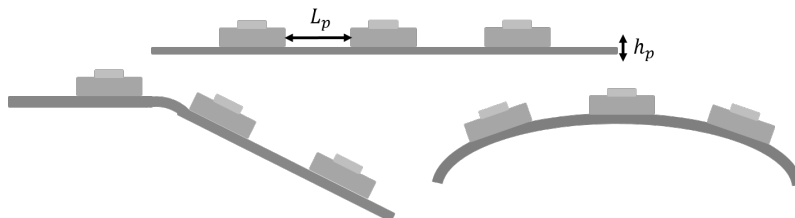
Figure 3.21: Cross-section drawing of the surface for flexibility and conformability.

3.5.1 Deformation of the haptic surface

To analyze the flexibility of the solution, we aim to determine the surface deformation under a unit load.

To achieve this, we consider a principal direction $(+x)$ and model the surface as a beam supported on two supports with varying cross-sections, as shown in Fig. 3.22. The surface's geometry and characteristics vary with position. The haptic resonators have a rigid surface due to their multi-layered composition, consisting of 500 μm of glass, 200 μm of PZT and 100 μm of PEEK polymer film. In contrast, the surface between the resonators is not rigid, since only the 100 μm PEEK film is present. The beam is point-loaded at the center, specifically in the middle of the central resonator.
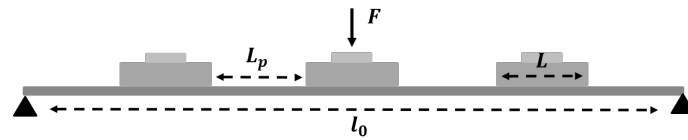
Figure 3.22: Haptic surface assimilated to a bending beam.

The maximum deflection of a beam on two supports with a load at its center is a well-known situation. However, this calculation is typically done for homogeneous beams, where the cross-section or material does not change. In this case, the beam is heterogeneous. Thus we choose to perform numerical calculations to determine the deflection. We will then compare these results to those of a homogeneous beam made of PEEK with a thickness to be determined. So, for a given resonator length L_p, we will be able to determine the maximum deflection under a unit load, and we will equate this to a thickness h_{hom} in the case of a homogeneous beam.

We therefore chose to simulate this situation with a COMSOL 2D study using the same parameters for the materials as previously. The beam is placed on two of its edges. A unit load is applied to the middle of the central resonator. A parametric study is carried out to vary the hinge length L_p from 2 mm to 20 mm and plot the deflection amplitude δ_S at the center of the beam.

In the table 3.2 we present the deflection δ_S for a surface produced with a PEEK film of 100 μm and we depict the situation for $L_p = 10$ mm in Fig. 3.23.

Logically, the deflection δ_S increases as the distance between the resonators L_p increases. The surface thus becomes increasingly flexible for the same load. Indeed, since the size of the resonators

Table 3.2: Deflection δ_S for each L_p obtained with the heterogeneous COMSOL model.

L_p (mm)	2	4	6	8	10	12	14	16	18	20
δ_S (mm)	0.31	0.85	1.74	3.05	4.86	7.25	10.33	14.21	18.79	24.46

Figure 3.23: Deflection for a space of 10 mm obtained on COMSOL.

does not change, the length of the beam increases as L_p increases, and so does the deflection. What's more, the polymer film has a very low thickness (100 µm) and a low Young's modulus (3.5 GPa), which contributes to making the surface more flexible.

The aim is now to compare these values of the deflection characteristics of the flexibility of the solution to an homogeneous beam of PEEK of thickness h_{hom}. Indeed the deflection and so the flexibility of an homogeneous beam of PEEK supported on its two sides and charged in this center is known as :

$$\delta_{hom} = \frac{F l_0^3}{48 E_{hom} I g_{hom}} \tag{3.23}$$

with $l_0 = 4L_p + 3L$, $Ig_{hom} = bh_{hom}^3/12$, $b = 10$ mm the width of the resonator, $F = 1$ N.

Therefore, we want to equalize the deflection in the case of the heterogeneous model with the deflection in the case of a homogeneous PEEK beam of unknown thickness:

$$\delta_S = \delta_{hom} \tag{3.24}$$

As a result, for each value of L_p spacing, we can calculate the PEEK thickness h_{hom} in a homogeneous case equivalent to our heterogeneous haptic surface :

$$h_{hom} = (4L_p + 3L) \left(\frac{12}{48 b E_{hom} \delta_S} \right)^{1/3} \tag{3.25}$$

Thus we obtain for each value of L_p the thickness of PEEK equivalent to have the same deflection. We report this in Table. 3.3.

To achieve the same flexibility as the heterogeneous beam, the equivalent thickness of PEEK ranges from 730 µm for $L_p = 20$ mm to 1086 µm for $L_p = 2$ mm. The greater the distance between the

76

Table 3.3: Thickness of PEEK film for an equivalent homogeneous model with the same deflection.

L_p (mm)	2	4	6	8	10	12	14	16	18	20
h_{hom} (µm) for $\delta_{hom} = \delta_S$	1086	933	864	823	796	776	761	748	739	730

resonators, the smaller the equivalent thickness. We note that for L_p is 10 mm the equivalent thickness is 796 µm, which corresponds to the maximum thickness of 800 µm of our surface (500 µm of glass + 200 µm of PZT + 100 µm of PEEK).

Fig. 3.24 shows the evolution of the deflection δ_S as a function of L_p in the case of the heterogeneous model obtained on COMSOL and for different values of the equivalent PEEK thickness h_{hom} according to a homogeneous beam model of Table. 3.3.
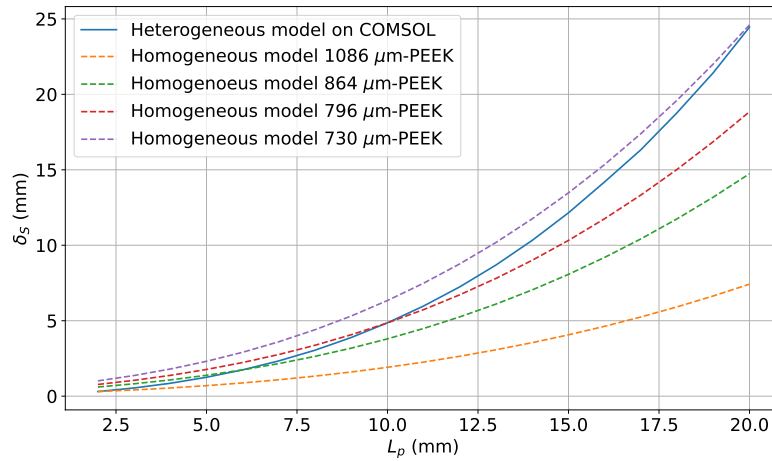
Figure 3.24: Deflection δ_S obtained with the heterogeneous model on COMSOL and with homogeneous beam model.

We can therefore see that in our heterogeneous case the deflection δ_S does not evolve in L_p^3 as it does in the case of a homogeneous beam on equation 3.23.

In this section, we have numerically calculated the maximum deflection δ_S for the haptic surface in a unidirectional case, enabling us to quantify the flexibility of our solution under unit load. By comparing these results with those obtained in the case of a homogeneous beam, we are able to determine, depending on the distance between the resonators L_p, an equivalent beam model of homogeneous thickness made from the PEEK polymer. Thus depending on the distance between the resonators L_p, the surface can be considered as flexible as a PEEK beam with a thickness of between 730 µm and 1086 µm.

In the following, we ask whether this flexibility has an impact on the mechanical response of the haptic surface.

3.5.2 Impact of flexibility on mechanical response

In this section, we want to determine the minimum curvature radius R_c that does not change the mechanical behavior of the haptic resonators.

Therefore, several impedance with different radii of curvature of the surface are conducted. Here, we draw inspiration from previous works that validated flexible electronic devices [111, 112, 113, 114]. Accordingly, our polymer surface is fixed to a support using tape. One of the support' sides is mobile with a screw nut mechanism, allowing us to bend the polymer surface. Different surfaces with PEEK 100 µm or KAPTON 75 µm films and distances of $L_p = 6$ mm, 10 mm, or 13 mm are chosen here.

To calculate the radius of curvature R_c, we measure the chord l_f and the deflection δ_S using a caliper as shown in Fig. 3.25.
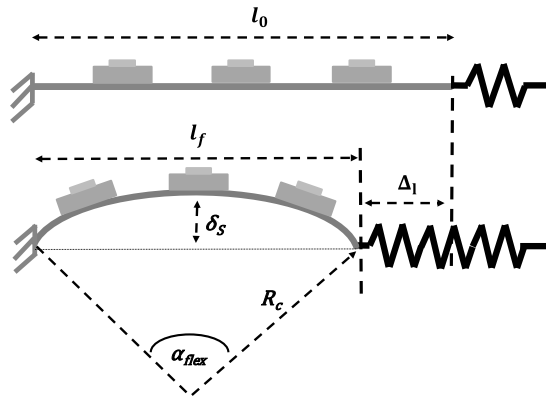
Figure 3.25: Set-up drawing for bending study.

Using the Pythagorean theorem, we have from this drawing :

$$R_c^2 = (\frac{l_f}{2})^2 + (R_c - \delta_S)^2 \tag{3.26}$$

This gives us the radius of curvature as a function of l_f and δ_S :

$$R_c = \frac{l_f^2}{8\delta_S} + \frac{\delta_S}{2} \tag{3.27}$$

When the radius of curvature is too small to measure the deflection accurately, as presented for example in Fig. 3.26.b), the radius of curvature is directly measured using the caliper. For each surface, we measure the impedance of both the central and a single external resonator.

<div align="center">a)   b)</div>
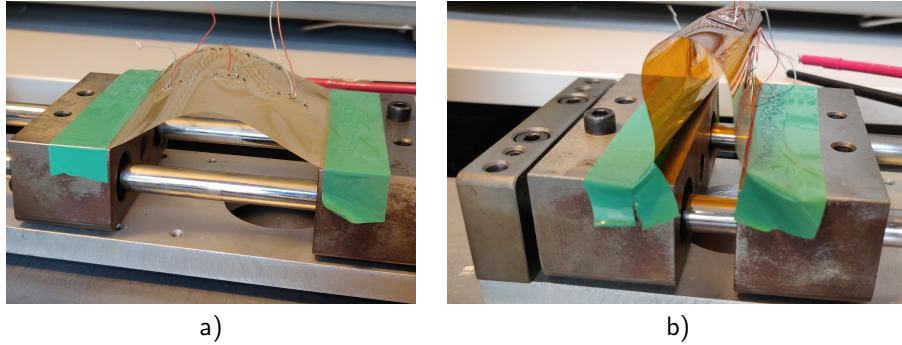
Figure 3.26: a) Large curve radius for PEEK; b) Small curve radius for KAPTON.

The impedance plots for PEEK, are depicted in Fig. 3.27.

The curves show discrepancies between the surfaces and also between resonators, even when the radius is infinite. Such discrepancies arise due to the manufacturing process of the resonators, which is manual and not repeatable. Furthermore, the electrical wires and connectors appear to have added a significant amount of noise to these measurements. This is not an issue in this study as the objective is to compare various bending states for the same surface.

The study illustrates that the bending and curvature effect does not impact the external resonators : the impedance modulus remains constant for the cases observed on Fig. 3.27.a), c) and e).

For the central resonator, the resonance frequency is shifted and the modulus of impedance drops as the radius of curvature R_c is lower than 23 mm. For instance, using a 6 mm spacing, a substantial alteration in impedance occurs between a 23 mm and a 29 mm curvature radius (Fig. 3.27.b). The same conclusion holds for $L_p = 10$ mm in Fig. 3.27.d), but not for $L_p = 13$ mm in Fig. 3.27.f).

Thus, as the distance between the resonators increases, the radius of curvature can be reduced without affecting the mechanical behavior of the resonators.

In addition, a bending radius R_c greater than 23 mm has no effect on the mechanical behavior of the resonators. This conclusion is important for our research. In fact, the typical adult wrist circumference $2\pi R_c$ ranges from 14 cm to 20 cm [115], resulting in a bending radius R_c greater than 22 mm. As a result, we can comfortably accommodate a small wrist without changing the electromechanical
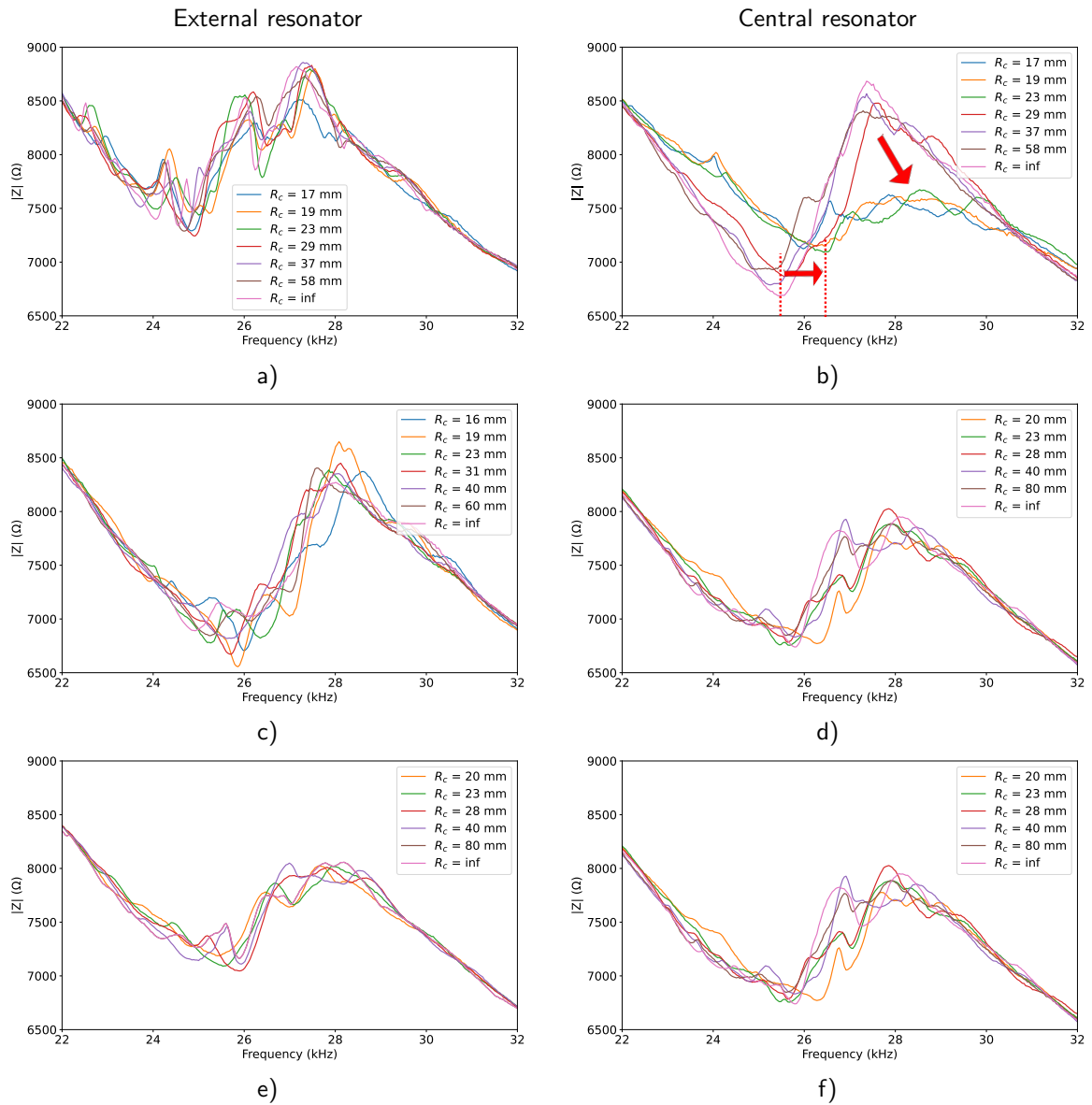
Figure 3.27: Impedance of external resonator : a) 6 mm gap, c) 10 mm gap, e) 13 mm gap; Impedance of central resonator : b) 6 mm gap, d) 10 mm gap, f) 13 mm gap.

performance of the interface. In Fig. 3.28 we can see some of these interfaces adapted to a cylindrical support with a radius of curvature R_c of 20 mm or 35 mm.

Figure 3.28: Interfaces on cylindrical supports.

3.6   Conclusion

This chapter presents the design of a surface composed of nine haptic resonators. The wave emitted by the haptic resonator on the surface of the polymer film is investigated. An assembly of two resonators separated by the distance L_p is then created. In the case where only one resonator is active, the polymer film is assimilated to a free-clamped beam model. From this simplified model, the distance L_p that maximizes the surface displacement is obtained. Then, by the principle of superposition, the displacement at the surface is modeled when two resonators are active. This simplified model is validated by COMSOL simulations and electromechanical measurements. Vibration amplitudes greater than 1 µm were confirmed at a low voltage of 20 Vpp at the resonant frequency. Next, a surface of 3 x 3 haptic resonators was presented. The haptic resonators are separated by the optimized distance L_p. The presented surface can be divided into three different zones where the displacement field is simplified. Numerical simulation in COMSOL shows that these different displacement zones can be used to create localized zones or large areas of haptic sensation, thanks to the combination of haptic resonators and the continuity of vibrations on the polymer film. Finally, this chapter highlights the flexibility of the haptic surface. In a 1D model, the haptic surface has a flexibility similar to that of a homogeneous beam of PEEK film with a thickness between 730 and 1086 µm under a unit load. In addition, an electromechanical study has shown that the proposed haptic surface can conform to small radii of curvature, such as a human wrist, without degrading the electromechanical performance of the resonators.

The next chapter aims to produce these interfaces on a more industrial scale, thereby limiting the defects and inconsistencies associated with manual interface fabrication.

Chapter 4

Realization of demonstrators

Contents

4.1 Introduction

In this chapter, the objective is to implement the designed interfaces using industrial tools. Firstly, the fabrication process and its main steps are detailed in 4.2. Two distinct methods to realize the bottom electrode of the haptic resonators are proposed and different interface configurations are tested. Following this, the various interfaces are validated through geometric verifications and electrical characterizations in 4.3. Additionally, the environmental impact of our technology is investigated and a Life Cycle Assessment (LCA) study is proposed in 4.4 to compare the two manufacturing methods to realize the bottom electrode of the haptic resonators. Finally, an electronic circuit is designed in 4.5 to control the flexible haptic surfaces.

4.2   Fabrication of the surface

The haptic surface designed in the previous two chapters is now manufactured through a specific fabrication process. This process is generic and can be used to build any interface configurations with any resonator dimensions. Subsequently, different resonator dimensions, PZT thicknesses and polymer films are tested, as shown in Table 4.1. In this way, we will show that this technology and its manufacturing process can be adapted to different uses and applications. The distance between resonators L_p is set at 10 mm or 6 mm. Two interfaces, 10 mm and 6 mm apart, are produced on a single PEEK or KAPTON substrate. As shown in Chapter 3 in Table 3.1, for the 100-µm PEEK film 6 mm corresponds to an optimum for 3 vibration nodes and 10 mm is almost an optimum for 5 vibration nodes. Thus, the chosen space L_p does not correspond to the optimal distance for both polymer films simultaneously. However, it enables the fabrication of two interfaces for each substrate, PEEK or KAPTON, using only one set of masks. The 200 µm thick PZT ceramic on the market is thinned to 150 µm or 75 µm. The aim is to reduce the overall thickness of the solution and the rigidity of the haptic resonator. This means that, for the same voltage, the resonator with thinner PZT ceramic will be more energy-efficient, and better displacements will be achieved [116].

Table 4.1: Interface dimensions tested.

Rigid	Material	Glass - 500 µm
substrate	Size	10 mm x 10 mm / 8 mm x 8 mm
PZT Actuator		Ø 5 mm x 150 µm / Ø 5 mm x 75 µm / Ø 3 mm x 150 µm
Polymer film		PEEK 100 µm - KAPTON 75 µm / 50 µm
Space between resonators		10 mm / 6 mm

The haptic interface is created using an innovative process (Fig. 4.1) performed in the cleanrooms of CEA-Leti and CEA-Liten for two specific steps, as explained in the following.

4.2.1   Resonator fabrication

Process

The rigid vibrating plates are fabricated on a 500 µm - thick glass wafer (Eagle glass) in cleanroom using the steps described in the following and as presented on Fig. 4.2.

The initial stage is to opacify and mark the back of the glass substrate, for the purpose of enabling
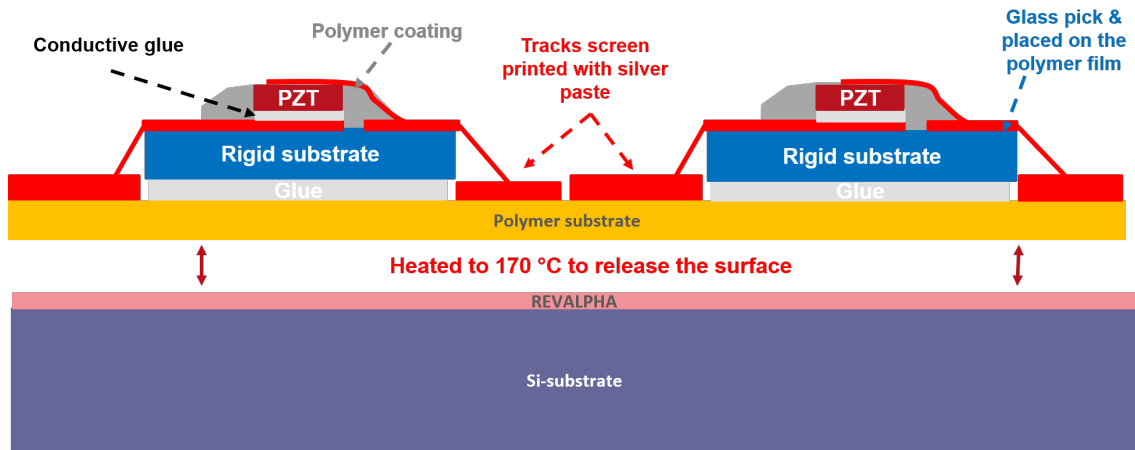
Figure 4.1: Cross section of the fabrication process.

Figure 4.2: Cross section of the first steps of fabrication.

subsequent equipment alignment. Opacification and marking of the glass substrate is accomplished by depositing 100 nm of titanium (Ti) followed by 500 nm of silicon nitride (SiN).

The bottom electrode is then deposited on the substrate. Two different methods were evaluated. The first technique involves depositing metal through physical vapor deposition (PVD) by sputtering, followed by photolithography, etching, and stripping for cleaning. This creates an electrode consisting of 50 nm of tungsten (W), 50 nm of tungsten nitride (WN), and 200 nm of gold (Au). Another technique utilizes screen-printed silver ink for the bottom electrode; 10 μm of a conductive silver paste (ELEPASTE NP1) is deposited and then annealed at 100°C for 15 minutes. A comparison of the electromechanical performance and environmental impact of both techniques are evaluated in the next section.

A second screen-printing also followed by an annealing process is performed to deposit the conductive adhesive (H20E) used to bond the PZT ceramics (PI 255). Ceramics of ⌀ 5mm × 200 μm, or ⌀ 3mm × 200 μm, are placed using a pick and place tool (DATACON 2200 Evo advanced). A polymer layer ("globtop" Namics G8345-146), in gray in Fig. 4.2, is then deposited all around the ceramics in order to electrically isolate the bottom electrode from the future upper electrode. To obtain the desired

thickness the ceramics are thinned by a grinding technique. This technique makes it possible to obtain thin ceramic thicknesses and bridge a technological gap. Indeed thin-film piezoelectric materials can only achieve thicknesses thinner than 10 to 20 μm, while piezoelectric ceramics on the market have minimum thicknesses around 100 to 200 μm. The top electrode is created by directly evaporating a 20 nm layer of titanium (Ti) and a 500 nm layer of gold (Au) in a vacuum through a stencil.

Following this process, we built on the wafer piezoelectrically actuated glass resonators. To conclude the first part of the fabrication, a water jet cutting is carried out to obtain 49 resonators as presented Fig. 4.3.
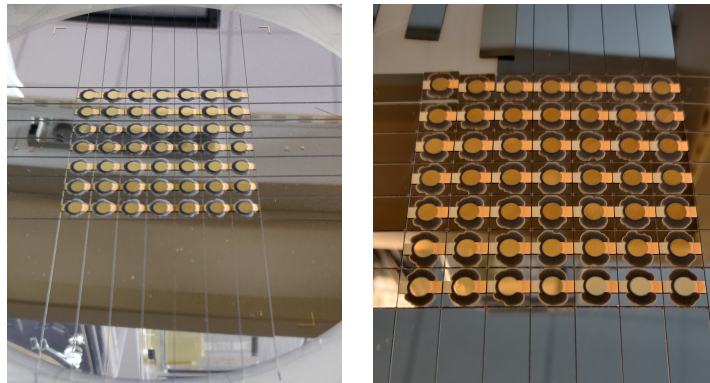
Figure 4.3: Substrates at the end of the steps.

Geometric verification

To check the dimensions of our resonators, we utilize both a conventional microscope and a scanning electron microscope (SEM) to acquire images. Fig. 4.4, Fig. 4.5, and Fig. 4.6 present the top and cross-sectional views of the resonators.

The PZT ceramic is located in the center and is connected to the top gold electrode, which faces to the left of the resonator, as shown in Fig. 4.4. The ceramic diameter is 5 mm for the initial resonators and 3 mm for the last ones. The polymer layer surrounds the ceramic to isolate the top electrode from the bottom electrode. The circumference of the globtop differs slightly among the three cases, but it does not affect functionality. The bottom electrodes are located to the right of the resonators. The gold electrode, acquired through photolithography on the first resonator as shown in Fig. 4.4.a), is discernible but not easily visible, whereas the silver electrode is clearly observable. The resonator,
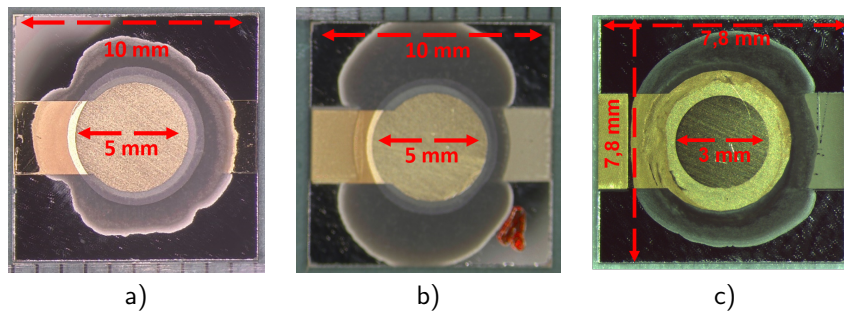
Figure 4.4: Top views of the resonators : a) 10 mm x 10 mm resonator with a gold bottom electrode; b) 10 mm x 10 mm resonator with a silver bottom electrode and c) 8 mm x 8 mm resonator with a silver bottom electrode.

measuring 8 mm x 8 mm, is smaller than expected due to cutting uncertainty, and therefore measures 7.8 mm in terms of its square side.
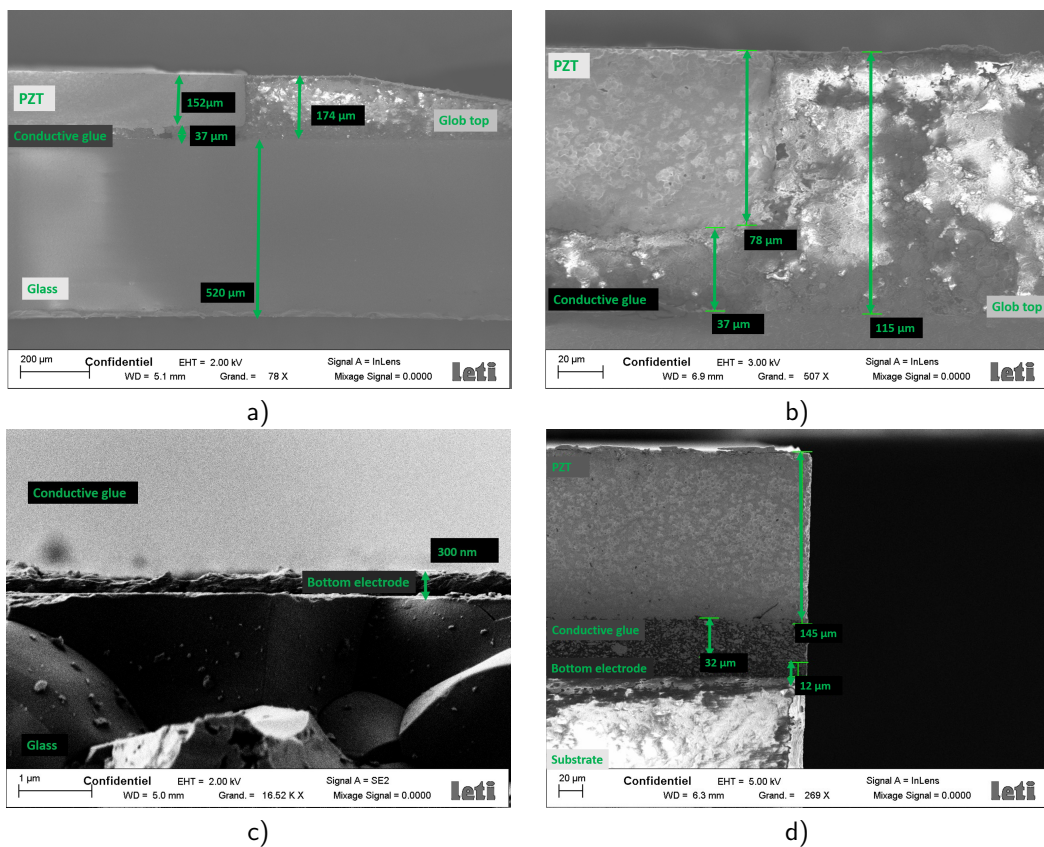
Figure 4.5: SEM cross-sections of resonators with a PZT thickness of: a) 150 μm or b) 75 μm; c) Zoom on the gold bottom electrode and d) Resonator with a silver bottom electrode.

87

The thickness of the grinded PZT is between 145 and 155 µm as presented Fig. 4.5.a) and Fig. 4.5.d). We have also proven the possibility of obtaining a thickness around 75 µm as expected and presented on Fig. 4.5.b). So the grinding technique uses to create thin PZT ceramics is efficient and enables to bridge the technological gap between thin film and ceramic piezoelectric materials. The conductive adhesive thickness between the glass and the PZT ceramic varies slightly between 30 and 40 µm without major impact on the resonator behavior.

The total thickness of the glass substrate is measured as being 520 µm rather than 500 µm as expected. It corresponds to the uncertainty announced by the glass manufacturer, to which is added the layer used to opacify the glass. This results in a resonator frequency increased.

In the cross-section on Fig. 4.5.c), the bottom electrode made with a photolithography is presented. Measurement reveals an electrode thickness of around 300 nm as expected. Similarly, the bottom electrode obtained by screen-printing technique is around 12 µm thick, very close to the desired thickness (10 µm), Fig. 4.5.d).

Finally, the thickness of the top electrode presented on Fig.4.6 is around 520 nm as wanted.
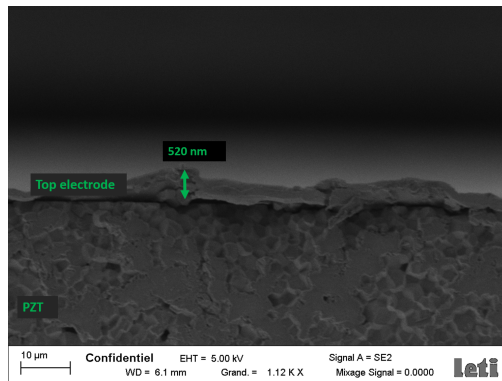
Figure 4.6: SEM cross-section of the top electrode.

4.2.2   Interface fabrication

Process

In the second part, the haptic resonators are integrated on the flexible substrate (Fig. 4.7). For this purpose, a REVALPHA thermal release film is laminated on an 8-inch silicon wafer followed by the lamination on the polymer substrate. In this way, it is possible to carry out conventional manufacturing

steps in cleanroom on the flexible substrate. The electronic tracks are then screen-printed on the surface with the same technique than for the bottom electrode on the glass substrate. Then the resonators made on glass wafer are bonded with epoxy glue (E505) by a pick and place technique, followed by annealing. The electrical contacts are made with a silver ink between the tracks on the polymer and the electrodes on the resonators.
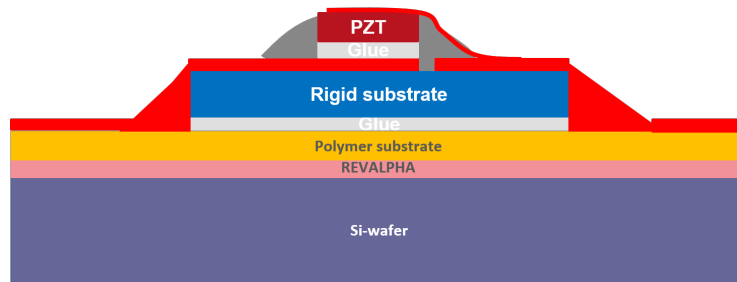
Figure 4.7: Substrate at the end of the interface fabrication steps.

The two types of substrate with the two polymers selected in chapter 2 are shown Fig. 4.8. On each wafer, four surfaces of nine haptic resonators are realized. There are two small areas with 6 mm spacing between resonators and two large areas with 10 mm spacing.
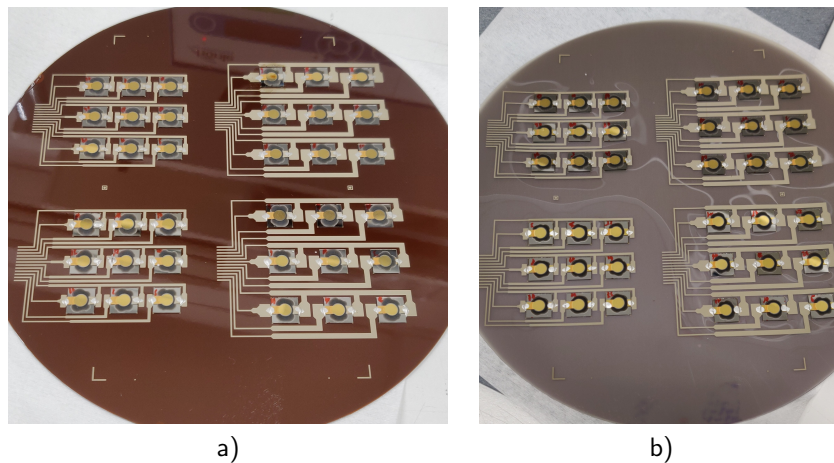
Figure 4.8: Substrate with a) the instrumented Kapton polymer and b) the instrumented PEEK polymer.

Then the silicon wafer is heated to 170°C, which allows the REVALPHA film to disintegrate and the surface to be released as shown Fig. 4.9. In principle, both PEEK and KAPTON polymer films can resist this temperature of 170°C. Validation tests have also shown that both polymers do not degrade at this temperature. In the final process, in some situations the PEEK film is degraded during this stage,

as seen on the dotted red areas. As a result, the resonators tend to lift off the film. In the following the results and surface characterizations for both types of polymer will be presented. However, in future developments, the KAPTON film will be preferred. Then the instrumented polymer film is cut to obtain
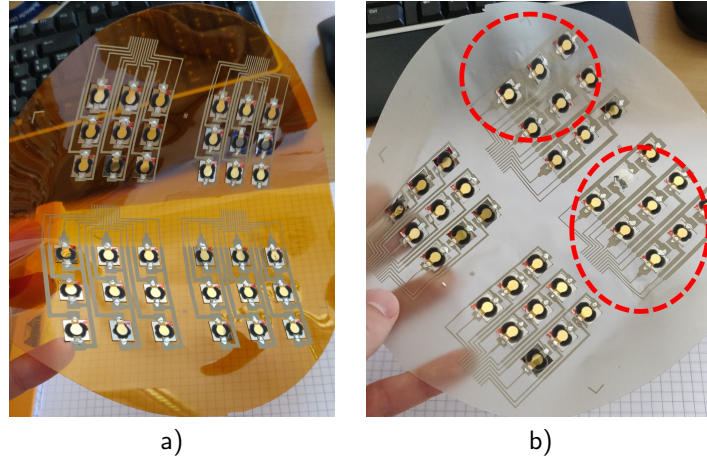
Figure 4.9: a) The instrumented KAPTON polymer and b) the instrumented PEEK polymer after the release of the REVALPHA film.

the four surfaces and a flexible connector is assembled to each surface to recover the connections of the electronic tracks. Lastly, an insulating coating is applied to insulate and protect the electronic tracks.

Geometric verification

Fig. 4.10 shows one of the interfaces produced, with a bottom view and a top view when the surface is fixed to a cylindrical support with a radius of 3 cm.

4.3 Electrical characterization and validation

4.3.1 Resonator measurement

Electrical characterizations are carried out on piezoelectric resonators before their integration onto the polymer film, to confirm their functionality. To do this, measurements were taken using an impedance analyzer (Keysight E4990A) with a prober (MPI TS200) under tip to obtain the electrical impedance and so the resonance frequency of the resonators.

Figure 4.10: a) Surface obtained at the end of the process; b) Surface on a cylindrical support of radius 3 cm.

This has been done for the two types of resonator presented above with a PZT thickness of 150 μm and a side of 10 mm.

Fig. 4.11 shows the impedance modulus of three resonators for two different substrates of each type (*P01_R1_pho*, *P01_R2_pho*, *P01_R3_pho* and *P02_R1_pho*, *P02_R2_pho*, *P02_R3_pho* for the bottom electrode with photolithography and *P03_R1_pho*, *P03_R2_pho*, *P03_R3_pho* and *P04_R1_pho*, *P04_R2_pho*, *P04_R3_pho* for the bottom electrode with screen-printing technique). We want here to analyze the dispersion between substrates and on each substrates.
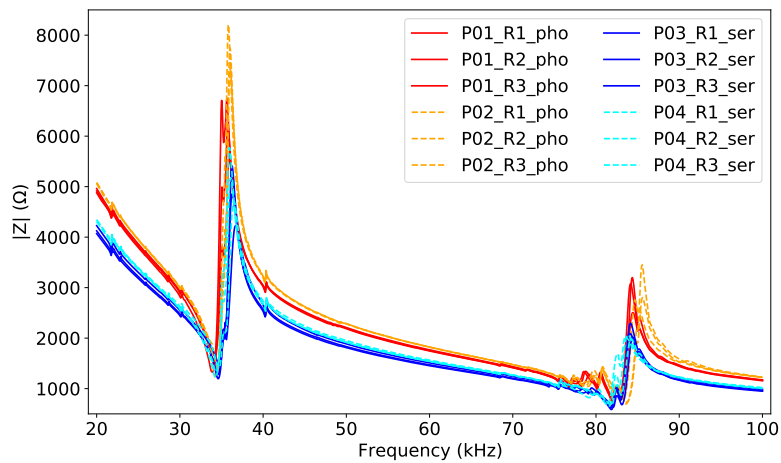
Figure 4.11: Impedance obtained for three resonators of two different substrate for the two methods of fabrication of the bottom electrode.

This shows that the resonant frequency of the first mode is higher than expected. It averages

34.5 kHz rather than 29.8 kHz obtained in Table 2.4. This is due to the slight difference in resonator dimensions already presented in the previous section. We note that for both types of manufacture, the mean resonance frequency is very close: 34.6 kHz for screen printing and 34.4 kHz for photolithography. The resonance frequencies show homogeneity within the same substrate type, with a low standard deviation of 200 Hz calculated from the measurement of 10 resonators.

On Fig. 4.12 impedance obtain for different configurations are presented. We plot again three 10 mm x 10 mm resonators with a bottom electrode in gold (*R10mm_PZT150μm_pho*) and 10 mm x 10 mm resonators with a bottom electrode in silver (*R10mm_PZT150μm_ser*). Then we add three 10 mm x 10 mm resonators where the PZT ceramic thickness is 75 μm (*R10mm_PZT75μm_pho*) and three 8 mm x 8 mm resonators (*R8mm_PZT150μm_ser*).
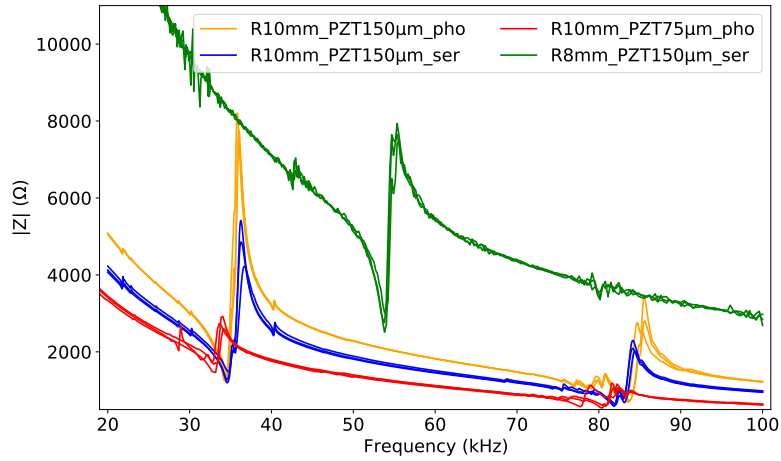
Figure 4.12: Impedance obtained for three resonators of each design.

As we can see, the first mode of vibration is shifted to high frequency for the 8 mm x 8 mm resonator which measured in fact 7.8 mm by 7.8 mm. This was expected as shown on the chapter 2 when the design was done. So the frequency of resonance of this resonator is at 53.9 kHz. For the resonator of 10 mm x 10 mm with a PZT thickness of 75 μm, the frequency is a little bit lower than for the other 10 mm x 10 mm resonator. The frequency is at 33 kHz.

The BVD model presented in chapter 2 is used to calculate the various circuit parameters (Fig. 2.16). The equations and the quality factor are recalled :

$$\omega_r = \sqrt{\frac{1}{LC}} \tag{4.1}$$

92

$$\omega_a = \omega_r \sqrt{1 + \frac{C}{C_0}} \tag{4.2}$$

and :

$$Q = \frac{1}{R}\sqrt{\frac{L}{C}} \tag{4.3}$$

On the table 4.2 the parameters are presented for the four different types of haptic resonators. The capacity C_0 represents the electrical circuit's capacity and is also measured with the impedance analyzer. It directly depends on the surface and thickness of the PZT ceramic, and to some extent on the electrodes. The capacitance C_0 differs depending on whether the bottom electrode is fabricated via photolithography (1 nF) or screen printing (1.2 nF), despite identical PZT thickness and size. Normally, if the ceramic thickness is reduced by half, the capacitance is doubled, as $C_0 \propto surface/thickness$. However, this does not hold true in the current situation since C_0 changes from 1 nF to 1.6 nF when the PZT thickness decreases from 150 μm to 75 μm. Moreover if the size of the resonators changes, then the surface area of the PZT also changes by a factor of $5^2/3^2$, which is approximately 2.8. In all cases, the capacity is less than 2 nF. These values will allow us to properly size our electronics.

Then we calculate at resonance $C = C_0 \frac{\omega_a^2 - \omega_r^2}{\omega_r^2}$ and $L = \frac{1}{C_0(\omega_a^2 - \omega_r^2)}$ To finally obtain the quality factor Q.

Table 4.2: Parameters of BVD circuit for haptic resonators.

	R10_P150μm_pho	**R10_P150μm_ser**	**R10_P75μm_pho**	**R8_P150μm_ser**
ω_r (kHz)	34.4	34.6	33	53.9
ω_a (kHz)	35.9	36.3	33.8	55.3
R (Ω)	1400	1300	1700	2800
C_0 (nF)	1.0	1.2	1.6	0.6
C (pF)	89	121	79	29
L (mH)	240	175	298	301
Q	37.1	29.3	36.1	36.4

We therefore have a fairly low quality factor in all situations. Our resonators are not very selective. This is not necessarily a disadvantage in our situation, since we do not want to create a filter. The differences in the resonators are slight, with a standard deviation of 200 Hz per type of resonator, but it is interesting because we are going to be able to operate all the resonators at the same frequency. As a result, the electronic actuation will become simplified and would not require specificity for each resonator.

4.3.2   Post simulation

The selected glass for the resonator fabrication is more rigid than anticipated in the FEM study. Specifically, the Corning Eagle XG glass was chosen in the cleanroom with a Young's modulus of 73.6 GPa, a density of 2380 kg/m^3, and a Poisson's ratio of 0.23, instead of the previously chosen one with E = 65 GPa, ρ = 2300 kg/m^3, and a Poisson's ratio of 0.2. Furthermore, the SEM view (Fig. 4.5.a) indicates that the glass thickness measures 520 μm. There is also a slight uncertainty regarding the resonator size in some case for the 10 mm x 10 mm haptic resonators and as explained before, the 8 mm x 8 mm measured actually 7.8 mm x 7.8 mm. After recalculating the frequency using the equation 2.25 with appropriate parameters, we analytically determined that the 10 mm x 10 mm resonators should have a frequency of 32.7 kHz and the 8 mm x 8 mm resonators have a frequency of 53.7 kHz. This leads to improved agreement with the experimental measurement. The small discrepancy, around 5 %, between the frequencies presented in Table 4.2 and those currently being calculated is because other thicknesses, such as electrodes or adhesive, were not considered.

4.3.3   Interface

Similarly, the impedance is graphed in various configurations for 9-resonator interfaces to confirm their resonant frequencies.

KAPTON film vs PEEK film

Fig. 4.13 exhibits the impedance of three different surfaces. The PEEK polymer surface, which employs a 10 mm resonator and a bottom electrode created through photolithography, is highlighted in red (*P100μm_R10mm_pho*). The other two interfaces are made of 75 μm thick KAPTON polymer. The resonators colored blue, 10 mm in size, possess a bottom electrode made via photolithography (*K75μm_R10mm_pho*). Conversely, the orange resonators have a bottom electrode fabricated through screen-printing (*K75μm_R10mm_ser*). The thickness of the PZT remains constant at 150 μm in all three instances. Measurements have enabled quantification of the resistivity of the electronic tracks on the polymer films, which range from 3.5 Ohm for the shortest track to 17.6 Ohm for the longest track.

The addition of the polymer shifts the resonance frequency towards the lower frequencies, as already seen for the manually-produced haptic resonators in chapter 2. The impedance and the phase show
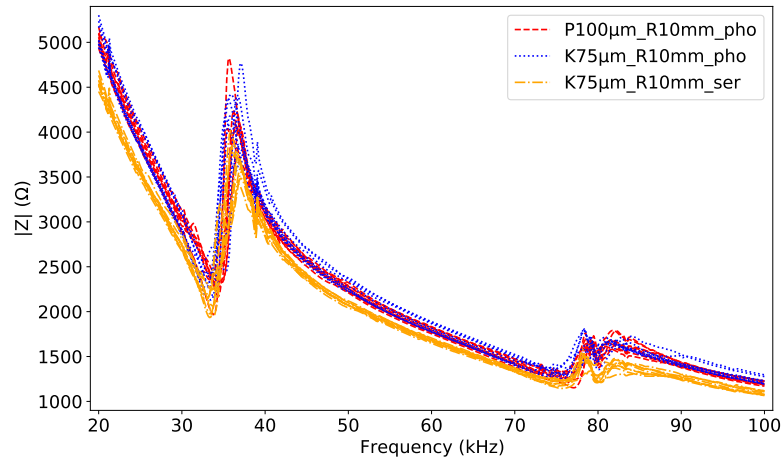
Figure 4.13: Impedance obtained for surfaces with PEEK-100 µm and KAPTON-75µm.

greater fluctuations between resonators, Fig. 4.14, when compared to Fig. 4.12, due to the inclusion of the epoxy layer, polymer film and electrical tracks. Mean resonance is now around 32 kHz for the interfaces with the 10 mm x 10 mm resonators as presented on the table 4.3. Resonance frequency dispersion for resonators on the same surface is $\pm$ 500 Hz.
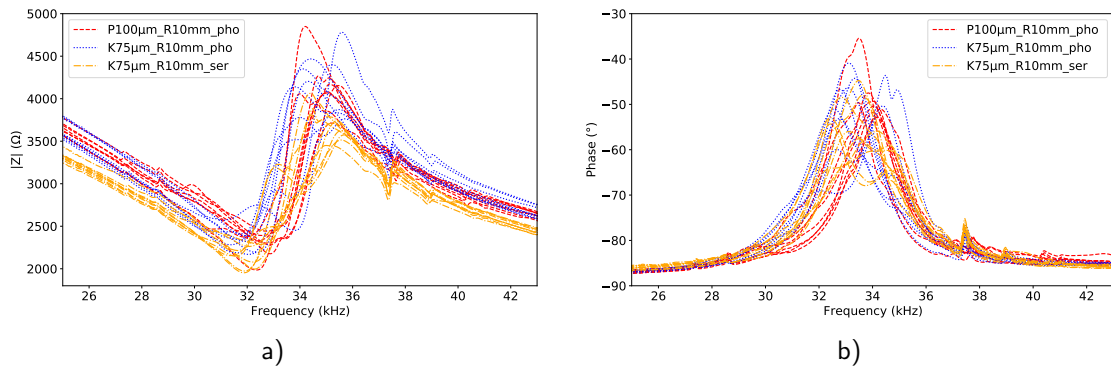
Figure 4.14: a) Impedance and b) phase obtained for the three surfaces around the resonance.

The inclusion of electronic tracks on the substrate, flexible connectors, and bonding between electronic tracks and resonators causes a slight change in the capacitance C_0. However, this value remains below 2 nF. The quality factor is also calculated and found to be very low, similar to before. As previously stated, the addition of polymer and a layer of adhesive has a considerable damping effect.

We will now shift our focus to the KAPTON surface due to complications with the PEEK surface

Table 4.3: Parameters of BVD circuit for haptic surfaces.

	P100µm_R10mm_pho	**K75µm_R10mm_pho**	**K75µm_R10mm_ser**
ω_r (kHz)	32.7	32.0	31.8
ω_a (kHz)	35.2	34.5	35.2
R (Ω)	2300	2400	2100
C_0 (nF)	1.5	1.4	1.7
C (pF)	238	227	383
L (mH)	99	109	65
Q	8.9	9.1	6.2

arising from manufacturing.

For a surface made with a Kapton film of 50 µm, the impedance is the same than for a surface made with a Kapton film of 75 µm. The average frequency is again around 32 kHz, while the average quality factor of the nine resonators is 8.2, which is similar to the Kapton surface of 75 µm. Evidently, no tangible electrical variation exists between these two distinct types of surfaces. We will examine in the subsequent chapter the effect of varying thickness on the wave since it depends directly on this thickness, as demonstrated in the equation 3.6.

Size resonators 10 mm vs 8 mm

Then two other surfaces are compared in Fig. 4.15 : the first is composed of 10 mm x 10 mm resonators (*K75µm_R10mm_ser*) and the second is composed of 8 mm x 8 mm resonators (*K75µm_R8mm_ser*).
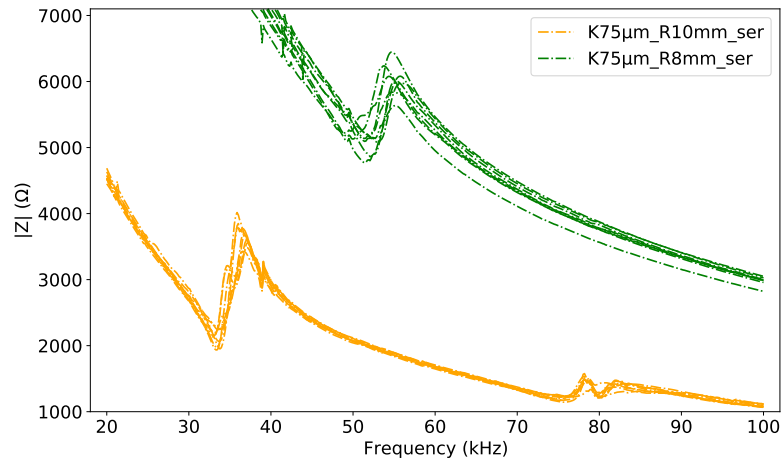
Figure 4.15: Impedance obtained for 10 mm x 10 mm resonators or 8 mm x 8 resonators.

As anticipated, the average resonance frequency of the resonators positioned between surfaces

varies significantly depending on their size. For instance, when the surface measures 8 mm x 8 mm, the frequency is around 51.5 kHz. The capacity C_0 remains almost the same as that without the polymer film, as shown in table 4.2, with a value of 0.5 nF.

Space of 6 mm vs 10 mm

Finally, we plot the impedance measurements of four other configurations (Fig. 4.16). We consider interfaces where resonators are spaced 6 mm apart (*Spa6mm_pho* or *Spa6mm_ser*) and compare that to the previous surface with a 10 mm spacing (*Spa10mm_pho* or *Spa10mm_ser*) .

a)   b)
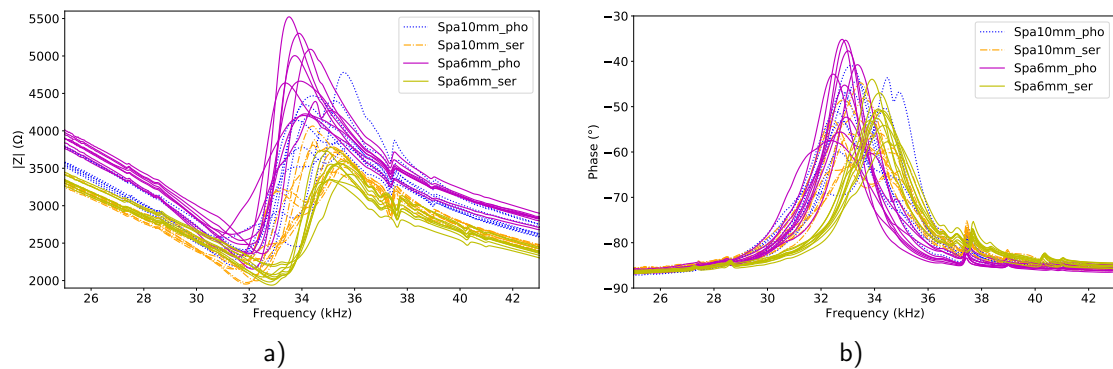
Figure 4.16: a) Impedance and b) phase obtained for space of 10 mm and 6 mm between resonators.

The average resonance frequency for two interfaces spaced 6 mm apart between resonators is almost the same than for the two interfaces with a space of 10 mm. The value of C_0 for the interface with resonators was determined to be 1.4 nF for the bottom electrode fabricated by photolithography and 1.7 nF for the bottom electrode fabricated by screen printing. The quality factor for the interfaces with a 6 mm spacing is 11.5 for the one with a bottom electrode in photolithography and 8.8 for the other one with a screen-printed electrode.

4.3.4 Conclusion

In summary, we have examined the resonators and surfaces created using the specific process, and noted that various designs are achievable through changing the polymer film and its thickness, the size of the resonators, the thickness of the PZT ceramic, and the spacing L_p between each resonator on the surface. The quality factor for each surface is low resulting to resonators less sensitive to process variation and

facilitate the balancing of the different variations of the resonance frequency. Consequently, electronic actuation becomes could be simplified and could not require specificity for each resonator. We will check that in the following.

The goal now is to develop a demonstrator based on these surfaces and evaluate its haptic capabilities. Before we are investigating the environmental impact of our haptic interfaces, in particular the manufacturing process.

4.4 Life Cycle Assessment (LCA) study

While producing the interfaces, concern regarding the environmental impact of our emerged technology. Consequently, we developed two manufacturing techniques for the bottom electrode. Both techniques were observed to produce a comparable electrical response. Consequently, this section provides a comparative analysis of their environmental impact via a Life Cycle Assessment (LCA) study, allowing us to distinguish between the two techniques. This study was conducted with the assistance of Laura Vauche of the Eco-innovation team in the Silicon Components Department (DCOS) in CEA-Leti.

4.4.1 Environmental context

In the context of climate change and resource depletion, the goal today is not only to produce the most efficient technology, but also to reduce its environmental impact. To this end, life cycle assessment is becoming more prevalent in the microelectronics industry. This sector's environmental impact is undeniably substantial, but data on it is scarce. However, according to Freitag et al [117], information and communication technologies (ICT) utilizing microelectronic technologies could contribute to 1.8 to 3.9 % of global greenhouse gas emissions (GES) by 2020. Additionally, electronic technologies are expected to continue to evolve, and the semiconductor market could reach $1000 billion by 2030, up from $550 billion in 2022 [118]. Controlling and reducing the environmental impact of micro and nanotechnologies has become increasingly critical.

To accomplish this, life cycle assessment (LCA), standardized to ISO 14040 and 14044, is used. LCA allows for the evaluation of a system or component, such as a product, process, or component, across its entire life cycle in terms of its environmental impact, as demonstrated in Fig. 4.17 for a microelectronic device case. The input flows consist of the elements used during manufacture, use, and

end-of-life, while the output flows include the emissions and products generated at each stage. This approach enables us to compare different technologies and make informed decisions that balance cost, performance, and environmental impact.
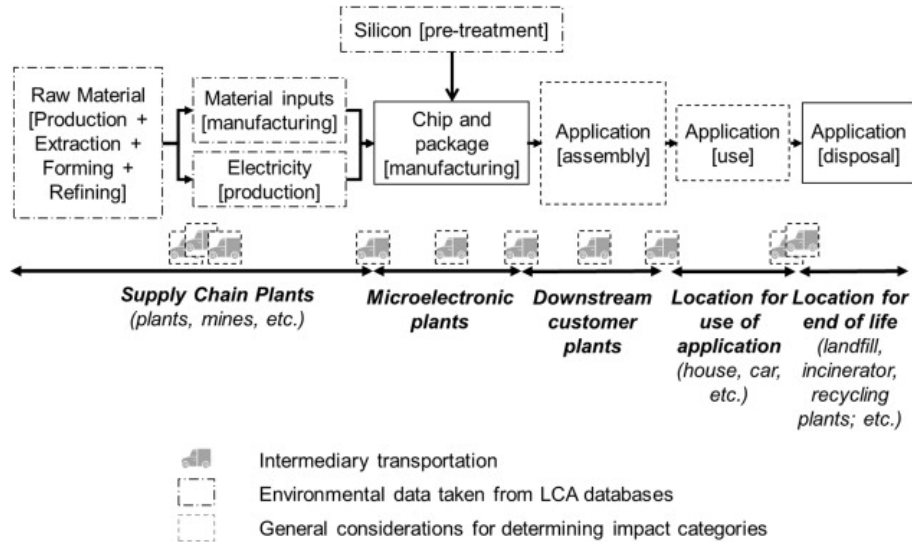
Figure 4.17: General phases in a component life cycle for microelectronic devices [119].

According to the ISO standard, an LCA study has four main stages (Fig. 4.18) : goal and scope definition of the study, inventory analysis, impact assessment and interpretation of the results. In the following, these four stages will be used to carry out a study on our technology.
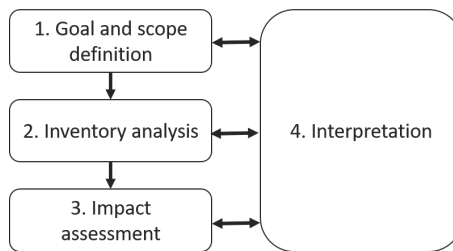
Figure 4.18: LCA framework based on ISO 14040.

4.4.2   Scope of the study

Our technology is still in development. In this case, there is no use or end-of-life cycle. Therefore, our study starts with the extraction of raw materials and ends with the manufacturing process described

above. The manufacturing process consists of numerous stages, with over 70 steps in total. While we only presented the main steps earlier, it is important to note the extensive process involved. For instance, the process of creating stencils for evaporating the top gold electrode is not detailed. In this type of study, it is essential to detail all the related steps that lead to the final product. However, this is a time-intensive process since it requires fetching data on incoming and outgoing flows from the cleanroom, which must be repeated for each step and recipe. It is also required to obtain information from subcontractors about the products that enter the manufacturing process.

As a result, the research focuses on the manufacturing of the bottom electrode. In the previous section, two electromechanically tested and approved solutions were examined. The objective is to determine the approach with the least environmental impact. Table 4.4 illustrates the detailed fabrication steps for each method.

Table 4.4: Steps used to fabricate the bottom electrode.

Photolithography		
Process	**Step**	**Description**
M_ELEC_INF_DEP_MET	PVD metal deposition - 50 nm W, 50 nm Wn and 200 nm Au	
~~M_ELEC_INF_PHOTO~~	~~Resin deposition~~ ~~Insulation~~	~~JSR420 1,5μm~~
M_ELEC_INF_GRAVURE_1	Steaming Descum Wet Etching	150°C - 30mn 20s Au 200nm (210 s)
~~M_ELEC_INF_GRAVURE_2~~	~~Steaming~~ ~~Descum~~ ~~Wet Etching~~	~~150°C - 30mn~~ ~~20 s~~ ~~W 50nm and Wn 50 nm (300 s)~~
~~M_ELEC_INF_GRAV_CASQ~~	~~Wet Etching~~	~~(120 s)~~
~~M_ELEC_INF_GRAV_STRIP~~	~~Stripping~~	~~(10 mn)~~
Screen-printing		
Process	**Step**	**Description**
M_ELEC_INF_SERIG	Screen printing	10 μm ELEPASTE NP1
M_ELEC_INF_STEAM	Steaming	100°C - 15 mn
M_ELEC_INF_CLEAN	Screen and squeegee cleaning	

Photolithography involves depositing metal and resin, insulation, and multiple etching passes to etch gold (Au), followed by tungsten (W) and tungsten nitride (WN). This process is subdivided into several stages, and concludes with a stripping step. In contrast, screen printing only requires three steps. As a result, screen printing reduces interface production times during device manufacture. This study aims to determine if this time-saving process also provides environmental benefits. The manufacturing of

photolithography masks and screen printing frames by third-party companies falls outside the scope of our study.

We will focus only on the PVD metal deposition step M_ELEC_INF_DEP_MET and on one step of etching with the gold etching step M_ELEC_INF_GRAVURE_1, as presented in Table 4.4. The remaining steps are denoted in italics and crossed out. Indeed we know from previous work done by the CEA-Leti Eco-innovation team that these two steps contribute the most to the environmental impact of the photolithography process. Therefore, we hypothesize that this will also be the case here.

4.4.3 Inventory analysis

Data on input flows are collected for each stage of the two processes. The input flows include raw materials, metals, chemicals, water, electricity, pressurized air, and gas. The collection process adheres to the scheme presented on Fig. 4.19. We do not consider the output flows in this study.
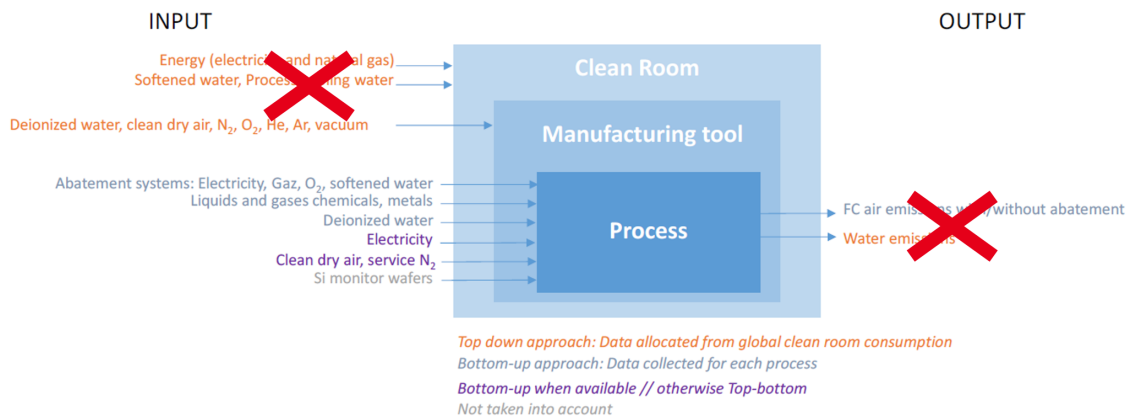
Figure 4.19: Approach for inventory analysis in this study, adapted from [120].

For the photolithography fabrication, the data is acquired from cleanroom equipment at CEA-Leti. The recipes used in this process are conventional and the data was collected by the Eco-innovation team in the Silicon Components Department (DCOS) at CEA-Leti. The obtained data were then utilized in our process. In contrast, no data was available for the production of the bottom electrode through screen-printing in a cleanroom at CEA-Liten, so we collected data on the on-site equipment during production.

In this study, only the energy consumed during the manufacturing process is considered, excluding

the energy used to operate the cleanroom (electricity, ventilation, natural gas, and water) without equipment and process steps. This "operation energy" represents approximately 65% of the global energy consumption of the cleanroom. The allocation rules for these parts are calculated using databases developed by the CEA-Leti eco-innovation team. The energy utilized by equipment for a recipe is calculated based on process time, equipment's useful surface area in the cleanroom, input energy flows (electricity, air, water, gas...), and total cleanroom consumption for processes over a year. By doing so, a portion of the total cleanroom consumption for process is assigned to the respective recipe.

Subsequently, inventory data is summarized. The amount of materials needed and water and energy (electricity, gas) usage for each substrate produced can be determined for every manufacturing process. The electricity source is based on the French energy mix.

Inventory analysis for photolithography

200 nm of gold (Au), 50 nm of tungsten (W), and 50 nm of tungsten nitride (WN) are deposited using the physical vapor deposition (PVD) process. The PVD equipment chamber is filled with argon gas which is partially ionized and generates plasma under the effect of a strong electric field. The target is bombarded by argon ions resulting in the deposition of the metal onto the substrate. It is important to note that during sputtering, the substrate cannot be exclusively targeted, leading to the metal being deposited on all surfaces of the equipment chamber. PVD experts of CEA-Leti's cleanrooms estimate that when depositing 200 nm of gold, only 10 % of the gold in the target reaches the substrate. This indicates that the process uses 9 times more gold than necessary in the first scenario.

Alternatively, returning the process kit and target to the supplier at the end of its life is another viable scenario. The remaining gold on the target and equipment is purified and recycled. Suppliers and CEA-Leti's eco-innovation team estimate that 1.4 times more gold is consumed than desired in this case. The production of the bottom electrode by photolithography allows for a comparison of the two scenarios, providing knowledge of the deposited volume for each component. Then, the masses per component are calculated based on the density, and the exact mass of each element is determined from their molar masses. For each plate, we have $0.121 * 9 = 1.09\ g$ of deposited gold for the scenario without recycling, and $0.121 * 1.4 = 0.169\ g$ of deposited gold for the scenario with recycling. We only considered the scenario without recycling for tungsten, which corresponds to $0.055 * 9 = 0.495\ g$.

As indicated in Table 4.5, to deposit 200 nm of Au, 50 nm of W, and 50 nm of WN, a total

of 0.86 kWh, 0.68 g of Argon, and 0.08 g of N2 is required. Additionally, the gold etching process necessitates a total of 4.53 kWh.

Table 4.5: Inventory analysis.

Photolithography			
Step	**Resource**		**Quantity**
M_ELEC_INF_DEP_MET	Materials (g)	Ar	0.68
		N2	0.08
		Au	0.169 or 0.9
		W	0.495
	Electricity (kWh)		0.86
M_ELEC_INF_DEP_GRAVURE_1	Materials (g)	O2	0.121
		He	0.007
		Ar	0.022
		N2	3
		H2O	173
	Electricity (kWh)		4.53
Screen-printing			
Step	**Resource**		**Quantity**
M_ELEC_INF_SERIG	Materials (g)	Ag	15.74
		Ethanol	0.316
		Acetone	0.08
	Electricity (kWh)		0.02
	Compressed air (m^3)		0.016
M_ELEC_INF_STEAM	Electricity (kWh)		1.8
M_ELEC_INF_CLEAN	Material (g)	Ethanol	2.37

Inventory analysis for screen-printing

For the screen printing process, the composition of silver ink is approximately 75 % silver. The remaining portion is made up of additives and diluents such as acetone and ethanol. Thus we consider 20 % of ethanol and 5 % of acetone. The amount of ink applied to each plate is 2 ml. By using the density of silver, which is 10.49 g/cm^3, the mass of silver deposited per plate can be determined. As a result, 15.74 g of silver is deposited per screen-printed plate. For this step, 0.02 kWh and 0.016 m^3 of compressed air are required. Afterward, steaming at 100°C for 15 minutes requires 1.8 kWh. 3 ml of ethanol is used for cleaning both the screen and squeegee.

As shown, the power consumption for each substrate produced is substantially less for the screen printing method, totaling 1.82 kWh. In contrast, photolithography requires at least 5.39 kWh, although only two primary steps are analyzed. Adding the steps that were crossed out in Table 4.4

has the potential to significantly increase power consumption, particularly with the insulation step for M_ELEC_INF_DEP_PHOTO.

4.4.4 Impact assessment and interpretation

The raw material and energy consumption data are translated into environmental impacts using SimaPro software and its "ecoinvent 3 - allocation, cut-off by classification - unit/system" database. An attributional LCA is employed, evaluating the life cycle at a specific time point. The "cut-off" approach is selected since the producer is accountable for the waste it generates and does not reap any advantages from recycling. The EF 3.1 method, developed by the European Commission as part of the PEF reference framework [121], classifies the impacts into 16 categories, each expressed in standardized units : Climate change (kg Co2 eq), Ozone depletion (kg CFC11 eq), Ionisig radiation (kBq U-235 eq), Photochemical ozone formation (kg NMVOC eq), Particulate matter (disease inc.), Human toxicity, non-cancer (CTUh), Human toxicity, cancer (CTUh), Acidification (mol H+ eq), Eutrophication, freshwater (kg P eq), Eutrophication, marine (kg N eq), Eutrophication, terrestrial (mol N eq), Ecotoxicity, freshwater (CTUe), Land use(Pt), Water use (m^3 depriv.), Ressource use, fossils (MJ) and Ressource use, minerals and metals (kg Sb eq).

For instance, two steps for manufacturing the bottom electrode on a substrate emits 53.2 kg CO2eq on climate change by photolithography without gold recycling and 8.7 kg CO2eq after recycling gold. In contrast, screen printing releases 7.3 kg CO2eq. Screen printing is significantly less environmentally damaging than photolithography for all indicators, unless gold is not recycled. Impacts can be decreased by a factor ranging from 4.7 to 10.9 using the screen-printing technique. If the gold is recycled, the two methods are comparable in terms of each impact factor. However, it is important to note that this study does not include all stages of photolithography.

Normalization and weighting factors that are normalized by the EF 3.1 method are used to rank the impact indicators according to their importance. The summation of these factors yields a single score. In both methods, the indicator of "resource use, minerals, and metals" accounts for more than 90 % of the calculated single score, which is presented in Fig 4.20. The use of resources, minerals, and metals is therefore responsible for the most significant ecological impact, resulting in depletion of resources.

If the gold on the target and equipment is not recycled, screen printing has significantly less impact
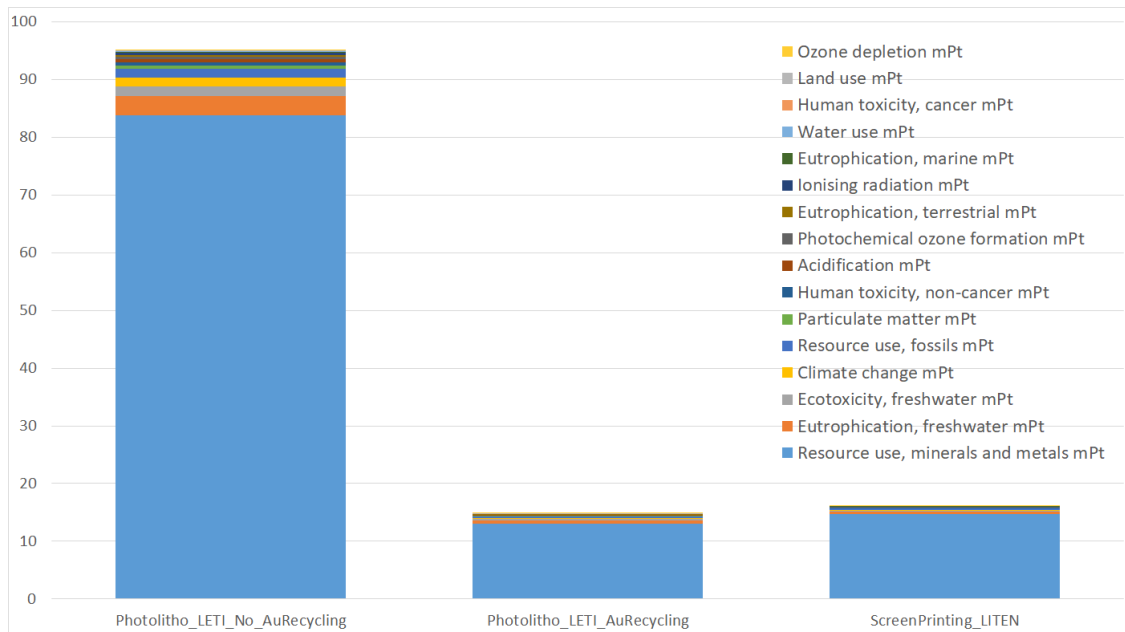
Figure 4.20: Single score for processes.

than photolithography in all categories. However, if the gold is recycled at the end of the equipment life cycle, the single score is equivalent. Despite the small amount of gold, specifically 0.169 g in the case of recycled overplated gold in comparison to 15.74 g of silver, the "Resource use, minerals, and metals" category remains equivalent. Indeed, 0.169 g of gold are equivalent to 0.011 kg Sb eq, while 15.74 g of silver are equivalent to 0.0124 kg Sb eq. Gold, in fact, has a noteworthy ecological effect.

SimaPro software can be used to identify the origin of the impacts by tracing the steps and materials utilized. For the two steps of photolithography studied, 100 % of the impact on this indicator is attributed to the metal deposition stage, with gold being the source of 100 % of the impact. Tungsten does not contribute to this impact. Returning to the topic of gold production, it is worth noting that 40 % of the impact originates from gold mining, while 21 % is from refining. The remaining impact is composed of several smaller impacts related to gold production after these two primary processes. When it comes to screen printing, 94 % of the impact results from silver mining. Thus this study identifies the extraction of gold and silver used for the bottom electrode as having the most significant impact. The impact of the procedures used is irrelevant.

To conclude this Life Cycle Assessment (LCA) indicates that the environmental impact of screen printing the bottom electrode with silver ink is equivalent to that of a gold deposition and etching step,

if the excess gold deposited in the PVD is recycled. It is important to note that additional steps are necessary for the photolithography process, as presented in Table 4.4. As a result, screen printing has a reduced impact on the environment and reduces the number of steps and production time. It has been observed that the electromechanical performance of haptic resonators produced using both techniques is similar. Therefore, it can be affirmed that screen-printing the bottom electrode with silver ink is the best option for future developments in this technology.

4.4.5 Future possibilities

In order to further reduce the environmental impact of the solution, other considerations are being taken into account.

Screen printing of the top electrode

The top electrode is obtained by direct evaporation in a vacuum of gold through a stencil, itself produced at CEA-Leti from a silicon substrate. In the same way, it takes a huge number of steps, and therefore resources and time, to deposit the gold layer on top of PZT ceramics. So it is worth asking if this step could be replaced with a silver ink screen printing step. The main disadvantage of screen-printing is the need to have a flat or near-flat surface in order to squeegee and spread the silver ink evenly over the wafer. When the surface is clean, there is no problem, as in the case of the bottom electrode step. However, in this situation, there is a certain topology present on the wafer due to the bottom electrode, the PZT ceramic, the glob top, and the various layers of adhesive. This surface topology encompasses height differences ranging from 0 μm to around 150 μm. A test is therefore carried out to see if screen printing is possible here. To do this, the screen-printing frame of the bottom electrode is taken and rotated by 180° to make the top electrode. It is not worth ordering a new screen-printing frame just to carry out a test. Alignment could therefore not be very precise, as shown in Fig. 4.21.

Nevertheless, this enabled us to validate the screen printing of the top electrode. SEM images, for example as on Fig. 4.22.a), show that the thickness of silver ink deposited varies between 8 and 12 μm. An impedance analyzer measurement also confirmed the electromechanical response and hence the resonance on Fig. 4.21.b).

In future developments, the screen-printing technique has the potential to produce both the bottom

Figure 4.21: Wafer with the top electrode screen-printed with a silver ink.

| a) | b) |
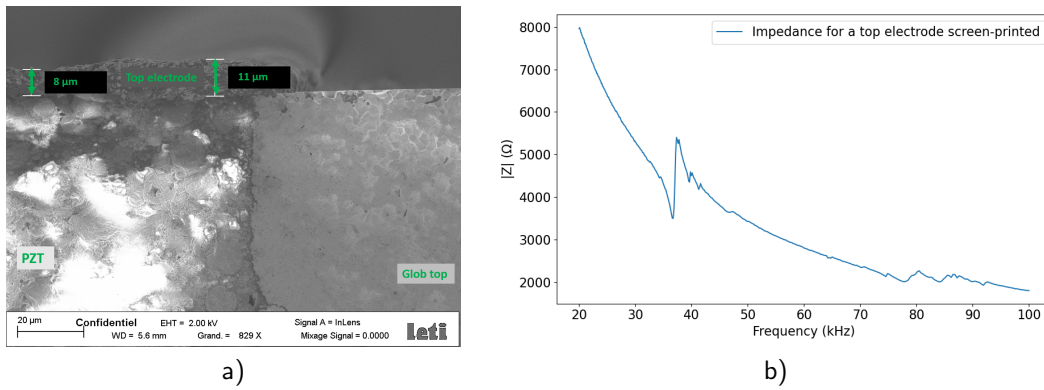
Figure 4.22: a) SEM cross-section and b) Impedance obtained for the top electrode in silver.

and top electrodes using silver ink. This would eliminate several fabrication steps and decrease the environmental impact of the technology.

Replacing the glass substrate with a silicon substrate

As explained in chapter 2, the vibrating plates were chosen to be made of glass, as they are traditionally used in microelectronics, particularly for touch screens. In addition, this suggested the possibility of a transparent solution. However, due to our technological choices, this transparency is not possible in the current state, since the polymer film used are not transparent, nor are PZT ceramics. Replacing the glass substrate with a non-transparent silicon substrate seems a viable solution. The mechanical characteristics of the two substrates are similar, except for the Young's modulus. The silicon substrate has a higher Young's modulus of around 140 GPa, compared to glass which has 73 GPa. This approach eliminates the need for glass opacification stages that are necessary for equipment to recognize plates and alignments. This process eliminates a number of steps, saving time and money and reducing

environmental impact. To produce haptic resonators from a 550 µm thick silicon substrate, a production batch was launched. One of the obtained resonators can be seen in Fig. 4.23.
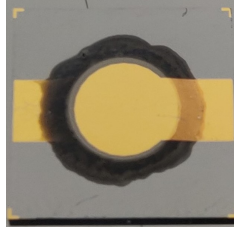
Figure 4.23: Resonator realized with a silicon substrate.

On Fig.4.24 a SEM cross view and the electromechanical validation using an impedance analyzer are plotted. As a result the resonance is around 46.9 kHz for this type of resonator.

a)   b)
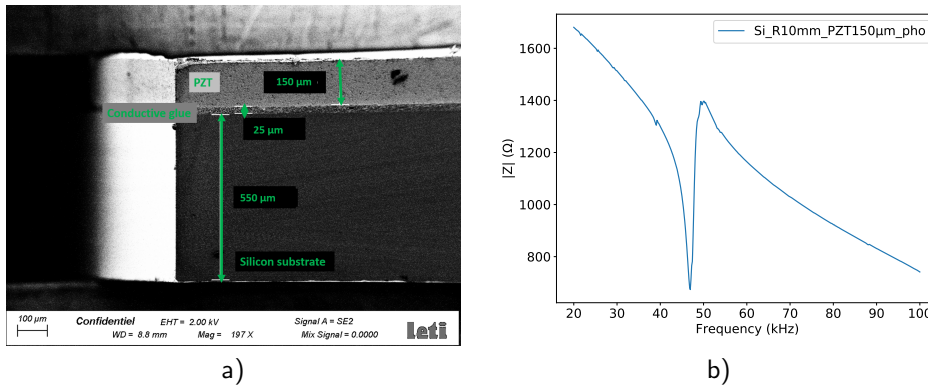
Figure 4.24: a) SEM cross-view and b) Impedance of the silicon resonator.

Other possibilities

Other potential improvements exist for reducing the ecological impact of this technology. One option is to use piezoelectric thin film technology that is based on PZT, which can minimize the amount of lead, a highly polluting substance. Another possibility is to substitute the PZT with a lead-free alternative material like AlN, ZnO, or KNN, for instance. The use of these materials may results in an ineffective haptic resonator due to their low piezoelectric coefficient, as shown in Table 2.1.

Replacing the KAPTON film with a bio-polymer can also be a solution to reduce the environmental impact of this technology. Nevertheless, a complete rethink of the manufacturing process will be necessary, as the polymer film is currently heated to 170°C.

4.4.6 Conclusion

A Life Cycle Assessment (LCA) study was conducted to compare two methods for creating the bottom electrode of the haptic resonator. Our findings confirm that the screen-printing method can significantly reduce the ecological impact of our technology. A more comprehensive study, including the entire process and life cycle of the technology, might be very interesting. Moreover some possibilities to reduce the ecological impact have been underlined and could be more investigated.

4.5 Electronic realization

Thus various interfaces have been produced using the manufacturing process. The aim is to use and test these surfaces. To do this, electronics are needed to control the surface, with the aim of providing haptic feedback.

In order to realize the electronics, we are asking whether an architecture with a completely different frequency and phase channel for each resonator on the surface is needed. To do this, we focus on the coupling and synchronization between resonators on the same surface.

4.5.1 Coupling and synchronization

As can be seen from measurements in 4.3.3, the resonators after bonding to the polymer film are not exactly identical due to manufacturing imperfections. In fact, each resonator has a slightly different natural frequency, but remains very close to the same frequency. However, thanks to the coupling between the resonators via the same polymer matrix, synchronization phenomena occur that allow the resonators to be locked at the same phase and frequency in certain cases. This phenomenon of synchronization has been theorized since Huygens in the 17th century with the discovery of the synchronization of two pendulum clocks [122]. In this section we will focus on the phenomenon of synchronization as applied to our coupled resonators.

Unidirectional synchronization

We take the case of two resonators, one active (A) and one passive (B).

109

If we apply a sinusoidal signal at resonance to resonator A a voltage is measured on the adjacent resonator B. The voltages of both resonators are plotted in Fig. 4.25. The actuation signal for resonator A is shown in blue, with an amplitude of 40 Vpp at 32 kHz. The captation signal for resonator B is shown in orange and is in phase with the actuation signal. This indicates that the second resonator oscillates at the same frequency and in phase with resonator A, demonstrating a unidirectional synchronization phenomenon [123]. Indeed, the coupling due to the flexible matrix causes resonator B to oscillate due to the surface wave. It oscillates at the frequency of resonator A. These oscillations are very weak, this is why we consider the resonator as passive. Thus, they cannot be detected by touch on the surface of the passive resonators. Furthermore, these displacements are not visible in the laser vibrometer measurements, as shown in Fig. 5.2.
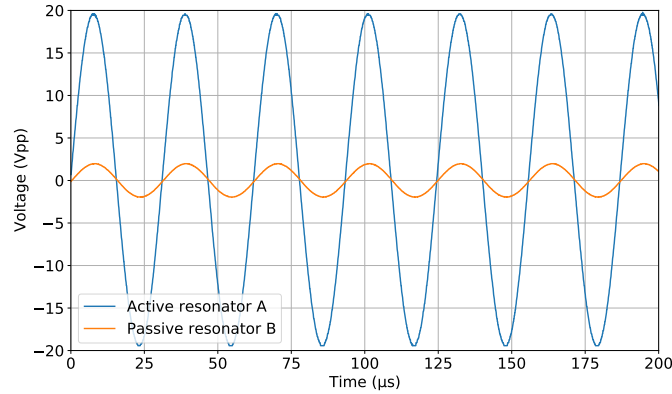
Figure 4.25: Actuation signal of resonator A and captation signal of resonator B.

This situation occurs because the frequencies of resonators A and B are close to each other. Synchronization would not be possible if the two frequencies were too far apart. This is theorized using the Adler equation 4.4, which allows the frequency range of synchronization between the two resonators to be defined as a function of the amplitude ϵ and pulsation ω of the actuation:

$$\frac{d\Delta\phi_s}{dt} = (\omega - \omega_0) + \epsilon q(\Delta\phi_s) \tag{4.4}$$

where $\Delta\phi_s = \phi_s - \omega t$ is the difference between the phases of the oscillations and of the forcing resonator

110

A. Function q is 2π periodic, and in the simplest case is sin. Thus there is a region $\Delta\Omega$:

$$\epsilon q_{min} < \Delta\Omega = \omega - \omega_0 < \epsilon q_{max} \tag{4.5}$$

where Eq. 4.4 has a stable stationary solution which exactly corresponds to phase locking, ϕ_s follows the phase of the forcing, i.e. $\phi_s = \omega t + cst$, and frequency entrainment, the observed frequency of the oscillator exactly coincides with the forcing frequency. This region is called the synchronization region, or Arnold tongue [124]. The multiple harmonics of ω_0 can also be used to create other synchronization regions. Fig. 4.26 shows drawings explaining the synchronization region.
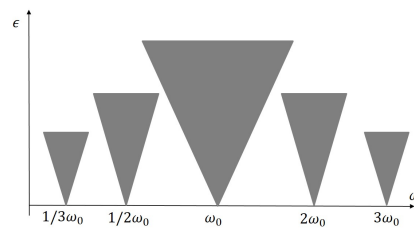
Figure 4.26: Zones of synchronization or Arnold tongue depending of the amplitude ϵ.

We now determine the frequency range $\Delta\Omega$. In this situation, the actuation signal of the active resonator A is varied at different frequencies around its resonance for a sinusoidal signal at 20 Vpp and we measure the impedance on the passive resonator B to determine if the resonator B synchronizes with the active one A. Fig. 4.27 shows the plot of the impedance for these different conditions.
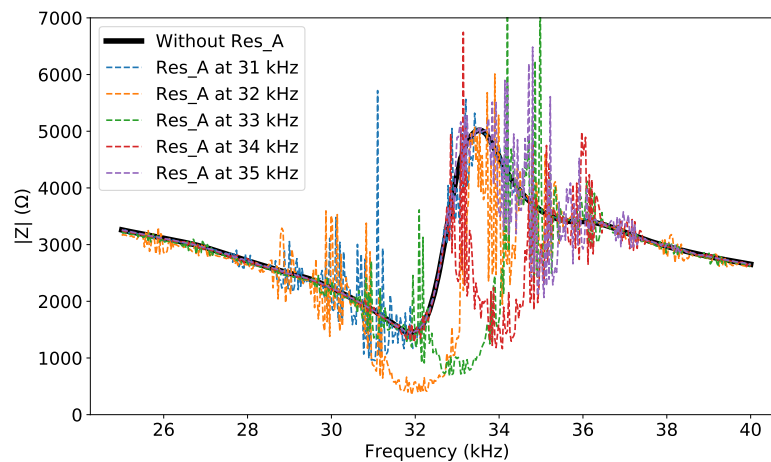
Figure 4.27: Impedance variation on B when an adjacent resonator A is actuated at different frequencies.

When resonator A is not activated, the impedance at the first mode of resonator B is the usual impedance. The resonance frequency is 31.9 kHz and the antiresonance is 33.5 kHz for this resonator. However, when resonator A is activated, the impedance becomes noisy due to the coupling of the two resonators through the polymer film. The coupling between resonator A and resonator B causes a shift in the resonance frequency of resonator B when resonator A is actuated with a 20 Vpp sinusoidal signal at a frequency between 32 kHz and 34 kHz. Resonator B synchronizes with resonator A. However, this synchronization is not effective when the actuation frequency of resonator A is too far from the initial resonance frequency of resonator B, such as at 31 kHz or 35 kHz in this plot. Thus, here the frequency range $\Delta\Omega$ for unidirectional synchronization is $[32:34]$ kHz at 20 Vpp.

This also allows us to prove that each resonator has a relatively wide operating range. This is due to the low quality factor discussed in 4.3.3. So each resonator can be operated over a wide frequency range. The resonance frequency disparity of $\pm$ 500 Hz, as seen in 4.3.3, is lower and is included in this actuation frequency range. It is therefore possible to actuate all the resonators at a single frequency, chosen as the average frequency of the resonant frequencies of the surface resonators as already done in Fig. 3.12 and in Fig. 3.19.

Mutual synchronization

In a more general case with at least two active oscillators, mutual synchronization phenomena appear. This is theorized by the Kuramoto model [125, 126, 127]. Here, we consider a weak coupling with N oscillators. Each oscillator has its own frequency, due to the disparity in the fabrication. However, these frequencies are very close to each other. Furthermore, each resonator is identically coupled to all the others.

In this way :

$$\frac{d\theta_k}{dt} = \omega_k + \frac{K}{N}\sum_{p=1}^{N} sin(\theta_p - \theta_k) \tag{4.6}$$

with N coupled phase oscillators, with phase θ_p and pulsation ω_p and a coupling factor K.

By redefining a parameter of order $re^{j\psi} = \frac{1}{N}\sum_{p=1}^{N}e^{j\theta_p}$, r for the phase coherence and ψ the mean phase and simplifying by considering the mean phase $\psi = 0$, we arrive at :

$$\frac{d\theta_k}{dt} = \omega_k - Kr\sin\theta_k \tag{4.7}$$

On Fig 4.28, we can find an example of phase synchronization following various order parameters. For the first one (a) the oscillators are not synchronized since there are incoherent. The more the order parameter increases the more the oscillators are locked. For r around 1 the oscillators are in phase. Since $sin(\theta_k) \leq 1$, we see that oscillators with natural frequencies $\omega_k \leq Kr$ can have a static

(a) $|r| = 0.18$ (b) $|r| = 0.44$ (c) $|r| = 0.91$ (d) $|r| = 0.99$
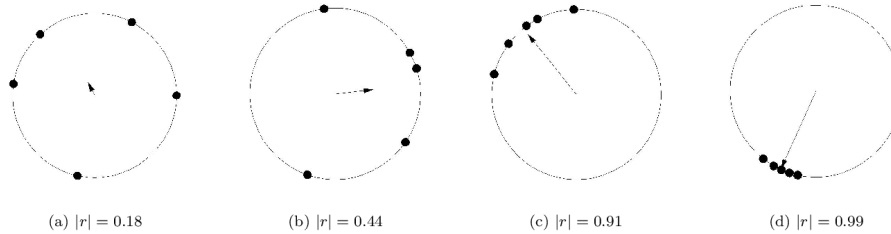
Figure 4.28: Evolution of the order parameter r. The length of the vector increases as the phases of the oscillators gets closer together [128].

solution $\dot{\theta}_k = 0$ when $\omega_k = Krsin(\theta_k)$. As a result, these resonators are frequency locked. In contrast, oscillators with a frequency of $\omega_k \geq Kr$ are not frequency locked and are not synchronized.

In our situation, resonators on the same surface are very close in frequency. Furthermore, the coupling is quite strong : as we saw in the previous sections, we can make a passive resonator oscillate with a neighboring active resonator that the same frequency and phase. Thus operating resonators at one frequency should force synchronization in frequency and phase, ensuring the desired outcome despite disparities in manufacturing.

Actuating all the resonators at the same frequency appears to be a good solution that simplifies the actuation electronics architecture. The option of introducing a phase shift between channels remains available to realign resonators if needed. The following section focuses on the electronic implementation.

4.5.2 Realization

Initially, the decision is taken to develop actuation electronics only. In fact, finger capture as part of a interface using friction reduction is not imperative. The electronics were developed with the help of Sébastien Brulais and Laure Peris Y Saborit from CEA-Leti / DSYS.

The actuation electronics is realized from a field-programmable gate array (FPGA) board and an amplification stage manufactured on a printed circuit board. The FPGA produces the digital drive signals [0;+3.3V] which can be for example connected from the USB port of a computer. Then two

field-effect transistors are mounted in push pull configuration and driven by a mosfet driver (IR2183), from the amplification stage as presented Fig. 4.29 for one PZT actuator. Thus, the signal generated by the FPGA board, is elevated from to 3.3 to 48 V. A DC generator is used to supply the amplification stage at 48 V.
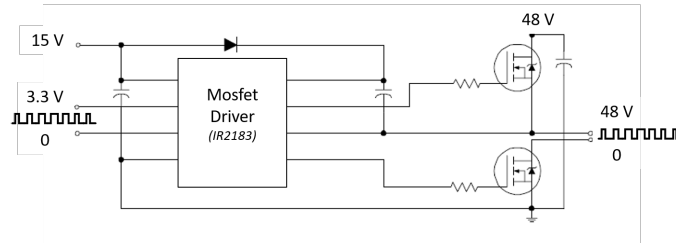
Figure 4.29: Amplification stage for one haptic resonator.

In this way, a pulse-width modulation (PWM) is produced on nine different channels to drive the nine piezoelectric actuators of the interface. The PWM allows to have an actuation signal at the resonance frequency of the resonators modulated at one frequency, for example 50 Hz or 250 Hz, by an amplitude modulation for haptic feeling. The carrier frequency (= the resonance frequency) and the modulation frequency are the same for each channel. A Python script enables to modify the voltage and the phase of the signal sent to each piezoelectric actuator.

4.5.3   Validation

To validate this electronic, measurements are done with a numerical oscilloscope and presented on Fig. 4.30. Here the actuation voltage is 20 Vpp at 32 kHz with a modulation at 250 Hz.
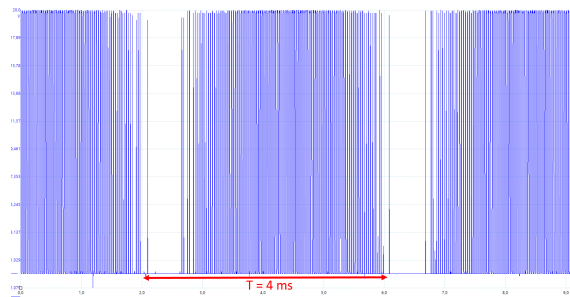
Figure 4.30: Operating voltage for one haptic resonator.

The period is 4 ms, i.e. the 250 Hz of the modulation. Additionally, examining the wave train's

center exposes a period of 31.2 µs between every spike which is the desired 32 kHz. The duty cycle, as expected, is 50 %.

Furthermore, a measurement was made to determine the current required for a haptic resonator without the polymer film. This is 12 mA for a voltage of 20 Vpp to 50 Vpp. This gives a maximum power consumption of 0.6 W per resonator. With the addition of the polymer film and the electronic tracks on it, which add a certain resistivity as seen above, the current required per resonator is between 14 mA and 17 mA for voltages from 20 Vpp to 50 Vpp, i.e. a maximum of 0.85 W per haptic resonator integrated into the final surface.

Fig. 4.31 shows the electronics as produced with a display base. An interface is mounted on a cylindrical 3D-printed support. Other surfaces on different supports are also shown. This set-up was presented during a demonstration session at the GDR Tact in Lille in June 2023, then at WorldHaptics23 in Delft in July 2023. The aim was to recognize elementary shapes drawn on the surface. A study on this subject will be presented in the next chapter 5.
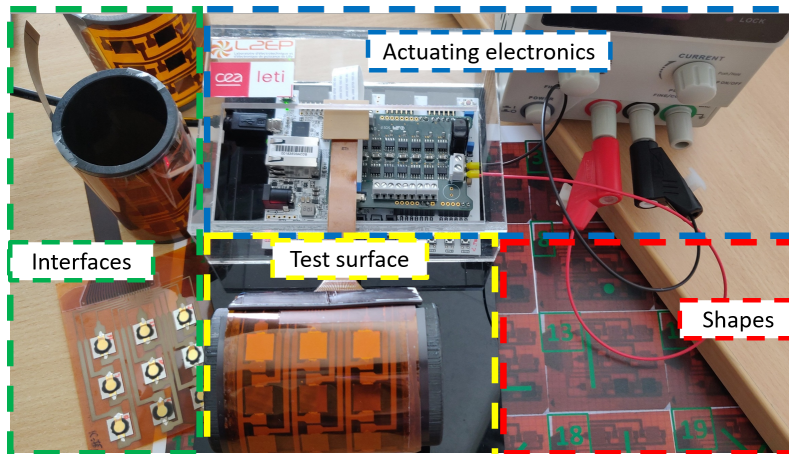
Figure 4.31: Interfaces with the actuating electronics.

4.5.4 Perspectives to improve the control of the surface

As explained this electronic is dedicated only to the actuation of the interface. To improve the system, an electronic device with vector control feedback as proposed in recent research [17] and finger captation on the surface will have to be developed.

As we have seen in 4.5.1 the resonance of the active resonator slightly excites a passive resonator.

Though insufficient to create sizable displacement, detection by the PZT ceramic allows it to function as a sensor. By calibrating the signal detected for each PZT ceramic, passive haptic resonators obtain specific signatures. By placing a finger on the surface, the passive resonator detects the signal and its PZT ceramic behavior changes, allowing us to track the position of the finger. Another technique could be to track the frequency of each resonator to obtain the position of the finger. Indeed the add of the finger is here equivalent to an add of mass and so the frequency is shifted to low frequency.

However, to achieve this, the electronics have to be completely redesigned.

4.6 Conclusion

In this chapter, we present the implementation of various interfaces using a specific process in the cleanroom facilities of CEA-Leti and CEA-Liten. The process entails two main steps : the production of square vibrating resonators and the creation of functional surfaces. Electrical characterizations validate the functionality of these devices. The resonators have been tested and confirmed to operate effectively at ultrasonic frequencies, while the surfaces of nine resonators have been shown to possess flexibility and functionality. Different configurations have been compared and validated from electrical measurements. Simultaneously, a LCA study was conducted to analyze the ecological impact of the technology. The scope of this research was limited to the production of the bottom electrode of the resonators. Two techniques were compared: a photolithography of a gold electrode and a screen printing of a silver electrode. This study confirms that screen-printing is less impactful on the environment while saving time and cost of fabrication. Additionally, its electrical performance is comparable to both techniques. Therefore, screen-printing is the optimal choice for future realizations. Further possibilities to reduce the ecological impact of this solution have also been identified. Finally, an actuation electronic has been developed based on an FPGA board, which enables the independent actuation of the nine resonators of the surface. Since the resonators on the same surface are very close in frequency and are coupled by the polymer film, we chose to drive them all at the same frequency. Only the phase of each channel can be parameterized. To further improve these electronics, various perspectives have been presented, including the addition of a vector control command and finger captation.

In this chapter, several demonstrators have been created. Consequently, the following chapter will evaluate the haptic capabilities of these new flexible interfaces based on localized friction reduction.

116

Chapter 5

Evaluation of the haptic capabilities of the surface

Contents

5.1 Introduction

This chapter aims to evaluate the haptic capabilities of our interfaces. Electromechanical measurements are performed to validate displacement amplitudes and vibration zones in 5.2. The influence of the finger on the surface is also studied. Tribological evaluations are performed in 5.3 to quantify the reduction in friction on localized areas or large continuous areas. Finally, two psychophysical studies are conducted in 5.4 to demonstrate two different use cases: the use of the interface in a shape recognition application and its use in a multi-touch or multi-user application.

In the following the interfaces used to validate the capabilities of this technology are the demon-

117

strators formed with the Kapton film of 75-µm and 10 mm x 10 mm resonators with a space of 10 mm between them.

5.2 Electromechanical evaluation

5.2.1 Localization of the vibrations

Cartographies have been done to confirm the behavior of the surface, formed with Kapton-75µm and 10 mm x 10 mm resonators with a space L_p of 10 mm, designed in chapter 3 and realized in chapter 4. For that purpose, the same setup as before is used with a Polytec OFV-5000 modular vibrometer and a sensor head OFV-505. The interface is mounted on a programmable and motorized 2-axis table (Makeblock) achieving programmable displacement with a resolution of 0.5 mm. The haptic resonators are driven by the same sinusoidal voltage at the resonance frequency and an amplitude peak to peak of 40 V. We use for that a specific ZIF connector and a breadboard as depicted in Fig. 5.1.
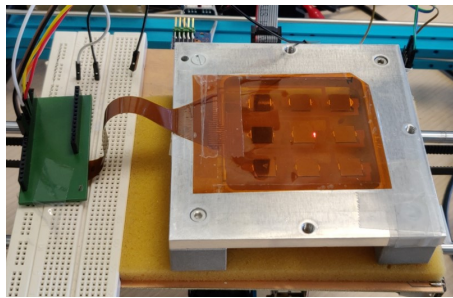
Figure 5.1: Set up for mapping measurements.

First, a single haptic resonator is activated at its resonant frequency as presented on Fig. 5.2.a). As expected by the model in chapter 3, the vibrations are localized around the haptic resonator. Due to the square geometry of the haptic resonator, there are four distinct parallel wavefronts and four spherical wavefronts. The passive resonator design ensures that only the four parallel wavefronts are reflected, allowing for precise localization of the vibration and resulting haptic feedback. The resonance is now at 32 kHz instead of 26 kHz, as explained in the previous chapter 4.

Shifting the resonant frequency from 26 kHz to 32 kHz results in a lower wavelength λ_p on the polymer, as seen in Fig. 3.2 and with formula 3.6. The wavelength should be lower, and in an optimal case it should be 2.6 mm. Thus, for 6 nodes of vibration, the optimum distance should be 8.5 mm and
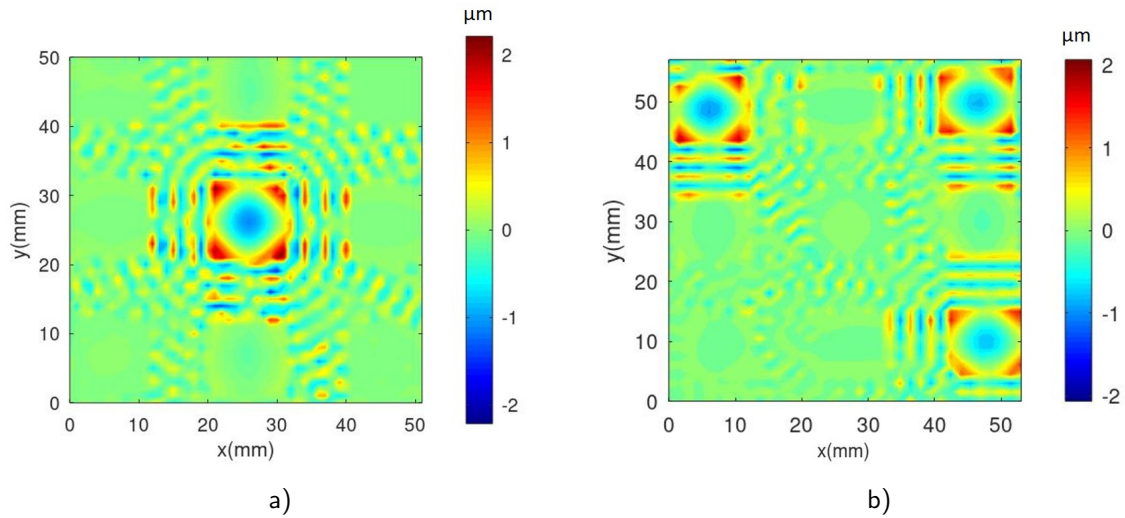
Figure 5.2: Displacements field for a) one actuated resonator and for b) three.

9.8 mm for 7 nodes according to the equation 3.11 i.e $L_p = \frac{\lambda_p}{2}(n + \frac{1}{2})$.

We can see that here, for $L_p = 10$ mm, we have exactly 6 vibration nodes, as observed in Fig. 5.2 and Fig. 5.3. As a result, the wavelength is 3.1 mm according to the equation 3.6. So there is a certain discrepancy between what we might have expected with the model and the experimental measurement. This can be explained by the fact that, on the Kapton film, the electrical tracks are made of silver paste. This adds 10 μm to the thickness h_p, but also increases the stiffness of the surface and thus increases the factor $\left(\frac{E_p}{\rho_p(1-\nu_p^2)}\right)^{1/4} h_p^{1/2}$ and thus λ_p. This was not present on the manual interfaces previously produced, nor taken into account in the model. As a result, the polymer film is stabilized in a 6-node vibration mode.
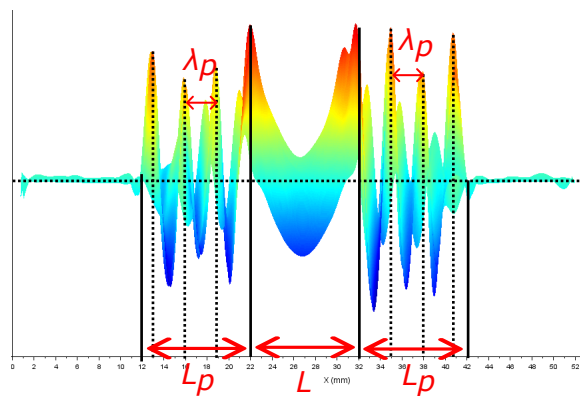
Figure 5.3: Transverse view : the central resonator active and the 2 others passive.

119

In order to characterize the maximal vibration amplitude that can be obtained on the device, punctual measurements were carried out at one corner of the central haptic resonator for several supplied voltage at resonance. The resulting curve depicted Fig. 5.4 exhibits a linear behavior ($y\ [\mu_{pp}] = 0.103\ x[V_{pp}]$, $R^2 = 0.995$) up to $V = 80$ Vpp as a consequence of the linearity of the piezoelectric effect of the piezoelectric actuators. A decrease in gain is then observed. The non-linearity of the resonator may be the cause of this problem. Increasing the voltage results in a slight frequency shift [129]. In this case, the frequency is kept constant, which could explain the nonlinear aspect and the decrease in gain.
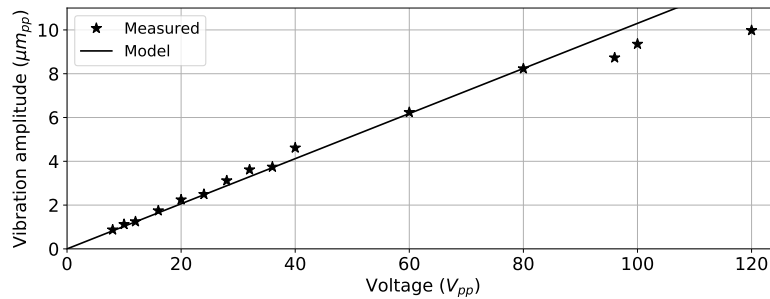
Figure 5.4: Amplitude of displacement at 32 kHz.

Then three resonators are activated at the same frequency. Fig. 5.2.b) shows the three distinct active zones. Thanks to the geometry of the surface, the vibrations are localized and strong enough to provide a haptic sensation. Moreover, the localization of these vibrations makes it possible to consider a multitouch use of this surface, in which case it would be possible to have three different sensations on the surface. Furthermore, despite the fact that the resonators have slightly different frequencies as shown in the previous chapter 4 due to manufacturing, activating them at the same frequency is not very problematic here. All three resonators have the same vibration amplitude and induce the same vibrations on the polymer film.

For a surface made from 75 μm thick KAPTON with 8 mm resonators, the frequency is 51.5 kHz as presented in chapter 4 above. A resonator is activated and the displacement amplitude and wave behavior are observed. The displacement amplitude on the active resonator is found to be the same as for interfaces with 10 mm resonators, which is expected. The distance between two resonators is now 12 mm, since the resonators are only 8 mm wide (actually 7.8 mm as previously observed). This results in a measured wavelength of 2.2 mm between two resonators using a laser vibrometer. The half-length

is therefore 1.1 mm, which is relatively small.

For the surface with 50 μm thick KAPTON and 10 mm resonators, no electromechanical differences were noted in chapter 4 with the same solution with 75 μm thick KAPTON. As a result, the same displacement amplitude is found on the resonators. Because of the thinner polymer film, we measure a wavelength of 2.3 mm or a half-wavelength of 1.15 mm.

For both situations, the half-wavelengths are very small. A half-wavelength of approximately 1 mm seems to be a lower limit considering the detection and discrimination thresholds under the finger, and especially the spatial resolution under the finger, which is about 1 mm. However, there are no studies to our knowledge that prove the existence of a lower wavelength limit, i.e. a high vibration frequency limit for ultrasonic lubrication. The lower limit of 20 kHz is well established, which enables us to determine the upper limit of the wavelength. However, the reverse is not explained in the current literature. Indeed Sednaoui et al. [61] prove that increasing the frequency enables to improve the friction reduction but this is at fixed $\lambda_p/2$ since they propose different haptic surfaces with the same $\lambda_p/2$ on each surface. In our scenario, the sensation obtained by friction modulation is easily detectable. Nevertheless, it would be valuable to explore the feedback obtained from a haptic resonator embedded in a polymer film at shorter wavelengths. This would allow a smaller resonator size, making it more suitable for various applications. We therefore validate these alternative designs. They are also suitable for the realization of flexible haptic interfaces with localized friction modulation. In the following we focus on interfaces with Kapton film of 75-μm and 10 mm x 10 mm resonators.

5.2.2 Continuity of the vibrations

We confirm now the possibility to create large haptic areas by combining haptic resonators. Two different shapes are presented on Fig. 5.5.

The displacements on the polymer and on the resonators are greater than 2 μm for 40 Vpp in both situations.

The first shape is a "L"-shape obtained by actuation of the top line and the right column. We clearly see that the passive resonators do not vibrate and will not produce any tactile feedback, confirming the simulation results in Fig. 3.17.a). This enables to have the "L" shape as wanted. For the second shape, the resonators are activated to reproduce an "X"-shape. Due to reflections between the passive
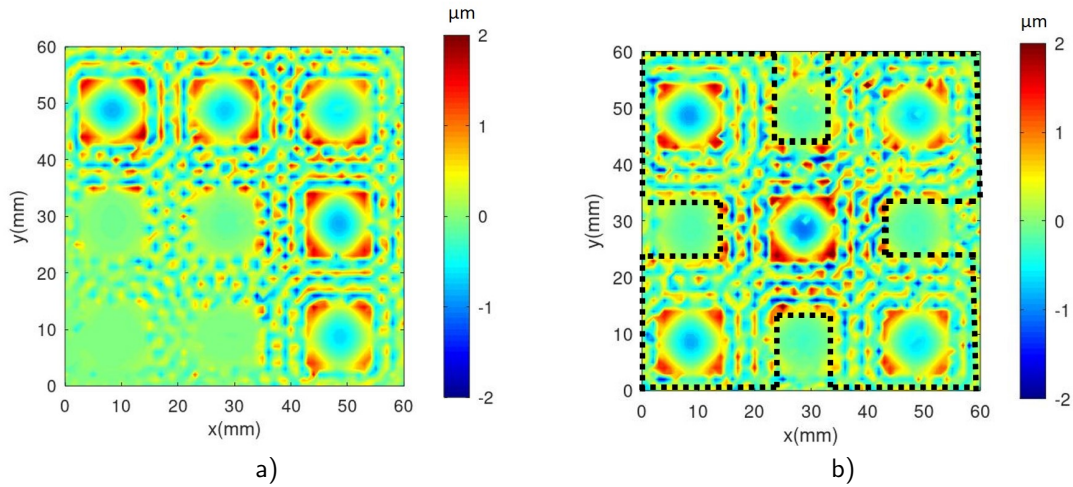
Figure 5.5: Displacement measurement on the surface: a) : activated L-shape; b): activated X-shape.

and active resonators, this shape is quite enlarged, as can be seen in the dotted line in Fig. 3.17.b). A shape recognition study will be following to see if this prevents to detect the "X" form.

5.2.3 Addition of a finger on the surface

Measurements are then taken to analyze the impact of the finger on the surface.

Impedance measurement

In fact, adding a finger to the surface is equivalent to adding a mass-spring-damper system to the surface [130, 131]. In Fig. 5.6 the model is shown with the finger in contact with the surface. The surface is also considered as a mass-spring-damper system, where m_s is the total mass of the surface, f_s and k_s are the equivalent damping and the equivalent stiffness of the surface. Thus, the impedance measured on a resonator will be the sum of the two impedances Z_f and Z_s when a finger is on the surface.

Several impedance measurements are taken on a surface resonator to observe the mechanical effect of the finger on the impedance. The impedance on the resonator changes depending on the finger's location on the interface because the surface is heterogeneous due to the periodic repetition of the resonators separated by a distance of L_p on the polymer film. Fig. 5.7.a) depicts the resonator where the impedance is measured and the finger's locations on the surface. In case A, the finger is on top
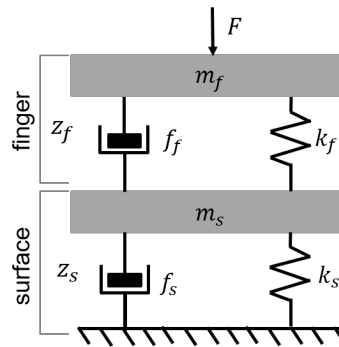
Figure 5.6: Model of the finger on the haptic surface.

of the measured resonator. In cases B, the finger is on top of the adjacent passive resonators, and in cases C, the finger is on the polymer film between resonators.

Fig. 5.7.b) shows the impedance modulus measured on the resonator in the various configurations.

a)   b)
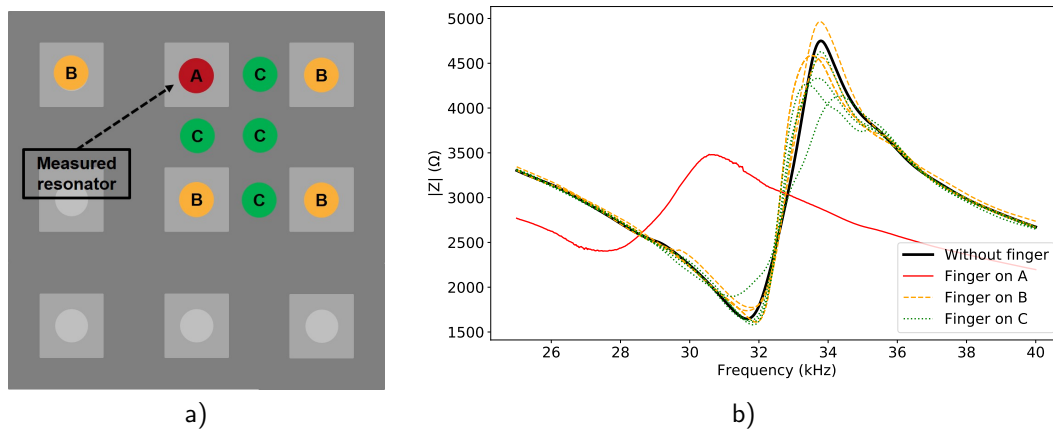
Figure 5.7: a) Drawing of the surface with the touch area; b) Impedance measurement for the different cases.

The impedance measured without the finger on the surface is the same as that measured in the previous chapter, with a resonance at approximately 32 kHz. However, when the finger is placed on top of the resonator, the frequency shifts to 27.5 kHz. This shift occurs because the mass of the finger affects the resonance frequency in a similar way to how the polymer film affected the resonance of the polymer-free resonator. Additionally, the finger strongly attenuates the mode, acting as a damper. The quality factor is reduced by more than 50 %. The impact of the finger on the resonator is significant in this case, as the finger remains static. However, in surface use cases where ultrasonic lubrication is

employed, the finger will be in a sliding condition, resulting in a less significant impact. As for cases B and C, where the finger is on adjacent resonators or on the polymer film between resonators, the impact on the active resonator is limited. The resonance and quality factor are slightly shifted and damped, respectively. However, these changes are negligible compared to the discrepancy caused by the manufacturing process.

Displacement measurement

Then displacement measurements are performed as follows. The central resonator is activated, and the laser is positioned to target an angle of the resonator. A force of 0.2 N, equivalent to a mass 20 g, is applied to the surface by a finger, as shown in Fig. 5.8.a).
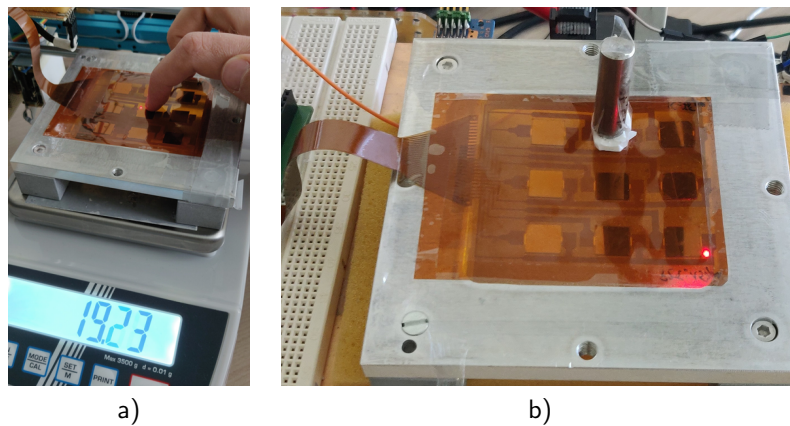
Figure 5.8: a) Set up for measurement with a finger and b) with a cylindrical mass.

When the finger is stationary at the center of the resonator, the measured displacements become negligible, effectively eliminating vibrations. Adding the finger to the center of the resonator, above the PZT ceramic, prevents vibrations. However, when the finger slides over the resonator and enters a dynamic condition, the vibration amplitude is reduced by half compared to the measurement without the additional mass shown in Fig. 5.4. This corresponds to a reduction of the quality factor by 2 due to the addition of the finger. In this way, the sensation is always present on the surface and around the active resonator. However, the finger damps the vibrations, so the voltage must be increased by a factor of 2 to obtain the same vibration amplitude on the surface.

The next step is to determine if the additional static mass affects the vibrations of the other resonators. The laser is used to produce two mappings, which are then compared. In both situations, a

line and a point are activated. The only difference between the two situations is the addition of a mass representing a finger in the static case. This mass is cylindrical, with a diameter of 1 cm and a weight of 20 g, representing an effort of 0.2 N on the surface. A piece of rubber is attached to the bottom of the cylindrical mass to add damping and approximate the mechanical behavior of a human finger. The assembly is attached to the central resonator of the active line, as presented in Fig. 5.8.b).

a)   b)
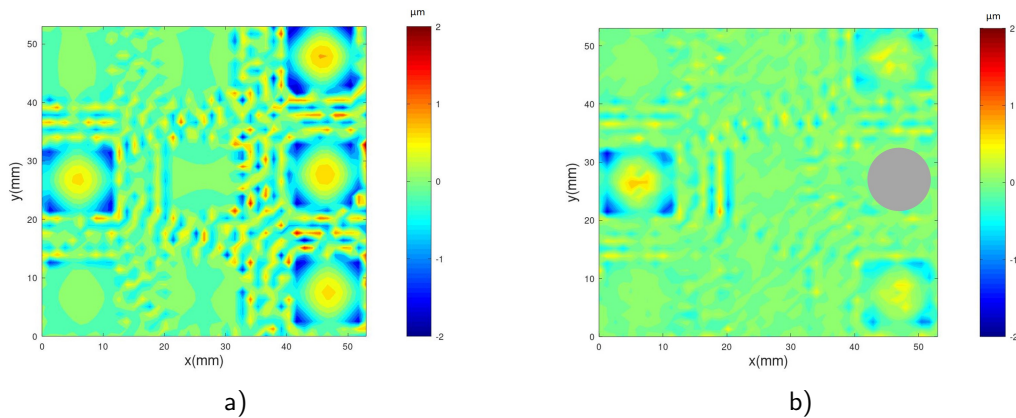
Figure 5.9: Surface displacement measurements : a) Without the mass; b) With the mass.

In the measurement without mass, Fig. 5.9.a), we obtain the two expected shapes: the line and the point. The displacements measured previously are in agreement with the current results, specifically 2 µm for 40 Vpp. When the mass is fixed, no displacement is measured on the resonator because it obstructs the laser, which is why a gray area is shown in Fig. 5.9.b). However, the amplitude of vibration on the other two resonators of the line was lower than before. Displacements are reduced by 50 % with maxima on the resonators at 1 µm compared to 2 µm without the mass symbolizing the static finger. Additionally, displacements on the polymer are nearly negligible. The resonance is shifted to a lower frequency due to the added mass, as shown in Fig. 5.7. Furthermore, the addition of mass deflects the surface due to the high flexibility of the polymer film, resulting in reduced efficiency of the laser measurement.

However, it is important to note that this measurement is made under static conditions, with the finger mass remaining fixed. Despite the damping effect of the finger, the displacements are compatible with the haptic effect obtained by ultrasonic lubrication. This measurement, nevertheless, highlights the importance of optimizing the control loop to adjust the resonator frequency according to the position of the finger on the surface.

As demonstrated in this section, haptic resonators create displacement amplitudes of over 2 μm at 20 Vpp at the surface for an ultrasonic frequency of 32 kHz. Localized areas or simple shapes can be programmed to provide haptic feedback by friction modulation.

The next section assesses the performance of the interface on the tribological point of view.

5.3 Tribological evaluation

In 2.5.1, we have verified the friction reduction on a single haptic resonator produced manually. We now aim to evaluate the localization and continuity of the friction reduction on the surface of nine resonators manufactured using the specific process detailed in chapter 4.

5.3.1 Validation of the friction reduction
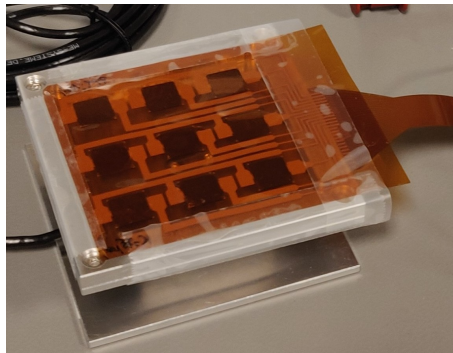
Figure 5.10: Set up for tribological measurements.

Tests are carried out in order to verify if our device can produce a localized friction reduction, and, contrary, if it is possible to have friction reduction over a whole line. For that purpose, we asked participants to explore the area of the haptic resonator by extending 10 mm to the left and to the right. We show on Figure 5.11 the friction coefficient μ over a line when the haptic resonator (B) in the center is supplied, and when the three haptic resonators are supplied to form a line (A+B+C). These are at 100 Vpp for one participant.

The figure shows that the friction decreases when the resonators are energized. When only the haptic resonator in the center (B) is supplied, the friction reduction is more important in the middle, than on top of the haptic resonators located at the extremity. Indeed, the vibration produced by the
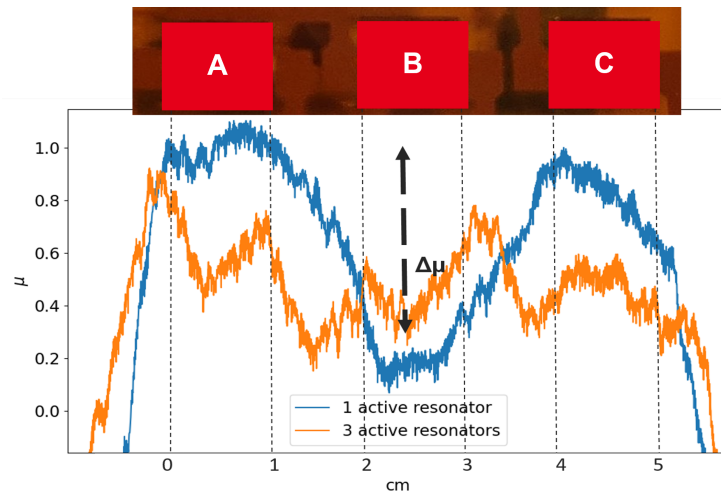
Figure 5.11: Comparison of the friction coefficient for one or three active haptic resonators.

active resonator is blocked by the non-energized ones, as described in our model in the chapter 3. When the three haptic resonators are supplied (A+B+C), the vibration is increased along the line. The friction reduction is not uniform however, maybe because the vibration amplitude is also not uniform over the line as shown Fig. 5.5. Indeed the amplitude of vibration on each resonator is slightly different, since they are not perfectly identical. But overall, the friction is reduced on the line, and the spaces between resonators contribute to its reduction, which shows that the interference are constructive and not destructive. The results presented above were obtained with a voltage whose amplitude is fixed. However, in the case where textures must be simulated, the voltage must be modulated. The more or less rapid variations in the vibration could then induce undesirable effects which would cancel the blocking effect of the resonators when they are not powered. This is why, the localization of the haptic feedback is now tested with a 5 Hz modulated voltage amplitude, and the results are presented Fig. 5.12.

Fig. 5.12 shows that the friction is modulated above the active resonator, and not above the passive ones. Hence, even in case of texture simulation, the haptic feedback can be localized, thanks to the discretization of the resonating surface.
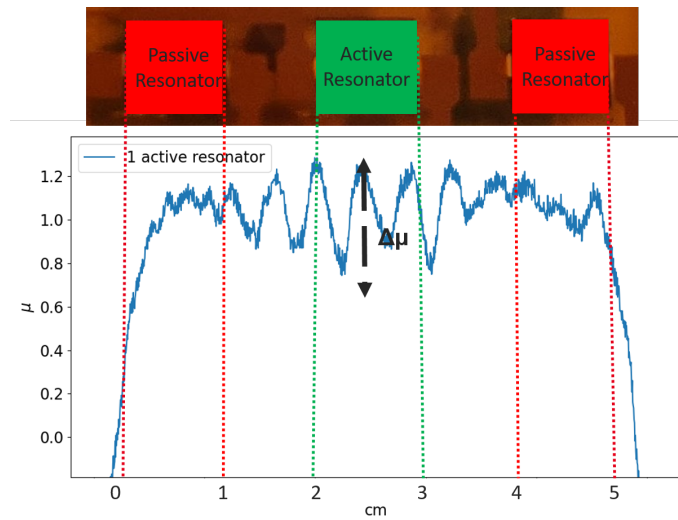
Figure 5.12: Variation in the coefficient of friction for an activated resonator.

5.3.2   Localization of the friction reduction

The friction coefficient is measured with 10 participants at different velocities conditions. They were asked to maintain a normal force of 0.2 N, and we tested a slow (15 mm/s) and fast (30 mm/s) sliding speed of the finger. A training session was organized for the participants to approximately maintain these velocity and normal force conditions. For each condition, the test is performed 7 times.

In a first experiment, the central haptic resonator is activated. The voltage amplitude V is varied between 20 Vpp and 140 Vpp, at resonance.

The mean relative friction coefficient, which is relative to the friction contrast $\Delta\mu/\mu_0$ and equal to $1 - \Delta\mu/\mu_0$, is then calculated for the complete area of 30 mm ie the active resonator and each side of it, and plotted as a function of the applied voltage for the two slide velocities. The standard deviation is also plotted on Fig. 5.13.

As expected, the relative friction coefficient between the sliding finger and the vibrating surface decreases as the applied voltage increases. This coefficient decreases until 0.7 at 140 Vpp for the two sliding velocities. Theses values match with the previous records done on a manually processed haptic resonator in 2.5.1.

Here we do not see the impact of the velocity on the friction velocity as we can see ordinary on friction reduction for classic rigid ultrasonic vibrating plate [61]. This can be due to the complexity of

128
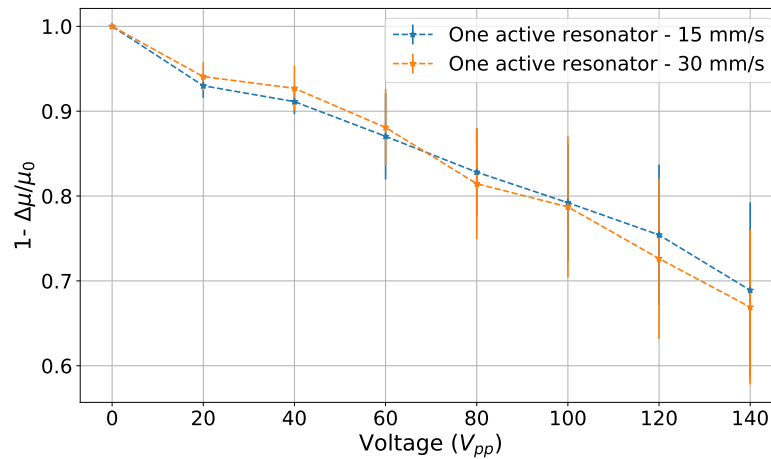
Figure 5.13: Friction reduction for one active resonator.

the multi-layer assembly of vibrating glass, epoxy adhesive and polymer film with stiffness changes of the surface.

We want now to test the continuity of the friction reduction on a larger area.

5.3.3 Continuity of the friction reduction

The same set up is used. During the test, one complete line of three resonators is activated by a sinusoidal voltage at the resonant frequency. Participants are asked to slide their finger on the line of 50 mm of length. Three different sliding velocities are tested: 17 mm/s, 25 mm/s and 50 mm/s. The same voltage set is used for these tests and the normal force apply is 0.2 N. For each voltage and slide velocity the test is performed 5 times.

We observe the same comportment that the previous measurement for one haptic resonator. The relative friction coefficient is decreasing again to 0.7 at 140 Vpp. Friction reduction is the same for a single resonator as for a complete line. This shows that the continuity of vibrations on the polymer provides continuity in friction reduction. Again the slide velocity seems to have no impact on the friction reduction.

In this section, we have validated and quantified the reduction of friction on our flexible haptic surface composed of nine resonators. We have also confirmed the localization and continuity of the friction modulation. This interface has the potential to create various textures simultaneously due to
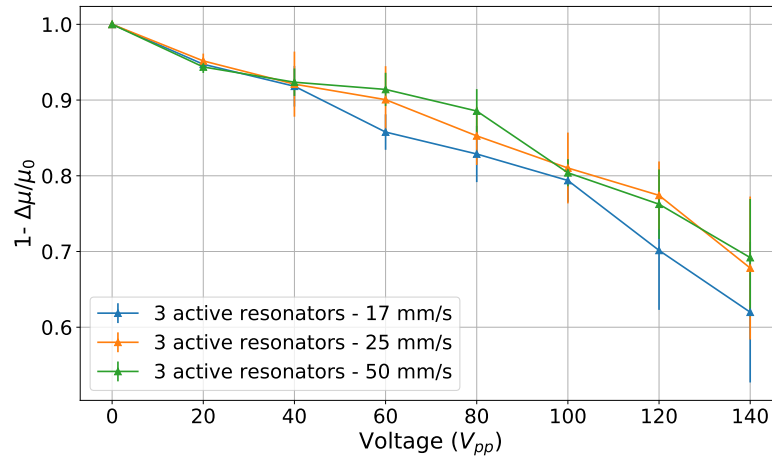
Figure 5.14: Friction reduction for a line of three active resonators.

its localization capability. This will be tested in the following section.

5.4 Psychophysical evaluation

In 2.5.2, we have confirmed the fact that users can detect different sensations around a manually-produced haptic resonator, depending on the signal of actuation. The objective is to validate a number of use cases on the interface of 9 resonators. The first use case involves detecting the local and large shape of the surface, for which a shape recognition study is conducted. The second use case involves testing the capacity to enable multitouch and multi-user interaction. For that, a multi-user study is conducted.

5.4.1 Shape recognition study

The objective of this study is to know whether the device can be used for tactile shape recognition. The study is conducted with the device curved, in order to prove the conformability of the surface.

Materials

The haptic interface is fixed on a cylindrical support with a diameter of 63 mm and placed on a stand to raise it. A breadboard, contactors and a ZIF connector are used to apply the voltage on the electronic tracks of the interface (Fig. 5.15). The breadboard is powered by a signal generator and a

130

voltage amplifier. By this way, the piezoelectric actuators are driven with a sinusoidal voltage with an amplitude of $V = 30$ Vpp, at the resonance. An amplitude modulation at 250 Hz is applied at this frequency, which corresponds to the lowest detection threshold for active touch [11].
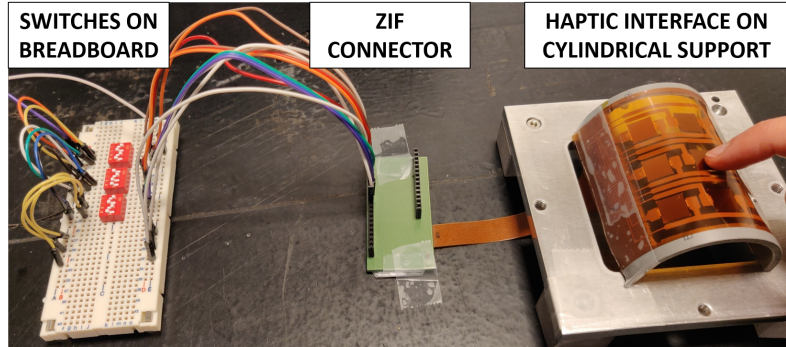
Figure 5.15: Set up for shape recognition study.

Protocol

12 inexperienced and consenting volunteers (3 women and 9 men) aged from 23 to 49 are participating in this study. 12 shapes, depicted Fig. 5.16, were selected. They represent elementary geometrical forms achievable with nine haptic resonators. They are made up of : a central point (n°2), three rows (n°3, n°4 and n°5), three columns (n°6, n°7 and n°8), two diagonals (n°9, n°10) and two more complex shapes which are the "+" (n° 11) and the "X" (n° 12). The shape n°1 contains no lit haptic resonator.

Each shape is presented 3 times for a total of 36 tests. Users are informed that 4 shapes are replayed to reach 40 tests, without knowing which ones. These are shapes n°1, n°2, n°4 and n°7. The goal is to prevent them from counting the number of times each shape is presented. The 40 tests are randomly drawn during the session.

Before the session, participants follow a training session in order to become familiar with the interface, and a shape is first presented. They then place their index finger on the device and a timer is started. After having freely explored the surface, participants announce aloud the detected shape. The timer is stopped. The response and the detection time are recorded in a file. Then, a new test is launched until the 40 ones are achieved. Two main data are analyzed. The first is the rate of correct answers and the second is the detection time which is necessary to recognize each shape by the participants.
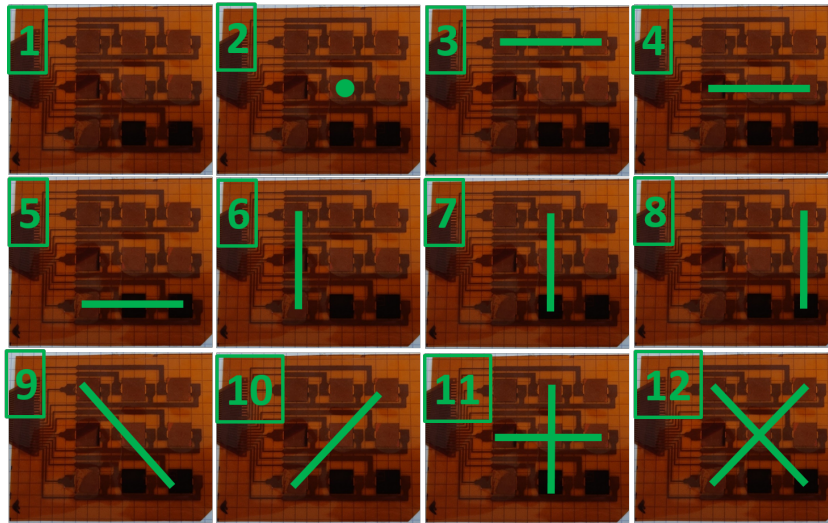
Figure 5.16: Shapes to recognize.

Results

The average score of shape detection with the device is 96.5 % across all shapes and all participants. The two best participants did not make any error for the 40 tests, while the worst participant perceived 92.5 % of the shapes which corresponds to only 3 wrong answers for the 40 tests. In general, the participants answered in 14.3 s.

To analyze and understand the origin of errors, we present on the table. 5.1 the confusion matrix for all shapes. The shapes 5, 6, 8, 9 and 10 were always detected by participants. However, the shapes 11 and 12 ("+" and "X" respectively) are the least identified.

Discussion

Interestingly, the results show that most of the time, a good detection ratio is obtained with the device, but some shapes are characterized by worse performances. This could be explained by the fact that shapes 11 and 12 merge two shapes (7 and 4 and 9 and 10 respectively). The experimental analysis of the Fig. 5.5.b) has shown that unwanted vibration of haptic resonators lead to the confusion with the shape 12.

If we analyze the average response time for each shape, we can see that the shapes for which the participants had the most errors also correspond to longest detection times. The shape 12 ("X") is

Table 5.1: Confusion matrix for the shape recognition study.

		Perceived by users												Total	Mean time for
		1	2	3	4	5	6	7	8	9	10	11	12	played	detection (s)
Played on the surface	1	100,0	0,0	0,0	0,0	0,0	0,0	0,0	0,0	0,0	0,0	0,0	0,0	48	12,8
	2	2,1	95,8	0,0	2,1	0,0	0,0	0,0	0,0	0,0	0,0	0,0	0,0	48	13,4
	3	2,8	0,0	94,4	0,0	0,0	0,0	0,0	0,0	0,0	0,0	2,8	0,0	36	16,8
	4	0,0	4,2	0,0	91,7	0,0	0,0	0,0	0,0	0,0	0,0	4,2	0,0	48	16,3
	5	0,0	0,0	0,0	0,0	100,0	0,0	0,0	0,0	0,0	0,0	0,0	0,0	36	12,7
	6	0,0	0,0	0,0	0,0	0,0	100,0	0,0	0,0	0,0	0,0	0,0	0,0	36	11,3
	7	0,0	2,1	0,0	2,1	0,0	0,0	95,8	0,0	0,0	0,0	0,0	0,0	48	13,8
	8	0,0	0,0	0,0	0,0	0,0	0,0	0,0	100,0	0,0	0,0	0,0	0,0	36	10,9
	9	0,0	0,0	0,0	0,0	0,0	0,0	0,0	0,0	100,0	0,0	0,0	0,0	36	13,9
	10	0,0	0,0	0,0	0,0	0,0	0,0	0,0	0,0	0,0	100,0	0,0	0,0	36	16,2
	11	0,0	0,0	0,0	2,8	0,0	0,0	5,6	0,0	0,0	0,0	91,7	0,0	36	13,9
	12	0,0	0,0	0,0	0,0	0,0	2,8	0,0	5,6	0,0	0,0	2,8	88,9	36	19,8
														480	14,3

the one for which the participants took the longest time to answer, 19.8 s; this confirms the difficulty of the participants to detect this form. Conversely, the shapes with 100 % recognition, such as shapes n°5, n°6 and n°8, are the fastest to be detected.

If we now draw the average response time of each participant in Fig. 5.17, we can see that the participants with the highest error rate are those who also took the longest time to answer (participants 3 and 12 for instance). Conversely, participants who made a maximum of 1 wrong answer (participants 1, 4, 6, 8, 10 and 11) responded the fastest.
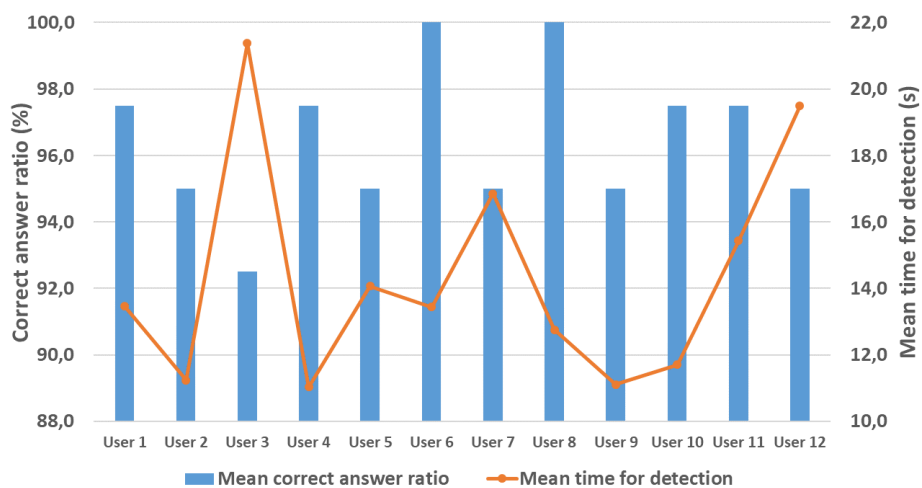
Figure 5.17: Correct answer ratio and mean time for detection by users.

The high recognition rate found in the study shows that our haptic interface allows to display programmable shapes in a conformable and flexible interface.

Giving the interface the shape of a cylinder with a diameter similar to that of a bracelet does not seem to have hindered the haptic performances of the interface. The feeling is very clear, only some rather sophisticated shapes pose a problem and appear confusing. Increased performances may require to improve the vibration pattern of the interface, and in particular, to avoid the unwanted vibration between non activated haptic resonators. For example, voltage control of the piezoelectric actuator could improve the accuracy of the generated shapes. The detection time however is around 14 s which is acceptable for one shape detection, but needs to be decreased if we want to present a sequence of shapes. The fact that we did not impose a time limit for detection does not work in our favor. The participants took their time to ensure that their answers were as accurate as possible. Furthermore it is also possible to increase the voltage to obtain a reduced detection time. Here, the rather low voltage of 30 Vpp corresponds to the voltage that was found to allow a 92 % rate of good responses at 250 Hz in our study of the detectability of haptic resonators in 2.5.2. Thus, by increasing this voltage, we increase the detectability rate of the resonators and thus, for this study, reduce the detection time. These low voltages have added an additional difficulty for the participants to detect shapes. In a real case of guidance use, the voltage would be increased to reduce the detection time.

5.4.2 Multi-user study

A two-user study is then carried out. The purpose here is to validate the multitouch and multi-user character of the proposed solution.

Materials

Two successive lines of three haptic resonators are used: the blue line on the left and the orange line on the right on Fig. 5.18.a). Four different haptic feedbacks were programmed: an amplitude modulation of the 31.8 kHz sinusoidal actuation signal at 30 Vpp applied to the haptic resonators at 50 Hz (A), at 250 Hz (B), or at 500 Hz (C), and no actuation at all (O). The surface is fixed to a flat, non-cylindrical support to facilitate two-person interaction.
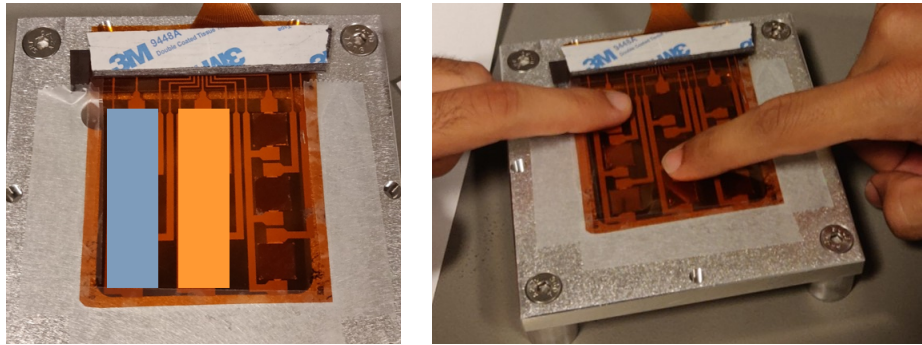
Figure 5.18: a) Surface with the 2 lines; b) Surface with 2 users.

Protocol

14 consenting, inexperienced people (3 women and 11 men) forming 7 pairs took part in the study. They range in age from 23 to 55. Each participant is stimulated with the following distribution of haptic feedback: $4 \times A + 4 \times B + 4 \times C + 3 \times 0$. This distribution was unknown to the users, and random draws are made before the test begins. During each test, the haptic feedback is different for each participant in a pair, who has 5 seconds to sweep the finger on his/her line, and announce on a sheet of paper which haptic feedback was presented. A training session is carried out before the test in order to differentiate each haptic feedback.

Results

The rate of correct answers for all users is 89.05 %. The participants in line 1 had a slightly better response rate at 89.52 %, compared with 88.57 % for the others. These excellent results demonstrate that users are able to differentiate tactile information while exploring the surface simultaneously. The table 5.2 shows participants' answers for each test and for each line.

The table 5.2 shows confusions, mainly between the stimuli B and C which are the most frequently changed in the responses. Interestingly, when no stimuli is programmed for a participant, while the other is stimulated with a haptic feedback A, B or C, the detection rate is almost 100 % in every case, except when stimuli B is programmed on line 2. For this last condition the success rate is 71.4 %.

Table 5.2: Participants answers for each test and each line.

Test number	Feeling played on the left line	Feeling perceived by users on the left line (in %)				Feeling played on the right line	Feeling perceived by users on the right line (in %)			
		0	A	B	C		0	A	B	C
1	B	0,0	0,0	100,0	0,0	A	0,0	71,4	28,6	0,0
2	A	0,0	100,0	0,0	0,0	0	100,0	0,0	0,0	0,0
3	B	0,0	0,0	42,9	57,1	C	0,0	0,0	28,6	71,4
4	0	71,4	0,0	0,0	28,6	B	0,0	0,0	100,0	0,0
5	C	0,0	0,0	14,3	85,7	B	0,0	0,0	100,0	0,0
6	A	14,3	85,7	0,0	0,0	C	0,0	0,0	14,3	85,7
7	0	100,0	0,0	0,0	0,0	A	0,0	100,0	0,0	0,0
8	B	0,0	0,0	85,7	14,3	C	0,0	0,0	14,3	85,7
9	C	0,0	0,0	0,0	100,0	0	100,0	0,0	0,0	0,0
10	0	100,0	0,0	0,0	0,0	B	14,3	14,3	57,1	14,3
11	B	0,0	0,0	85,7	14,3	A	0,0	85,7	14,3	0,0
12	A	14,3	85,7	0,0	0,0	0	100,0	0,0	0,0	0,0
13	C	0,0	0,0	0,0	100,0	B	0,0	0,0	85,7	14,3
14	A	0,0	100,0	0,0	0,0	C	0,0	0,0	0,0	100,0
15	C	0,0	0,0	0,0	100,0	A	14,3	85,7	0,0	0,0

Discussion

The results show that the sensation felt by a user is independent of the stimulation provided to the other. Hence, it is possible to play different haptic patterns simultaneously for each user. Therefore, we demonstrate that the device can produce localized stimuli, allowing several users to interact simultaneously on the interface.

This validates the multitouch and multi-users nature of the solution.

5.5 Conclusion

This chapter validates the developed and produced interfaces and demonstrates localized or extended zones of vibration continuity on the polymer film. The haptic resonators achieve displacements of 4 μm_{pp} at a voltage of 40 Vpp at resonance. When a finger is added to the surface, these amplitudes are reduced due to attenuation and resonance offset, but the sensation is not prevented. Tribological evaluations are then conducted to validate the friction reduction on the haptic surface. As a result, friction modulation can be felt in the desired zones and is also present between the resonators. Two psychophysical studies were conducted to evaluate the 9-resonator haptic surface. The first study demonstrated that users could distinguish vibration zones and recognize shapes drawn on the surface. The correct response rate was 96.5 % with a detection time of 14 seconds when a voltage of 30 Vpp was used. Increasing the actuation voltage and making the study more restrictive could improve the

detection time. The second study showed that the surface has multitouch and multi-user capabilities. In a study, two users touched the surface at the same time and announced the feel they thought they had touched. In 89 % of cases, users correctly recognized their own sensation. The study also found that users did not feel their neighbor's sensation, which validates the fact that multiple sensations can be felt simultaneously on the surface. This flexible haptic interface enables multitouch and multi-user feedback, making it the first flexible haptic surface with localized friction modulation.

Conclusion and Perspectives

Haptic surfaces have been developed for many years with the aim of improving human-machine interaction. Simple vibration to texture reproduction can be experienced on tactile screens. However, these solutions require a simple geometry and a rigid material to be effective. At the same time flexible and conformable technologies, such as foldable phones and wearable technologies, are now emerging on the market. Currently, researchers are developing haptic solutions that are flexible and conformable to all surfaces. However, these solutions are not able to achieve advanced sensations such as texture effects. Therefore, this thesis aims to develop a new concept of flexible haptic interface with localized or continuous feedback using friction modulation.

Based on a review of the state of the art and considering the advantages and disadvantages of current haptic technologies, whether rigid or flexible and conformable the proposed solution was introduced in chapter 1. This solution is an innovative hybrid haptic interface that combines the benefits of small-sized haptic resonators with ultrasonic lubrication and a flexible polymer matrix, ensuring the overall flexibility of the system.

In Chapter 2, the primary focus was on the development and validation of the fundamental concept of a haptic resonator incorporating integrated ultrasonic lubrication within a flexible matrix. This chapter involved the design of two resonators, optimized using the theory of vibrating plates and accounting for various assumptions and constraints related to frequency, wavelength, and resonator size. Two distinct resonators emerged from this process: a rectangular resonator based on a Lamb A0 mode and a square resonator based on a (2,0+0,2) mode. Piezoelectric actuators were selected to align with each mode's requirements. Electromechanical validation confirmed the viability of both designs.

Following this, the square resonator was chosen as the foundational element for the haptic surface. A subsequent exploration of different polymers resulted in the selection of a 100 μm PEEK film and a 75 μm KAPTON film as the flexible matrix. Electromechanical measurements were conducted to confirm surface displacements exceeding 1 μm when subjected to a sinusoidal signal of 20 Vpp at the resonance frequency. Additionally, a tribological study confirmed the friction reduction between the finger and the vibrating surface. The implementation of haptic resonators was further validated through a psychophysical study, where users successfully detected the resonators in 92 % of cases when subjected to a 30 Vpp actuation signal at resonance, modulated at 250 Hz.

In Chapter 3, the elementary resonator served as the basis for designing a surface composed of 9 haptic resonators. This periodic surface was intricately detailed through the analysis of the flexion wave generated by the haptic resonators on the polymer film's surface. The distance between two resonators was optimized based on clamped-free beam model to maximize displacement. The surface of 3 x 3 resonators was segmented to highlight the displacement field at the matrix surface during resonance, generating local and large-area vibrations. Electromechanical measurements were conducted to validate these findings, confirming vibration amplitudes greater than 1 μm at a low voltage of 20 Vpp at the resonance frequency. Finally, this chapter highlights the flexibility of the haptic surface. In a 1D model, the haptic surface has a flexibility similar to that of a homogeneous beam of PEEK film with a thickness between 730 and 1086 μm under a unit load. In addition, the proposed haptic surface can conform to small radii of curvature, such as a human wrist, without degrading the electromechanical performance of the resonators.

Chapter 4 focused on producing various demonstrators based on the designs introduced in earlier chapters. The fabrication of the haptic interfaces took place through a specific process, using the 8 inch industrial tools in the cleanrooms of CEA-Leti and CEA-Liten. This innovative process was divided into two main stages: the production of vibrating resonators and the functionalization of the polymer film. Electrical characterizations were performed to validate the fabrication of resonators and surfaces for different configurations. Simultaneously, a life cycle assessment (LCA) was conducted to assess the environmental impact of this technology. The study, limited to the production of the bottom electrode of the resonators, compared two techniques: photolithography of a gold electrode and screen printing of a silver electrode. The findings confirmed that screen printing is more environmentally friendly, time-saving, and cost-effective. Additionally, its electrical performance is comparable to both techniques,

making screen printing the optimal choice for future implementations. Further opportunities to minimize the ecological impact of this solution were also identified. An actuation electronics based on a FPGA board was then developed to allow the independent actuation of the nine resonators on the surface. Various perspectives were discussed for enhancing this electronic, including the incorporation of vector control commands and finger detection.

Finally, in Chapter 5, the potential for obtaining localized or continuous haptic sensations on the surface was demonstrated. The haptic resonators achieved displacements of 4 μm_{pp} at a voltage of 40 Vpp at resonance. Although the addition of a finger to the surface reduced these amplitudes due to attenuation and resonance offset, it did not prevent the sensation. Tribological evaluations were then performed to reduce friction on the haptic resonators, resulting in noticeable friction modulation in the desired zones and between the resonators. Two psychophysical studies were conducted to assess the 9-resonator haptic surface. The first study demonstrated that users could distinguish vibration zones and recognize shapes drawn on the surface, achieving a correct response rate of 96.5 % with a detection time of 14 seconds at a voltage of 30 Vpp. Increasing the actuation voltage and refining the study parameters could improve detection time. The second study revealed the multitouch and multi-user capabilities of the surface. In a two-user scenario, users correctly identified their own sensation in 89 % of cases, confirming that multiple sensations can be felt simultaneously on the surface.

In conclusion, this work has successfully pioneered the development of the first flexible haptic solution capable of providing localized or continuous feedback through friction modulation, enabling multitouch and multi-user use cases. This solution holds applicability in various scenarios where surface flexibility and conformability are essential. Examples mentioned in the thesis include applications such as a haptic bracelet, wearable technologies, and larger surfaces like car dashboards. Each of these diverse use cases and applications would require a unique design process, considering distinct assumptions, constraints, and objectives. However, the underlying operating principle of the technology remains consistent. For example, the size of the haptic resonator could be further reduced by adjusting its manufacturing technique with thinned substrates and thin PZT layer solutions, facilitating integration into wearable systems. Conversely, the resonator could be enlarged to accommodate more substantial vibrations and be integrated into a thicker matrix, such as a car dashboard. Therefore, improvements to this technology could include adding finger sensing through the use of piezoelectric sensors or capacitive layers, implementing closed-loop electronics for better control of the resonators and a wider range of

activation signals, and modifying the manufacturing process to reduce the environmental footprint of the solution.

The potential applications of this novel haptic technology are vast, promising improvements in human-machine interactions by replicating textured sensations on flexible and conformable surfaces. This versatility opens up numerous perspectives for further advancements and innovations in the field.

References

[1] S. J. Lederman and R. L. Klatzky, "Hand movements: A window into haptic object recognition," *Cognitive Psychology*, vol. 19, no. 3, pp. 342–368, 1987.

[2] C. Basdogan, F. Giraud, *et al.*, "A review of surface haptics: Enabling tactile effects on touch surfaces," *IEEE Transactions on Haptics*, vol. 13, no. 3, pp. 450–470, 2020.

[3] L. Pantera and C. Hudin, "Multitouch Vibrotactile Feedback on a Tactile Screen by the Inverse Filter Technique: Vibration Amplitude and Spatial Resolution," *IEEE Transactions on Haptics*, vol. 13, pp. 493–503, July 2020.

[4] C. Hudin, J. Lozada, and V. Hayward, "Localized tactile stimulation by time-reversal of flexural waves: Case study with a thin sheet of glass," in *2013 World Haptics Conference (WHC)*, (Daejeon), pp. 67–72, IEEE, Apr. 2013.

[5] A. B. Dhiab and C. Hudin, "Confinement of Vibrotactile Stimuli in Narrow Plates: Principle and Effect of Finger Loading," *IEEE Transactions on Haptics*, vol. 13, pp. 471–482, July 2020.

[6] M. Biet, F. Giraud, and B. Lemaire-Semail, "Squeeze film effect for the design of an ultrasonic tactile plate," *IEEE Transactions on Ultrasonics, Ferroelectrics and Frequency Control*, vol. 54, pp. 2678–2688, Dec. 2007. Number: 12.

[7] D. Corzo, G. Tostado-Blázquez, and D. Baran, "Flexible Electronics: Status, Challenges and Opportunities," *Frontiers in Electronics*, vol. 1, p. 594003, Sept. 2020.

[8] C. Pacchierotti, S. Sinclair, M. Solazzi, A. Frisoli, V. Hayward, and D. Prattichizzo, "Wearable Haptic Systems for the Fingertip and the Hand: Taxonomy, Review, and Perspectives," *IEEE Transactions on Haptics*, vol. 10, pp. 580–600, Oct. 2017.

[9] J. Yin, R. Hinchet, H. Shea, and C. Majidi, "Wearable Soft Technologies for Haptic Sensing and Feedback," *Advanced Functional Materials*, p. 2007428, Dec. 2020.

[10] F. Casset, J. S. Danel, C. Chappaz, Y. Civet, M. Amberg, M. Gorisse, C. Dieppedale, G. Le Rhun, S. Basrour, P. Renaux, E. Defay, A. Devos, B. Semail, P. Ancey, and S. Fanget, "Low voltage actuated plate for haptic applications with PZT thin-film," in *2013 Transducers & Eurosensors XXVII: The 17th International Conference on Solid-State Sensors, Actuators and Microsystems (TRANSDUCERS & EUROSENSORS XXVII)*, (Barcelona, Spain), pp. 2733–2736, IEEE, June 2013.

[11] S. J. Bolanowski, G. A. Gescheider, R. T. Verrillo, and C. M. Checkosky, "Four channels mediate the mechanical aspects of touch," *The Journal of the Acoustical Society of America*, vol. 84, pp. 1680–1694, Nov. 1988.

[12] Y. Lee, J. Park, A. Choe, S. Cho, J. Kim, and H. Ko, "Mimicking Human and Biological Skins for Multifunctional Skin Electronics," *Advanced Functional Materials*, vol. 30, p. 1904523, Aug. 2019.

[13] A. Vallbo and R. Johansson, "Properties of cutaneous mechanoreceptors in the human hand related to touch sensation," *Human Neurobiology*, vol. 3, no. 1, p. 3 – 14, 1984.

[14] K. O. Johnson, "The roles and functions of cutaneous mechanoreceptors," *Current Opinion in Neurobiology*, vol. 11, no. 4, pp. 455–461, 2001.

[15] S. J. Lederman and R. L. Klatzky, "Haptic perception: A tutorial," *Attention, Perception & Psychophysics*, vol. 71, pp. 1439–1459, Oct. 2009.

[16] L. A. Jones and S. J. Lederman, *Human hand function*. Oxford ; New York: Oxford University Press, 2006. OCLC: ocm60798472.

[17] A. Kaci, *Méthodologie de commande de vibrations multimodales par modulation-démodulation synchrone : application au retour tactile "multi-touch"*. PhD thesis, Université des Sciences et Technologies de Lille, 2020.

[18] I. El Rassi and J.-M. El Rassi, "A review of haptic feedback in tele-operated robotic surgery," *Journal of Medical Engineering & Technology*, vol. 44, pp. 247–254, July 2020. Publisher: Taylor & Francis.

[19] D. Borro, J. Savall, A. Amundarain, J. Gil., A. Garía-Alonso, and L. Matey, "A large haptic device for aircraft engine maintainability," *IEEE Computer Graphics and Applications*, vol. 24, no. 6, pp. 70–74, 2004.

[20] J. Perret, C. Kneschke, J. Vance, and G. Dumont, "Interactive assembly simulation with haptic feedback," *Assembly Automation*, vol. 33, no. 3, pp. 214–220, 2013.

[21] Phantom, "Phantom premium." `https://fr.3dsystems.com/haptics-devices/3d-systems-phantom-premium`.

[22] Butterfly Haptics. `https://butterflyhaptics.com/`.

[23] P. Culmer, A. Alazmani, F. Mushtaq, W. Cross, and D. Jayne, "15 - Haptics in Surgical Robots," pp. 239–263, Jan. 2020.

[24] D. Wang, Y. Guo, S. Liu, Y. Zhang, W. Xu, and J. Xiao, "Haptic display for virtual reality: progress and challenges," *Virtual Reality & Intelligent Hardware*, vol. 1, pp. 136–162, Apr. 2019.

[25] Teslsuit. `https://teslasuit.io/products/teslasuit-4/`.

[26] bHaptics. `https://www.bhaptics.com/`.

[27] Skinetic Actronika. `https://www.skinetic.actronika.com/`.

[28] Cyberglove. `http://www.cyberglovesystems.com/`.

[29] Haptx. `https://haptx.com/`.

[30] Razer. `https://www.razer.com/fr-fr/technology/razer-hypersense`.

[31] T. Iwamoto, M. Tatezono, and H. Shinoda, "Non-contact Method for Producing Tactile Sensation Using Airborne Ultrasound," in *Haptics: Perception, Devices and Scenarios* (D. Hutchison, T. Kanade, J. Kittler, J. M. Kleinberg, F. Mattern, J. C. Mitchell, M. Naor, O. Nierstrasz, C. Pandu Rangan, B. Steffen, M. Sudan, D. Terzopoulos, D. Tygar, M. Y. Vardi, G. Weikum, and M. Ferre, eds.), vol. 5024, pp. 504–513, Berlin, Heidelberg: Springer Berlin Heidelberg, 2008. Series Title: Lecture Notes in Computer Science.

[32] T. Carter, S. A. Seah, B. Long, B. Drinkwater, and S. Subramanian, "UltraHaptics: multi-point mid-air haptic feedback for touch surfaces," in *Proceedings of the 26th annual ACM symposium on User interface software and technology*, (St. Andrews Scotland, United Kingdom), pp. 505–514, ACM, Oct. 2013.

[33] T. Howard, G. Gallagher, A. Lecuyer, C. Pacchierotti, and M. Marchal, "Investigating the Recognition of Local Shapes Using Mid-air Ultrasound Haptics," in *2019 IEEE World Haptics Conference (WHC)*, (Tokyo, Japan), pp. 503–508, IEEE, July 2019.

[34] Ultraleap. `https://www.ultraleap.com/`.

[35] T. Romanus, S. Frish, M. Maksymenko, W. Frier, L. Corenthy, and O. Georgiou, "Mid-Air haptic bio-holograms in mixed reality," pp. 348–352, 2019.

[36] M. Shinohara, Y. Shimizu, and A. Mochizuki, "Three-dimensional tactile display for the blind," *IEEE Transactions on Rehabilitation Engineering*, vol. 6, no. 3, pp. 249–256, 1998.

[37] H. Kajimoto, "Enlarged electro-tactile display with repeated structure," in *2011 IEEE World Haptics Conference*, pp. 575–579, 2011.

[38] C. Harrison and S. Hudson, "Providing dynamically changeable physical buttons on a visual display," pp. 299–308, 04 2009.

[39] M. Loechtefeld, "Towards Real Organic User Interfaces-Using Non-Newtonian Fluids for Self-Actuated Displays," p. 4.

[40] S. Karlin, "Tactus technology [resources start-ups]," *IEEE Spectrum*, vol. 50, no. 4, pp. 23–23, 2013.

[41] Y. Jansen, T. Karrer, and J. Borchers, "Mudpad: Tactile feedback and haptic texture overlay for touch surfaces," in *ACM International Conference on Interactive Tabletops and Surfaces*, ITS '10, (New York, NY, USA), p. 11–14, Association for Computing Machinery, 2010.

[42] S.-Y. Kim, J.-O. Kim, and K. Kim, "Traveling vibrotactile wave - a new vibrotactile rendering method for mobile devices," *IEEE Transactions on Consumer Electronics*, vol. 55, pp. 1032–1038, Aug. 2009.

[43] C. Hudin, J. Lozada, and V. Hayward, "Localized Tactile Feedback on a Transparent Surface through Time-Reversal Wave Focusing," *IEEE Transactions on Haptics*, vol. 8, pp. 188–198, Apr. 2015.

[44] S. Wöckel, U. Steinmann, and H. Arndt, "Modelling of time reversal for localized tactile feedback on displays," *Procedia Engineering*, vol. 120, pp. 302–305, 2015.

[45] L. Pantera and C. Hudin, "Sparse Actuator Array Combined with Inverse Filter for Multitouch Vibrotactile Stimulation," in *2019 IEEE World Haptics Conference (WHC)*, (Tokyo, Japan), pp. 19–24, IEEE, July 2019.

[46] S. Wockel, U. Steinmann, and H. Arndt, "Haptics by time reversal of elastic waves," in *2016 IEEE International Ultrasonics Symposium (IUS)*, (Tours, France), pp. 1–3, IEEE, Sept. 2016.

[47] A. Ben Dhiab, *Confinement of Vibrations for Localized Surface Haptics*. Theses, Sorbonne Université, Apr. 2022.

[48] E. Enferad, C. Giraud-Audine, F. Giraud, M. Amberg, and B. L. Semail, "Generating controlled localized stimulations on haptic displays by modal superimposition," *Journal of Sound and Vibration*, vol. 449, pp. 196–213, June 2019.

[49] P. Garcia, F. Giraud, B. Lemaire-Semail, M. Rupin, and M. Amberg, "2MoTac: Simulation of Button Click by Superposition of Two Ultrasonic Plate Waves," in *Haptics: Science, Technology, Applications* (I. Nisky, J. Hartcher-O'Brien, M. Wiertlewski, and J. Smeets, eds.), vol. 12272, pp. 343–352, Cham: Springer International Publishing, 2020. Series Title: Lecture Notes in Computer Science.

[50] E. Enferad, C. Giraud-Audine, F. Giraud, M. Amberg, and B. Lemaire-Semail, "Differentiated haptic stimulation by modal synthesis of vibration field," in *2018 IEEE Haptics Symposium (HAPTICS)*, (San Francisco, CA), pp. 216–221, IEEE, Mar. 2018.

[51] P. Garcia, F. Giraud, B. Lemaire-Semail, M. Rupin, and A. Kaci, "Control of an ultrasonic haptic interface for button simulation," *Sensors and Actuators A: Physical*, vol. 342, p. 113624, Aug. 2022.

[52] D. J. Meyer, M. A. Peshkin, and J. E. Colgate, "Fingertip friction modulation due to electrostatic attraction," in *2013 World Haptics Conference (WHC)*, (Daejeon), pp. 43–48, IEEE, Apr. 2013.

[53] O. Bau and I. Poupyrev, "Revel: Tactile feedback technology for augmented reality," *ACM Trans. Graph.*, vol. 31, jul 2012.

[54] X. Li, C. Choi, Y. Ma, P. Boonpuek, J. R. Felts, J. Mullenbach, C. Shultz, J. E. Colgate, and M. C. Hipwell, "Electrowetting: A Consideration in Electroadhesion," *IEEE Transactions on Haptics*, vol. 13, pp. 522–529, July 2020.

[55] F. Giraud, M. Amberg, and B. Lemaire-Semail, "Merging two tactile stimulation principles: electrovibration and squeeze film effect," in *2013 World Haptics Conference (WHC)*, (Daejeon), pp. 199–203, IEEE, Apr. 2013.

[56] T. Watanabe and S. Fukui, "A method for controlling tactile sensation of surface roughness using ultrasonic vibration," in *Proceedings of 1995 IEEE International Conference on Robotics and Automation*, vol. 1, (Nagoya, Japan), pp. 1134–1139, IEEE, 1995.

[57] M. Biet, "Discrimination of Virtual Square Gratings by Dynamic Touch on Friction Based Tactile Displays," p. 8, 2008.

[58] M. Biet, F. Giraud, and B. Lemaire-Semail, "The implementation of tactile feedback using squeeze film effect devices," vol. 43, pp. 123–135, 2008.

[59] T. Sednaoui, E. Vezzoli, B. Dzidek, B. Lemaire-Semail, C. Chappaz, and M. Adams, "Experimental evaluation of friction reduction in ultrasonic devices," in *2015 IEEE World Haptics Conference (WHC)*, (Evanston, IL), pp. 37–42, IEEE, June 2015.

[60] E. Vezzoli, Z. Vidrih, V. Giamundo, B. Lemaire-Semail, F. Giraud, T. Rodic, D. Peric, and M. Adams, "Friction Reduction through Ultrasonic Vibration Part 1: Modelling Intermittent Contact," *IEEE Transactions on Haptics*, vol. 10, pp. 196–207, Apr. 2017.

[61] T. Sednaoui, E. Vezzoli, B. Dzidek, B. Lemaire-Semail, C. Chappaz, and M. Adams, "Friction Reduction through Ultrasonic Vibration Part 2: Experimental Evaluation of Intermittent Contact and Squeeze Film Levitation," *IEEE Transactions on Haptics*, vol. 10, pp. 208–216, Apr. 2017.

[62] M. Wiertlewski, R. Fenton Friesen, and J. E. Colgate, "Partial squeeze film levitation modulates fingertip friction," *Proceedings of the National Academy of Sciences*, vol. 113, pp. 9210–9215, Aug. 2016.

[63] F. Giraud, M. Amberg, B. Lemaire-Semail, and G. casiez, "Design of a transparent tactile stimulator," in *2012 IEEE Haptics Symposium (HAPTICS)*, (Vancouver, BC, Canada), pp. 485–489, IEEE, Mar. 2012.

[64] E. Vezzoli, W. B. Messaoud, C. Nadal, M. Amberg, B. Lemaire-Semail, and A. Bueno, "Coupling of ultrasonic vibration and electrovibration for tactile stimulation," p. 22.

[65] F. Casset, G. le Rhun, B. Neff, B. Desloges, C. Dieppedale, and S. Fanget, "Low Voltage Haptic Slider Built Using Sol-Gel Thin-Film PZT Actuators Reported on Glass," in *2019 IEEE 32nd International Conference on Micro Electro Mechanical Systems (MEMS)*, (Seoul, Korea (South)), pp. 990–993, IEEE, Jan. 2019.

[66] S. Glinsek, M. A. Mahjoub, M. Rupin, T. Schenk, N. Godard, S. Girod, J. Chemin, R. Leturcq, N. Valle, S. Klein, C. Chappaz, and E. Defay, "Fully Transparent Friction-Modulation Haptic Device Based on Piezoelectric Thin Film," *Advanced Functional Materials*, vol. 30, p. 2003539, Sept. 2020.

[67] L. Song, S. Glinsek, S. Drnovsek, V. Kovacova, B. Malic, and E. Defay, "Piezoelectric thick film for power-efficient haptic actuator," *Applied Physics Letters*, vol. 121, p. 212901, Nov. 2022.

[68] F. Casset, J. Danel, P. Renaux, C. Chappaz, F. Bernard, T. Sednaoui, S. Basrour, B. Desloges, and S. Fanget, "4-inch transparent plates based on thin-film AlN actuators for haptic applications," *Mechatronics*, vol. 40, pp. 264–269, Dec. 2016.

[69] HAP2U, "Téléphone portable haptique HAP2U," 2020. https://region-aura.latribune.fr/innovation/innovation-technologique/2020-01-08/ces-2020-l-iserois-hap2u-devoile-son-premier-telephone-haptique-836380.html.

[70] C. Hudin, "Local friction modulation using non-radiating ultrasonic vibrations," in *2017 IEEE World Haptics Conference (WHC)*, (Munich, Germany), pp. 19–24, IEEE, June 2017.

[71] T. Daunizeau, D. Gueorguiev, S. Haliyo, and V. Hayward, "Phononic Crystals Applied to Localised Surface Haptics," *IEEE Transactions on Haptics*, vol. 14, pp. 668–674, July 2021.

[72] D. A. Torres, B. Lemaire-Semail, C. Giraud-Audine, F. Giraud, and M. Amberg, "Design and control of an ultrasonic surface haptic device for longitudinal and transverse mode comparison," *Sensors and Actuators A: Physical*, vol. 331, p. 113019, Nov. 2021.

[73] D. J. Meyer, M. Wiertlewski, M. A. Peshkin, and J. E. Colgate, "Dynamics of ultrasonic and electrostatic friction modulation for rendering texture on haptic surfaces," in *2014 IEEE Haptics Symposium (HAPTICS)*, (Houston, TX, USA), pp. 63–67, IEEE, Feb. 2014.

[74] Xiaowei Dai, J. E. Colgate, and M. A. Peshkin, "LateralPaD: A surface-haptic device that produces lateral forces on a bare finger," in *2012 IEEE Haptics Symposium (HAPTICS)*, (Vancouver, BC, Canada), pp. 7–14, IEEE, Mar. 2012.

[75] Z. Cai and M. Wiertlewski, "Ultraloop: Active lateral force feedback using resonant traveling waves," *IEEE Transactions on Haptics*, pp. 1–7, 2023.

[76] S. Ghenna, E. Vezzoli, C. Giraud-Audine, F. Giraud, M. Amberg, and B. Lemaire-Semail, "Enhancing Variable Friction Tactile Display Using an Ultrasonic Travelling Wave," *IEEE Transactions on Haptics*, vol. 10, pp. 296–301, Apr. 2017.

[77] E. C. Chubb, J. E. Colgate, and M. A. Peshkin, "ShiverPaD: A Glass Haptic Surface That Produces Shear Force on a Bare Finger," *IEEE Transactions on Haptics*, vol. 3, pp. 189–198, July 2010.

[78] J. Mullenbach, D. Johnson, J. E. Colgate, and M. A. Peshkin, "ActivePaD surface haptic device," in *2012 IEEE Haptics Symposium (HAPTICS)*, (Vancouver, BC, Canada), pp. 407–414, IEEE, Mar. 2012.

[79] S. J. Breitschaft, S. Clarke, *et al.*, "A theoretical framework of haptic processing in automotive user interfaces and its implications on design and engineering," *Frontiers in Psychology*, vol. 10, p. 1470, 2019.

[80] E. Huitema, "The Future of Displays Is Foldable," *Information Display*, vol. 28, pp. 6–10, Feb. 2012.

[81] S. Biswas and Y. Visell, "Emerging Material Technologies for Haptics," *Advanced Materials Technologies*, vol. 4, p. 1900042, Apr. 2019.

[82] A. Adilkhanov, M. Rubagotti, and Z. Kappassov, "Haptic Devices: Wearability-Based Taxonomy and Literature Review," *IEEE Access*, vol. 10, pp. 91923–91947, 2022.

[83] P. Strohmeier, J. Burstyn, J. P. Carrascal, V. Levesque, and R. Vertegaal, "ReFlex: A Flexible Smartphone with Active Haptic Feedback for Bend Input," in *Proceedings of the TEI '16: Tenth International Conference on Tangible, Embedded, and Embodied Interaction*, (Eindhoven Netherlands), pp. 185–192, ACM, Feb. 2016.

[84] W.-E. Ju, Y.-J. Moon, C.-H. Park, and S. T. Choi, "A flexible tactile-feedback touch screen using transparent ferroelectric polymer film vibrators," *Smart Materials and Structures*, vol. 23, p. 074004, July 2014.

[85] S. Yun, S. Park, B. Park, S. Ryu, S. M. Jeong, and K.-U. Kyung, "A Soft and Transparent Visuo-Haptic Interface Pursuing Wearable Devices," *IEEE Transactions on Industrial Electronics*, vol. 67, pp. 717–724, Jan. 2020.

[86] W.-H. Park, E.-J. Shin, S. Yun, and S.-Y. Kim, "An Enhanced Soft Vibrotactile Actuator Based on ePVC Gel with Silicon Dioxide Nanoparticles," *IEEE Transactions on Haptics*, vol. 11, pp. 22–29, Jan. 2018.

[87] X. Yu, Z. Xie, Y. Yu, J. Lee, A. Vazquez-Guardado, H. Luan, J. Ruban, X. Ning, A. Akhtar, D. Li, B. Ji, Y. Liu, R. Sun, J. Cao, Q. Huo, Y. Zhong, C. Lee, S. Kim, P. Gutruf, C. Zhang, Y. Xue, Q. Guo, A. Chempakasseril, P. Tian, W. Lu, J. Jeong, Y. Yu, J. Cornman, C. Tan, B. Kim, K. Lee, X. Feng, Y. Huang, and J. A. Rogers, "Skin-integrated wireless haptic interfaces for virtual and augmented reality," *Nature*, vol. 575, pp. 473–479, Nov. 2019.

[88] D. Li, J. He, Z. Song, K. Yao, M. Wu, H. Fu, Y. Liu, Z. Gao, J. Zhou, L. Wei, Z. Zhang, Y. Dai, Z. Xie, and X. Yu, "Miniaturization of mechanical actuators in skin-integrated electronics for haptic interfaces," *Microsystems & Nanoengineering*, vol. 7, p. 85, Dec. 2021.

[89] I. Trase, Z. Xu, Z. Chen, H. Tan, and J. X. Zhang, "Thin-film bidirectional transducers for haptic wearables," *Sensors and Actuators A: Physical*, vol. 303, p. 111655, Mar. 2020.

[90] I. Trase, H. Z. Tan, Z. Chen, and J. X. Zhang, "Flexible electrostatic transducer array with displacement control for haptic sensing and actuation," *Sensors and Actuators A: Physical*, vol. 317, p. 112452, Jan. 2021.

[91] J. Ma, X. Cheng, P. Wang, Z. Jiao, Y. Yu, M. Yu, B. Luo, and W. Yang, "A Haptic Feedback Actuator Suitable for the Soft Wearable Device," *Applied Sciences*, vol. 10, p. 8827, Dec. 2020.

[92] G. Grasso, S. Rosset, and H. Shea, "Fully 3D-Printed, Stretchable, and Conformable Haptic Intaktherfaces," *Advanced Functional Materials*, vol. 33, p. 2213821, May 2023.

[93] A. Akther, J. O. Castro, S. A. Mousavi Shaegh, A. R. Rezk, and L. Y. Yeo, "Miniaturised acoustofluidic tactile haptic actuator," *Soft Matter*, vol. 15, no. 20, pp. 4146–4152, 2019.

[94] N. Besse, S. Rosset, J. J. Zarate, and H. Shea, "Flexible Active Skin: Large Reconfigurable Arrays of Individually Addressed Shape Memory Polymer Actuators," *Advanced Materials Technologies*, vol. 2, no. 1700102, 2017.

[95] J. Lee, H. Sul, W. Lee, K. R. Pyun, I. Ha, D. Kim, H. Park, H. Eom, Y. Yoon, J. Jung, D. Lee, and S. H. Ko, "Stretchable Skin-Like Cooling/Heating Device for Reconstruction of Artificial Thermal Sensation in Virtual Reality," *Advanced Functional Materials*, vol. 30, p. 1909171, July 2020.

[96] H. Kim, S. Yun, K. Kim, W. Kim, J. Ryu, H. G. Nam, S. M. Han, S. Jeon, and S. Hong, "Breaking the elastic limit of piezoelectric ceramics using nanostructures: A case study using ZnO," *Nano Energy*, vol. 78, p. 105259, Dec. 2020.

[97] E. S. Ege and A. Balikci, "Transparent localized haptics: Utilization of pvdf actuators on touch displays," *Actuators*, vol. 12, no. 7, 2023.

[98] A. Bartasyte, G. Clementi, Q. Micard, I. Labbaveettil, A. S. L. Moreira, S. Boujnah, M. Ouhabaz, A. Verma, A. Ichangi, G. Malandrino, S. Mathur, B. Dulmet, and S. Margueron, "Material strategies to enhance the performance of piezoelectric energy harvesters based on lead-free materials," *Journal of Micromechanics and Microengineering*, vol. 33, p. 053001, May 2023.

[99] H. Lamb, "On the Vibrations of an Elastic Sphere," *Proceedings of the London Mathematical Society*, vol. s1-13, pp. 189–212, Nov. 1881.

[100] H. Lamb, "On waves in an elastic plate," *Royal Society London*, vol. 93, no. 648, pp. 114 – 128, 1917.

[101] J. D. Achenbach, *Wave propagation in elastic solids*. No. v. 16 in North-Holland series in applied mathematics and mechanics, Amsterdam New York: North-Holland Pub. Co. American Elsevier Pub. Co, 1973.

[102] M. D. Waller, "Vibrations of Free Rectangular Plates," *Proceedings of the Physical Society. Section B*, vol. 62, pp. 277–285, May 1949.

[103] T. D. Rossing and N. H. Fletcher, *Principles of Vibration and Sound*. New York, NY: Springer New York, 1995.

[104] A. W. Leissa, *Vibration of Plates*. 1969.

[105] A. G. Piersol, T. L. Paez, and C. M. Harris, eds., *Harris' shock and vibration handbook*. New York: McGraw-Hill, 6th ed ed., 2010.

[106] C. Jeerapan, W. Sriratana, P. Julsereewong, and S. Kummool, "Analysis of Appropriate Parameters for Piezoelectric Ceramic Utilization by Using BVD Model," p. 4.

[107] W. B. Messaoud, M.-A. Bueno, *et al.*, "Relation between human perceived friction and finger friction characteristics," *Tribology International*, vol. 98, pp. 261–269, June 2016.

[108] Y. Xiao, J. Wen, and X. Wen, "Flexural wave band gaps in locally resonant thin plates with periodically attached spring–mass resonators," *Journal of Physics D: Applied Physics*, vol. 45, p. 195401, apr 2012.

[109] J. Jung, S. Goo, and S. Wang, "Investigation of flexural wave band gaps in a locally resonant metamaterial with plate-like resonators," *Wave Motion*, vol. 93, p. 102492, 2020.

[110] E. Miranda Jr., E. Nobrega, S. Rodrigues, C. Aranas Jr., and J. Dos Santos, "Wave attenuation in elastic metamaterial thick plates: Analytical, numerical and experimental investigations," *International Journal of Solids and Structures*, vol. 204-205, pp. 138–152, 2020.

[111] J. S. Alfonso Sepúlveda and P. M. Vereecken, "Bending impact on the performance of a flexible li4ti5o12-based all-solid-state thin-film battery," *Science and Technology of Advanced Materials*, vol. 19, no. 1, pp. 454–464, 2018. PMID: 29868149.

[112] H. U. Li and T. N. Jackson, "Flexibility testing strategies and apparatus for flexible electronics," *IEEE Transactions on Electron Devices*, vol. 63, no. 5, pp. 1934–1939, 2016.

[113] J. Sheng, H.-J. Jeong, K.-L. Han, T. Hong, and J.-S. Park, "Review of recent advances in flexible oxide semiconductor thin-film transistors," *Journal of Information Display*, vol. 18, no. 4, pp. 159–172, 2017.

[114] R. Saleh, M. Barth, W. Eberhardt, and A. Zimmermann, "Bending setups for reliability investigation of flexible electronics," *Micromachines*, vol. 12, no. 1, 2021.

[115] T. B. G. Olde Dubbelink, F. G. C. M. De Kleermaeker, R. Beekman, J. Wijntjes, R. H. M. A. Bartels, J. Meulstee, and W. I. M. Verhagen, "Wrist circumference-dependent upper limit of normal for the cross-sectional area is superior over a fixed cut-off value in confirming the clinical diagnosis of carpal tunnel syndrome," *Frontiers in Neurology*, vol. 12, 2021.

[116] S. Trolier-McKinstry and P. Muralt, "Thin Film Piezoelectrics for MEMS," *Journal of Electroceramics*, vol. 12, pp. 7–17, Jan. 2004.

[117] C. Freitag, M. Berners-Lee, K. Widdicks, B. Knowles, G. Blair, and A. Friday, *The climate impact of ICT: A review of estimates, trends and regulations*. Feb. 2021.

[118] S. Dauvé and L. Di Cioccio, "Comment réduire l'impact environnemental de la microélectronique dans un domaine du semi-conducteur en pleine évolution ?," *Annales des Mines - Responsabilité et environnement*, vol. 110, no. 2, pp. 95–101, 2023. Publisher: Institut Mines-Télécom.

[119] A. Villard, A. Lelah, and D. Brissaud, "Drawing a chip environmental profile: environmental indicators for the semiconductor industry," *Journal of Cleaner Production*, vol. 86, pp. 98–109, Jan. 2015.

[120] L. Vauche, G. Guillemaud, J.-C. Barbosa, and L. Di Cioccio, "Cradle-to-gate life cycle assessment (lca) of gan power semiconductor device," *Sustainability*, vol. 16, p. 901, 01 2024.

[121] Europa, "European Platform on LCA | EPLCA." `https://eplca.jrc.ec.europa.eu/LCDN/developerEF.xhtml`.

[122] A. Pikovsky, M. Rosenblum, and j. Kurths, *Synchronization. A Universal Concept in Nonlinear Sciences.* Cambridge University Press, 2001.

[123] R. Adler, "A study of locking phenomena in oscillators," *Proceedings of the IEEE*, vol. 61, no. 10, pp. 1380–1385, 1973.

[124] F. Montoya, M. Rivera, J. Escalona, and P. Parmananda, "Construction of arnold tongue structures for coupled periodic oscillators," *Physics Letters A*, vol. 377, no. 43, pp. 3124–3127, 2013.

[125] S. H. Strogatz, "From Kuramoto to Crawford: exploring the onset of synchronization in populations of coupled oscillators," *Physica D: Nonlinear Phenomena*, vol. 143, pp. 1–20, Sept. 2000.

[126] J. A. Acebrón, L. L. Bonilla, C. J. Pérez Vicente, F. Ritort, and R. Spigler, "The kuramoto model: A simple paradigm for synchronization phenomena," *Rev. Mod. Phys.*, vol. 77, pp. 137–185, Apr 2005.

[127] F. A. Rodrigues, T. K. D. Peron, P. Ji, and J. Kurths, "The kuramoto model in complex networks," *Physics Reports*, vol. 610, pp. 1–98, 2016. The Kuramoto model in complex networks.

[128] B. C. Daniels, "Synchronization of globally coupled nonlinear oscillators: the rich behavior of the kuramoto model," 2005.

[129] K. Uchino, "Chapter 17 - high-power piezoelectrics and loss mechanisms," in *Advanced Piezoelectric Materials (Second Edition)* (K. Uchino, ed.), Woodhead Publishing in Materials, pp. 647–754, Woodhead Publishing, second edition ed., 2017.

[130] R. F. Friesen, M. Wiertlewski, and J. E. Colgate, "The role of damping in ultrasonic friction reduction," in *2016 IEEE Haptics Symposium (HAPTICS)*, pp. 167–172, 2016.

[131] N. Huloux, C. Bernard, and M. Wiertlewski, "Estimating friction modulation from the ultrasonic mechanical impedance," *IEEE Transactions on Haptics*, vol. 14, no. 2, pp. 409–420, 2021.

List of Publications

[1] Fabrice Casset and Romain Le Magueresse. "Haptic interface with flexible hinges." U.S. Patent Application No. 18/049,342.

[2] R. Le Magueresse, F. Casset F. Giraud, B. Desloges, N. David, A. Kaci, A. Berdagué, and M. Colin, "Piezoelectric flexible haptic interface development," *2022 23rd International Conference on Thermal, Mechanical and Multi-Physics Simulation and Experiments in Microelectronics and Microsystems (EuroSimE)*, St Julian, Malta, 2022, pp. 1-5.

[3] R. Le Magueresse, F. Giraud, F. Casset, A. Kaci, B. Desloges and M. Colin, "Preliminary Design of a Flexible Haptic Surface". *In: Seifi, H., et al. Haptics: Science, Technology, Applications. EuroHaptics 2022. Lecture Notes in Computer Science*, vol 13235.

[4] R. Le Magueresse, F. Casset, F. Giraud, M. Kazar Mendes, S. Brulais, L. Peris Y Saborit, A. Kaci and M. Colin, "Development, realization and validation of a piezoelectric flexible haptic interface", *International Conference on Solid State Sensors and Actuators (TRANSDUCERS)*, 2023.

[5] R. Le Magueresse, F. Casset, F. Giraud, M. Kazar Mendes, A. Kaci and M. Colin, "Reconfigurable flexible haptic interface using friction modulation", *Work-In-Progress + Demonstration WorldHaptics23*, 2023.

[6] R. Le Magueresse, F. Casset, F. Giraud, M. Kazar Mendes, D. Mermin, R. Franiatte, A. Kaci and M. Colin, "Reconfigurable flexible haptic interface using localized friction modulation", *Transactions on Haptics (ToH)*, Under review.

Titre: Développement d'une interface haptique flexible à modulation de frottement localisé

Mots clés: Haptique, Haptique flexible, Modulation de frottement

Résumé: Les technologies haptiques améliorent nos interactions avec les interfaces homme-machine en intégrant le sens du toucher. Elles permettent diverses expériences, notamment sur les écrans tactiles rigides, allant des simples vibrations à la reproduction de textures par modulation du frottement entre le doigt et l'écran vibrant dans un mode ultrasonore. Parallèlement, l'émergence de l'électronique flexible, utilisée notamment dans la fabrication des téléphones pliables et des dispositifs portables, a ouvert la voie au développement de technologies haptiques flexibles. Cependant aucune de ces nouvelles solutions flexibles n'est efficace pour reproduire des effets de texture.

Cette thèse relève donc le défi de créer une interface flexible capable de reproduire un retour haptique localisé ou continu grâce à la modulation du frottement. Pour ce faire, un concept d'interface hybride est développé, intégrant des résonateurs haptiques rigides d'environ 1 cm^2 à un film polymère d'une épaisseur maximale de 100 µm. Les dimensions des résonateurs ultrasonores et de l'interface, constituée de 3 x 3 résonateurs, sont optimisées à l'aide de modèles analytiques et de simulations numériques. La fabrication est réalisée selon un processus en salle blanche évalué par une analyse du cycle de vie. Des mesures électromécaniques valident ensuite le fonctionnement de la technologie avec notamment des déplacements en surface supérieurs à 1 µm pour une faible tension d'actionnement de 20 Vpp. Des essais tribologiques vérifient la réduction du frottement lors d'un toucher actif des utilisateurs. Enfin, des études psychophysiques confirment la localisation et la continuité des ressentis haptiques, affirmant ainsi le caractère multitouch et multi-utilisateurs de cette interface. En conséquence, les applications potentielles de cette nouvelle technologie sont vastes, promettant des améliorations dans les interactions homme-machine en reproduisant des sensations texturées sur des surfaces flexibles et conformables.

Title: Development of a flexible haptic interface using localized friction modulation

Keywords: Haptic, Flexible haptic, Friction modulation

Abstract: Haptic technologies enhance our interactions with human-machine interfaces by integrating the sense of touch. They enable a variety of experiments, particularly on rigid touch screens, ranging from simple vibrations to the reproduction of textures by modulation of the friction between the finger and the vibrating screen in an ultrasonic mode. At the same time, the emergence of flexible electronics, used notably in the manufacture of foldable phones and wearable devices, has led the way to the development of flexible haptic technologies. However, none of these new flexible solutions is effective in reproducing texture effects.

This thesis therefore takes up the challenge of creating a flexible interface capable of reproducing localized or continuous haptic feedback through friction modulation. To achieve this, a hybrid interface concept is developed, integrating rigid haptic resonators of around 1 cm^2 with a polymer film of up to 100 µm thickness. The dimensions of the ultrasonic resonators and the interface, consisting of 3 x 3 resonators, are optimized using analytical models and numerical simulations. Manufacturing is carried out in a cleanroom process, assessed by a life-cycle analysis. Electromechanical measurements validate the technology's performance, with surface displacements of over 1 µm at a low actuating voltage of 20 Vpp. Tribological tests verify the reduction in friction during active user touch. Finally, psychophysical studies confirm the localization and continuity of haptic sensations, thus affirming the multitouch and multi-user nature of this interface. As a result, the potential applications of this new technology are vast, promising improvements in human-machine interactions by reproducing textured sensations on flexible and conformable surfaces.